Plasmons in metal nanostructures

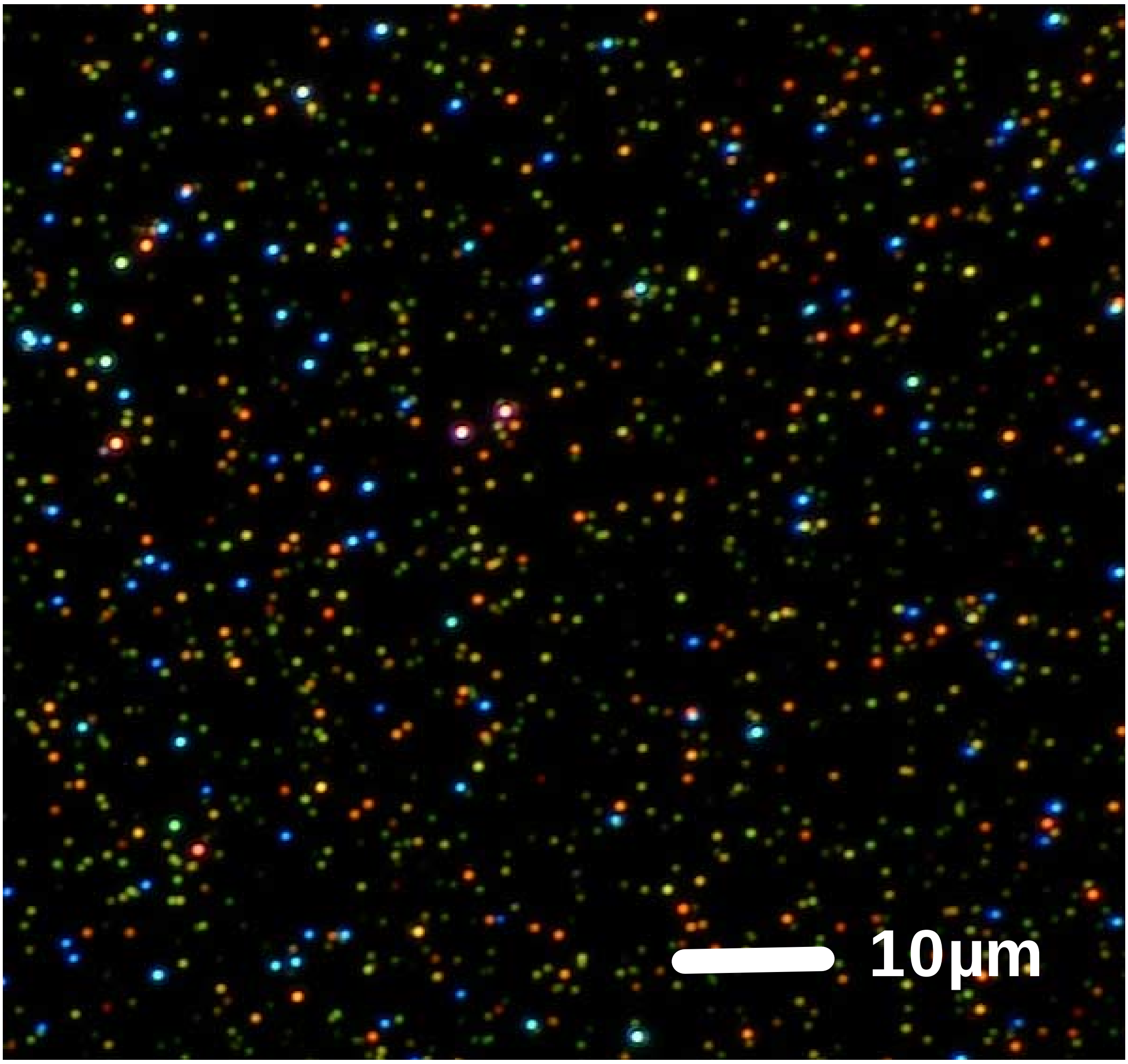

Dissertation der Fakultät für Physik der
Ludwig-Maximilians-Universität München,
vorgelegt von Carsten Sönnichsen aus Hamburg.

München, 20 June 2001

A dissertation submitted to the physics department of the
Ludwig-Maximilians-University of Munich by Carsten Sönnichsen.

Preface

This dissertation is the result of work carried out in the Photonics and Optoelectronics group at the University of Munich. Part of the work was conducted in collaboration with other groups at the Karl-Franzens University of Graz, the University of Ulm and the University of Melbourne.

Except where specific reference is made to the work of others, this work is original and has not been already submitted either wholly or in part to satisfy any degree requirement at this or any other university.

Carsten Sönnichsen

Tag der mündlichen Prüfung: 24. 7. 2001
1. Gutachter: Prof. Dr. J. Feldmann
2. Gutachter: Prof. Dr. H. Gaub
Weitere Prüfungskommissionsmitglieder:
Prof. Dr. J. von Delft (Vorsitzender), Prof. Dr. H. Weinfurter

The picture on the front page shows a true color image of a sample containing gold and silver nanospheres as well as gold nanorods photographed with a dark field microscope. Each dot corresponds to light scattered by an individual nanoparticle at the plasmon resonance. The resonance wavelength varies from blue (silver nanospheres) via green and yellow (gold nanospheres) to orange and red (nanorods).

(This document is typeset by LaTeX.)

Scientific publications of results presented in this work

Fabrication and properties of nanorods
O. Wilson, C. Sönnichsen, ..., P. Mulvaney, Nanoletters, in preparation

Suppression of interband damping of plasmons in gold nanorods
C. Sönnichsen, T. Franzl, T. Wilk, G. von Plessen, J. Feldmann, O. Wilson, P. Mulvaney, Phys. Rev. Lett., submitted

Electrically controlled light scattering by particle plasmons
C. Sönnichsen, A. Jakab, G. von Plessen, J. Feldmann, in preparation

Spectroscopy of single metallic nanoparticles using total internal reflection microscopy
C. Sönnichsen, S. Geier, N.E. Hecker, G. von Plessen, J. Feldmann, H. Ditlbacher, B. Lamprecht, J.R. Krenn, F.R. Aussenegg, V.Z.-H. Chan, J.P. Spatz, and M. Möller, Appl. Phys. Lett. 77, 2949 (2000)

Launching surface plasmons into nano-holes in metal films
C. Sönnichsen, A.C. Duch, G. Steininger, M. Koch, G. von Plessen, and J. Feldmann
Appl. Phys. Lett. 76, 140 (2000)

Contributions to conferences, workshops, and seminars

Invited talks:

Spectroscopy of single metallic nanoparticles
European Science Foundation Exploratory Workshop on Surface Plasmon Photonics
27-30 April 2000, Obernai, France

Nanooptics with Plasmons
- Seminar, University of Hamburg (July 1999)
- SFB 513 ('Nanostructures at Interfaces and Surfaces') workshop (September 1999)
- Center for NanoScience (CeNS) workshop in Wildbad Kreuth (2000)
- Seminar, University of Ulm (February 2000)

Using metal particles as nanosensors
Seminar 'Fallstudien aus der Optoelektronik', Munich, 13 May 2000

Contributed talks:

Spectroscopy of single metallic nanoparticles
C. Sönnichsen, A. Jakab, S. Geier, T. Wilk, G. von Plessen, J. Feldmann
Spring Meeting of the American Physical Society (APS), Seattle, April 2001

Metal nanoparticles as optical nanosensors for concentrations of organic molecules
S. Malkmus, T.Franzl, T. Wilk, C. Sönnichsen, G. von Plessen, J. Feldmann
Spring Meeting of the German Physical Society (DPG), Berlin, May 2001

Coupling of plasmon modes in metal nanoparticle pairs
T. Franzl, C. Sönnichsen, G. von Plessen, J. Feldmann
Spring Meeting of the German Physical Society (DPG), Berlin, May 2001

Dephasing times of the particle plasmon resonances in spherical gold and silver nanoparticles
C. Sönnichsen, T. Wilk, S. Geier, E. Dulkeith, G. von Plessen, J. Feldmann
Spring Meeting of the German Physical Society (DPG), Berlin, May 2001

Nanogolf with surface plasmons
C. Sönnichsen, A. Duch, G. Steininger, M. Koch, G. von Plessen, J. Feldmann; and
Spectroscopy of single metallic nanoparticles using total internal reflection microscopy (post deadline poster)
C. Sönnichsen, S. Geier, N. E. Hecker, G. von Plessen, J. Feldmann
6th International Conference on Near Field Optics and related techniques (NFO-6)
August 27-31, 2000 University of Twente, Enschede, The Netherlands

NFO experiments on nanoholes in metal films
C. Sönnichsen, A. Duch, G. Steininger, M. Koch, G. von Plessen, J. Feldmann
Nanoscale Optics topical meeting of the European Optical Society,
16-19 April 2000, Engelberg, Switzerland

Nanogolf mit Oberflächenplasmonen
C. Sönnichsen, A. Duch, G. Steininger, M. Koch, G. von Plessen, J. Feldmann
Spring Meeting of the German Physical Society (DPG), Regensburg, May 2000

Lichttransmission durch einzelne Nanolöcher in dünnen Metallfilmen
G. Steininger, A. Duch, C. Sönnichsen, G. von Plessen, M. Koch, U. Lemmer, and J. Feldmann
Spring Meeting of the German Physical Society (DPG), Münster, May 1999

Near-field study of surface plasmons in individual noble-metal nanoparticles
C. Sönnichsen, T. Klar, J. März, M. Perner, S. Grosse, W. Spirkl, G. von Plessen, J. Feldmann
5th International Conference on Near Field Optics and related techniques (NFO-5)
6-10 December 1998, Shirahama, Japan

ZUSAMMENFASSUNG

Die Anregung von Plasmonen, d.h. kollektiven Schwingungen der Leitungsbandelektronen, hat einen starken Einfluß auf die optischen Eigenschaften metallischer Nanostrukturen und ist von großem Interesse für zukünftige photonische Bauelemente. In dieser Arbeit werden Plasmonen in metallischen Nanostrukturen mit optischen Mikroskopiermethoden im Nah- und Fernfeld untersucht. Im Mittelpunkt steht die lineare Wechselwirkung zwischen Licht und einzelnen Nanostrukturen.

Insbesondere wird die Lichttransmission durch einzelne Nanometer große Löcher in undurchsichtigen Metallfilmen mit Hilfe eines optischen Rasternahfeldmikroskops (SNOM, von engl. Scanning Near-field Optical Microscope) untersucht. Die Ergebnisse zeigen eindeutig die in letzter Zeit viel debattierte Unterstützung der Lichttransmission durch solche Nanolöcher mit Hilfe der Anregung und lateralen Ausbreitung von Oberflächenplasmonen. Die Ausbreitungsrichtung ist durch die Lichtpolarisation gegeben, so daß die kontrollierte Adressierung von einzelnen Löchern möglich ist — diesen Prozess kann man bildlich als "Nanogolf" bezeichnen. Die polarisationsabhängige Adressierung von spezifischen Nanolöchern könnte für das Demulitiplexen in zukünftigen optischen Systemen anwendbar sein.

Außerdem werden die Dephasierungszeiten und lokale Feldverstärkungsfaktoren für Plasmonen in Edelmetall-Nanopartikeln bestimmt, indem die Lichtstreuung an einzelnen Nanopartikeln spektral mit Hilfe eines dunkelfeldmikroskopischen Aufbaus untersucht wird. Es wird gezeigt, daß Strahlungsdämpfung die Dephasierungszeit T_2 in Gold-Nanokugeln auf 2-5 fs begrenzt. Die Unterdrückung von Interbanddämpfung in Gold-Nanostäbchen führt hingegen zu überraschend langen Dephasierungszeiten und großen lokalen Feldverstärkungsfaktoren. Der Rekordwert von $T_2 = 18\,\mathtt{fs}$ nähert sich der theoretischen Grenze, die durch die Freie-Elektronen-Relaxationszeit gegeben ist. Das Ergebnis dieser ersten systematischen und aussagekräftigen experimentellen Untersuchung an einzelnen Partikeln beantwortet die seit langem debattierte Frage nach der Stärke der Plasmonendämpfung in Gold-Nanopartikeln. Die gute Übereinstimmung mit Berechnungen unter Verwendung der dielektrischen Funktion von Volumengold zeigt, daß rein kollektive Dephasierungsmechanismen und Oberflächeneffekte nur einen vernachlässigbaren Beitrag zur Gesamtdämpfung in den untersuchten Nanopartikeln liefern. Die relativen Anteile von strahlender, Inter- und Intraband-Dämpfung in Gold-Nanopartikeln werden bestimmt. Zudem kann die "wahre" Partikelplasmonendämpfungszeit im Sinne einer reinen Plasmonenschwingung ohne Ankopplung an Photonen oder Interband- Anregungen angegeben werden.

Die spektroskopische Untersuchung von Plasmonen in einzelnen Nanopartikeln kann auch verwended werden, um den Brechungsindex des Mediums um diese Partikel zu bestimmen. Hier wird zum ersten Mal gezeigt, wie diese Methode angewendet werden kann, um optische Nanosensoren basierend auf Partikelplasmonen zu bauen. Anwendungen für die Bestimmung von lokalen Konzentrationen, Bindungsereignissen und Redox-Reaktionen werden gezeigt. Ein solcher Nanosensor wird nur von einem Volumen in der winzigen Größenordnung von Attolitern beeinlußt. Erste Experimente zur Steigerung der Sensorempfindlichkeit zeigen die Entwicklungsmöglichkeiten dieser Technik.

Aktives Ändern der Partikelumgebung durch die elektrische Ausrichtung von Flüssigkristallmolekülen ermöglicht es, die Resonanzfrequenz über weite spektrale Bereiche zu verschieben. Die in dieser Arbeit gezeigten Experimente demonstrieren, daß dieser neue Effekt eingesetzt werden kann, um Lichtstreuung mit hohem Kontrast und spektraler Selektivität elektrisch zu steuern.

ABSTRACT

Plasmon excitations, i.e. collective oscillations of the conduction electrons, strongly influence the optical properties of metal nanostructures and are of great interest for future photonic devices. Here, plasmons in metal nanostructures are investigated by near- and far-field optical microscopic techniques. Emphasis is placed on the study of the linear interaction of light with individual nanostructures.

Specifically, the light transmission through individual nanometer-sized holes in opaque metal films is investigated using a scanning near-field optical microscope (SNOM). It is shown unambiguously that excitation and lateral propagation of surface plasmons support the light transmission through these nanoholes. This process has been under discussion recently. The propagation direction is given by the light polarization, thus allowing controlled addressing of individual holes — a process that may figuratively be described as "nanogolf". This polarization controlled addressing of specific holes may be applicable for de-multiplexing purposes in future optical systems.

Furthermore, the dephasing times and local field enhancement factors of plasmons in noble metal nanoparticles are determined by spectrally investigating the light-scattering from individual nanoparticles in a dark-field microscope setup. It is found that radiation damping limits the plasmon dephasing time, T_2, in the gold nanospheres studied here to 2-5 fs, whereas suppression of interband damping in gold nanorods leads to surprisingly long particle plasmon dephasing times and large local field enhancement factors. The record value of T_2=18 fs approaches the theoretical limit given by the free-electron relaxation time. The results of this first systematic and conclusive experimental study on individual particles answer the long debated question of the amount of plasmon damping in gold nanoparticles. Good agreement with calculations using the bulk dielectric function of gold shows that purely collective dephasing and surface effects contribute negligibly to the overall damping in the particles under investigation. The experimental results allow to deduce the relative contributions of radiation, inter- and intraband damping in gold nanoparticles. Also, the "true" particle plasmon dephasing time is determined in the sense of a pure plasmon oscillation without coupling to photons or interband excitations.

The spectroscopic investigation of plasmons in single nanoparticles can also be used to determine the refractive index of the medium surrounding the particles. It is demonstrated for the first time how this can be used to build optical nanosensors based on particle plasmons. Applications for local concentrations, binding events and redox reactions are shown. The sensing volume of such a nanosensor is on the order of attoliters. First experiments towards increasing the sensitivity show the prospect of this technique.

Actively changing the environment around metal particles by electrically aligning liquid crystal molecules allows the shift of the resonance frequency over a wide spectral range. The experiments presented here show that this novel effect can be used for electrically controlled light scattering with high contrast and spectral selectivity.

CONTENTS

1. Introduction 19

2. Theoretical background 21

2.1 Classical electrodynamics in matter 21

2.1.1 Limits 21

2.1.2 Maxwell equations in matter 22

2.2 Solid state theory for optical constants of metals 23

2.2.1 Drude-Sommerfeld model 23

2.2.2 Empirical bulk values for noble metals 24

2.2.3 Adjustment for very small particles 26

2.3 Quasi-particle lifetime and linewidth of resonances 26

2.3.1 Fourier-transformation 27

2.3.2 Driven harmonic oscillator 27

2.3.3 Deducing lifetimes 29

3. Plasmon modes on planar metal-dielectric interfaces – *surface plasmons* 31

3.1 Properties and applications 31

3.2 Electrodynamical theory 32

3.3 Surface plasmon excitation by light 33

3.4 Interaction with nanostructures 34

3.5 Surface plasmon assisted light transmission through nanoholes 35

4. Plasmon modes in metal nanoparticles — *particle plasmons* 37

4.1 Simple semi-classical model 38

4.2 Properties and applications 38

4.3 Light scattering and absorption by metal nanoparticles 39

4.4 Damping mechanisms of particle plasmons 41

4.5 Electrodynamic theories for particle plasmons . . . 42
  4.5.1 Quasi-static approximation — Rayleigh Theory . . . 42
  4.5.2 Scattering by elliptical particles . . . 43
  4.5.3 Mie theory . . . 45
  4.5.4 Some results of electrodynamic calculations . . . 46
  4.5.5 Limits of the electrodynamic theory . . . 49
4.6 Open questions . . . 49

5. Experimental methods . . . 51
5.1 Near-field microscopy . . . 51
5.2 Microscopic scattering spectroscopy in the far-field . . . 54
  5.2.1 Total internal reflection microscopy . . . 54
  5.2.2 Dark-field microscopy in reflection . . . 56
  5.2.3 Dark-field microscopy in transmission . . . 57
  5.2.4 Recording of scattering spectra . . . 58
5.3 Determination of dephasing times from single particle scattering spectra . . . 60

6. Samples . . . 63
6.1 Electron-beam lithography: nanodisks . . . 63
6.2 Chemical synthesis: nanospheres and -rods . . . 66
  6.2.1 Sample preparation . . . 69
6.3 Nanoholes in gold, silver and aluminum films . . . 70

7. Light transmission through nanoholes . . . 73
7.1 Experimental configuration . . . 73
7.2 Experimental results . . . 74
  7.2.1 Polarization effect . . . 75
  7.2.2 Wavelength effect . . . 75
  7.2.3 Interferences . . . 76
7.3 Conclusion . . . 76

8. Particle plasmon damping . . . 79
8.1 Gold nanodisks . . . 80
8.2 Gold nanospheres . . . 84

- 8.3 Silver nanospheres 89
- 8.4 Gold nanorods 92
- 8.5 Particle pairs 98
- 8.6 Discussion 99
  - 8.6.1 Summary of dephasing times 99
  - 8.6.2 Particle plasmon damping mechanisms in gold (qualitative) 102
  - 8.6.3 Particle plasmon damping mechanism in gold (quantitative) 105
  - 8.6.4 The ‘true’ plasmon dephasing time 106
- 8.7 Summary 108

9. Nanosensor applications 109
- 9.1 Measurements in liquids 110
- 9.2 Local concentration sensor 110
- 9.3 Increasing sensitivity 111
  - 9.3.1 Measurement accuracy 112
  - 9.3.2 Linewidth and magnitude of the resonance-shift 113
  - 9.3.3 Conclusion 114
- 9.4 Binding indicator 114
- 9.5 Particle charge sensor – Redox potential sensor 115
- 9.6 Discussion 115
- 9.7 Summary 116

10. Electrically controlled light scattering 117
- 10.1 Principle of the experiment 117
- 10.2 Electrically induced plasmon resonance shift 119
- 10.3 Polarization effect 119
- 10.4 Model and discussion 121
- 10.5 Conclusion 122

11. Summary 123

Bibliography 125

Curriculum Vitae 131

Acknowledgements 133

LIST OF FIGURES

2.1 Dielectric function of gold 25

2.2 Dielectric function of silver 25

2.3 Damped harmonic oscillator 28

3.1 Dispersion of surface plasmons 33

3.2 Excitation configuration of surface plasmons 34

3.3 Light transmission through arrays of nanoholes 35

4.1 Lycurgus cup 37

4.2 Simple model for particle plasmons 38

4.3 Backscattering and extinction of gold particles in suspension 40

4.4 Comparison of luminescence and light scattering 40

4.5 Particle plasmon decay mechanism 41

4.6 Quasi-static model for particle plasmons 42

4.7 Prolate and oblate spheroids 43

4.8 Geometrical factor of a prolate spheroid 44

4.9 MATHEMATICA$^{\mathtt{tm}}$ script to calculate Mie coefficients 46

4.10 Mie scattering cross-sections 47

4.11 Influence of particle size and shape on plasmons resonances 47

4.12 Influence of the embedding medium on particle plasmons 48

5.1 Scanning near-field optical microscope (SNOM) setup 52

5.2 Experimental setup used to couple two laser into the SNOM fiber 53

5.3 Colorful light scattering in SNOM experiments 53

5.4 Comparison of bright- and dark-field microscopy 55

5.5 Total internal reflection microscope (TIRM) setup. 55

5.6 Dark-field microscopy setup in reflection 56

5.7 Dark-field microscopy setup in transmission 57
5.8 Photograph of the total internal reflection setup 58
5.9 Measuring process for single particle scattering spectra 59
5.10 SNOM scattering spectrosopy 60
5.11 Comparison of single particle spectra obtained by different methods 61

6.1 Electron beam lithography processes 63
6.2 Exposure dose dependence of disk diameter 64
6.3 Structure of lithographically produced samples 65
6.4 Suspensions of gold nanospheres in water 66
6.5 Ensemble extinction spectra of gold and silver nanospheres 67
6.6 Transmission electron microscopy (TEM) images of gold nanorods 68
6.7 Ensemble extinction spectrum of nanorods 68
6.8 Sample preparation with chemically produced nanoparticles 69
6.9 Simple orientation marks 69
6.10 Patterning of nanoparticles by electron beam lithography 70
6.11 Production method for nanoholes in a metal film 71

7.1 Principle of the single nanohole experiments 74
7.2 Large area SNOM image 74
7.3 Single nanohole SNOM image 75
7.4 Polarization effect in light transmission through nanoholes 76
7.5 Interference effect in light transmission through nanoholes 77

8.1 Experimental setup to measure nanodisks 80
8.2 Single particle spectra of nanodisks 81
8.3 Linewidths and dephasing times for nanodisks 82
8.4 Quality factors for nanodisks 83
8.5 Experimental setup to measure nanospheres 84
8.6 Single particle spectra of gold nanospheres 86
8.7 Linewidths, dephasing times, and quality factors of gold nanospheres . . . 88
8.8 Single particle spectra of silver nanospheres 89
8.9 Linewidths, dephasing times, and quality factors of silver nanospheres . . . 90

8.10 Setup to measure single nanorods 92
8.11 Single particle spectrum of the plasmon modes in a gold nanorod 93
8.12 Polarization dependence of the scattering spectrum of a nanorod 94
8.13 Experimentally determined linewidths, dephasing times, and quality factors of gold nanorods 95
8.14 Scattering intensity of a nanorod and a 60 nm nanosphere 96
8.15 Photo of particle pairs 98
8.16 Spectra of particle pairs 99
8.17 Comparison of single particle scattering spectra 100
8.18 Summary for gold nanodisks and -rods 101
8.19 Comparison of gold nanospheres and -rods 103
8.20 Radiative and nonradiative damping in gold nanospheres 106
8.21 Radiative quantum yield of gold nanospheres 107

9.1 Comparison of SEM and optical image 109
9.2 Measurements in liquids 110
9.3 Saccharose concentration sensor 111
9.4 Increasing sensitivity with rods or particle pairs 113
9.5 Red-shift of the particle plasmon by binding molecules to the surface . . . 115
9.6 Blue-shift of the particle plasmon by a negative particle charge 116

10.1 Sample structure and experimental principle 118
10.2 Domain structure of the liquid crystal 118
10.3 Observed red- and blue-shift of the plasmon resonance 119
10.4 Polarization dependence of the observed shift 120
10.5 Model for the observed plasmon shifts 121

LIST OF TABLES

2.1 Drude-parameters for the noble metals Au, Ag and Cu 24
2.2 Drude-parameters at optical frequencies for Au and Ag 26

8.1 Dephasing times of gold nanospheres 87
8.2 Dephasing times of silver nanospheres 91
8.3 Summary of plasmon properties in nanospheres 100

1. INTRODUCTION

Nanostructured metals show very complex and interesting optical properties. The most striking phenomenon encountered in these structures are electromagnetic resonances due to collective oscillations of the conduction electrons termed *plasmons*. Plasmon modes exist in a number of geometries and in various metals — most importantly in noble metals such as gold and silver. Under certain circumstances plasmons are excited by light, which leads to strong light scattering and absorption and an enhancement of the local electromagnetic field. The interest in plasmon modes dates back to the beginning of the 20th century (Zenneck, 1907; Mie, 1908; Sommerfeld, 1909), but recent advances in structuring, manipulating and observing on the nanometer scale have revitalized this field. Even though these technological advances were at first driven by the increasing demand for semiconductor based integrated electronic components, optical applications are now receiving increasing attention. Guiding light in integrated optical systems and interfacing with electronic components remain important challenges for research and development today. Nanostructures metals are believed to be one of the key ingredients of such future optoelectronic devices (Alivisatos *et al.*, 1998; Shipway *et al.*, 2000; Xia *et al.*, 2000).

I have investigated plasmon modes in noble metal nanostructures by near-field and far-field optical microscopy. Near-field microscopy allows the circumvention of the resolution limit imposed by the diffraction of light; this allows the to study of the electromagnetic field distribution around metal nanostructures and the interaction of light with these structures. I use this near-field technique to study the role of surface plasmons in the light transmission through holes with nanometer dimensions in planar metal films. Plasmon modes in individual metal nanoparticles are also spectrally investigated by near-field microscopy. I show that particle plasmons are even more successfully studied by far-field techniques. The nanoparticle samples can be prepared such that the interparticle spacing is large enough to distinguish the particles in the far-field. To spectrally investigate the small signal due to plasmon excitations of single nanoparticles, I have applied for the first time techniques such as total internal reflection microscopy and dark-field microscopy to such systems. This new “single particle scattering spectroscopy” method proves to be very successful for the investigation of particle plasmons. I show examples for a range of particles, namely gold and silver nanospheres, gold nanodisks and gold nanorods. These investigations give new insight into the long debated dephasing mechanism of particle plasmons and the question of the limits of simple electrodynamical theory for such nanostructured metals. In addition, the possibility of changing the environment around the metal nanoparticles has prompted the applications of the single particle scattering spectroscopy method for building optical nanosensors to probe properties such as local concentrations, bindings or redox potentials. By actively manipulating the environment electrically, the plasmon resonance of nanoparticles can be used to selectively scatter light at a desired frequency, and hence to build an optical switch based on light scattering.

This work is organized as follows: First, I will briefly review the most important electrodynamical and solid state theoretical concepts in Chap. 2 . Subsequently, I will discuss plasmon modes on planar metal-dielectric interfaces (surface plasmons) and in metal nanoparticles (particle plasmons) in Chap. 3 and Chap. 4 , respectively. In particular, I will describe general properties, applications, theoretical models, and open questions. Chap. 5 presents the experimental methods used for the studies presented in this work. These are scanning near-field microscopy and microscopic scattering spectroscopy in the far-field. Three configurations to achieve the necessary contrast for the latter method are presented: total internal reflection microscopy and dark-field microscopy in reflection and transmission. Using these near- and far-field techniques, a number of different samples are investigated, which are described in Chap. 6 .

The following chapters present results of experiments. A study of the light transmission through nanoholes investigated by near-field microscopy is presented in Chap. 7 . I show the important role of surface plasmons in this process, which has been under discussion following the discovery of an extraordinary high light transmission through regular gratings of nanoholes in metal films (Ebbesen *et al.*, 1998).

In Chap. 8 I address the important and long debated question of the amount of plasmon damping, described by the dephasing time, for different metal nanostructures. The results presented in this chapter not only give quantitative numbers for the dephasing time but allow for the first time the deduction of the underlying dephasing mechanisms. In addition, I determine the local field enhancement factors.

In Chap. 9 I present a new application of the plasmon resonance in an individual particle, namely its use as a passive sensor for changes in the local environment. I employ shifts in resonance frequency to detect local concentrations, binding events and particle charges due to redox reactions. Even though the development into real devices has yet to be proven, the results presented here show the great potential of this technique for obtaining extremely localized information on small changes in the environment of metal nanostructures.

In addition to the passive use of plasmons in metal particles as nanosensors, I actively change the plasmon frequency by manipulating the particle environment electrically (Chap. 10). This allows the control of the light scattering of the metal particles and could be used to build a spectrally selective light switch based on scattering.

2. THEORETICAL BACKGROUND

The understanding of optical properties of metal nanostructures requires both electrodynamics and solid state theory. The basic concepts of these disciplines needed for the following chapters will be briefly introduced here, starting with classical electrodynamics in matter. The material properties entering the electrodynamics treatment have to be explained by solid state theory, which will be discussed in the second part of this chapter. For more thorough treatments the reader is directed to the authoritative textbooks on electrodynamics by Jackson (1975) and on solid state physics by Ashcroft and Mermin (1976) or Kopitzki (1993).

2.1 Classical electrodynamics in matter

Electrodynamics correctly describes the time and spatial evolution of electromagnetic fields in the presence of charges, currents and any type of matter. Due to its inherent covariance it may even be used to describe relativistic effects. Only when the quantum nature of the electromagnetic field plays an important role, the classical concepts of electrodynamics have to be modified. However, in the context of the experiments described later such a quantum treatment is unnecessary.

The theory of electrodynamics developed by Maxwell in the 19th century very successfully describes the interaction of magnetic and electric fields and their propagation in free space. In its original form it fails, however, in the description of the interaction with matter. The internal structure of solids was largely unknown until the beginning of the 20th century, when the discovery of the electron, the crystal lattice structure and the advent of quantum mechanics provided the background for the description of the interaction of light with matter. Among the most important researchers who developed this description were H. A. Lorentz (*18.7.1853 Arnheim, †4.2.1928 Haarlem) and W. K. Heisenberg (*5.12.1901 Würzburg, †1.2.1976 München) (Allen and Eberly, 1975).

2.1.1 Limits

The extended electrodynamical theory includes the interaction with matter. Although it describes correctly the reaction of matter to electric and magnetic fields, some material properties (for example the complex dielectric function ε) enter as input parameters. Classical electrodynamics is therefore somewhat “inherently correct” as all unknown parameters are included in the material dependent parameters. These material parameters are *not* explained in the context of electrodynamics – they must either be taken from tabulated experimental data or explained by solid state theory. Only a microscopic perspective on the origin of the values of material properties gives insight into the "real" physical processes of the light interaction with the material, for example electron-hole-pair excitation. It is further important to realize that any *changes* in the material properties *induced* by the interaction with electromagnetic fields, cannot be explained or predicted by classical electrodynamics. Thus important optical effects such as light induced transmission or luminescence are implicitly excluded if time-independent and field-independent material properties are used.

2.1.2 Maxwell equations in matter

With these limitations in mind, I will now briefly describe the fundamental equations governing the evolution of electromagnetic fields in the present of charges, current and polarizable media: the Maxwell equations. To include situations involving matter, it is useful to distinguish external fields and fields produced by the response of the material. If we denote the local electric polarization of matter with $\vec{P}$ and the local magnetization with $\vec{M}$, we may define two new field quantities $\vec{D}$ and $\vec{H}$ by:

$$\vec{D} = \varepsilon_0 \vec{E} + \vec{P} \quad \text{and} \quad \vec{H} = \mu_0^{-1} \vec{B} - \vec{M} \tag{2.1}$$

The constants μ_0 and ε_0 are the permeability and permittivity of free space, respectively. In SI-units $\mu_0 = 4\pi \cdot 10^{-7} N A^{-2}$ and $\varepsilon_0 = 8.854 \cdot 10^{12} F m^{-1}$. The sources of these new fields $\vec{D}$ and $\vec{H}$ are the *free* charge density ρ_F and current density j_F, respectively. The Maxwell equations now read:

$$\begin{aligned} \nabla \cdot \vec{D} &= \rho_F && (2.2) \\ \nabla \cdot \vec{B} &= 0 && (2.3) \\ \nabla \times \vec{H} &= j_F + \frac{\partial}{\partial t} \vec{D} && (2.4) \\ \nabla \times \vec{E} &= -\frac{\partial}{\partial t} \vec{B} && (2.5) \end{aligned}$$

These equations are of limited use by themselves. In order to solve real problems, relations describing the response of the materials involved are needed, the so-called constitutive relations:

$$J_F = \sigma E, \quad B = \mu \mu_0 H, \quad P = \varepsilon_0 \chi E \tag{2.6}$$

with the phenomenological coefficients σ, μ, and χ (conductivity, permeability and electric susceptibility, respectively). They depend on the medium under consideration, but are assumed to be independent of the fields (the medium is *linear*), and independent of position and direction (homogeneous and isotropic media). They are, however, frequency dependent. The time dependence of the involved fields can be assumed to be harmonic, e.g. $E(\vec{r}, t) = E_\omega(\vec{r})\, e^{-i\omega t}$. More complicated time dependent fields can be written as superposition of such fields (Fourier synthesis)(i). Introducing all these equations into the

---

(i) The field quantities are extended to complex values for mathematical reasons. The actual physical fields are represented by the real parts of these functions.

Maxwell equations, these simplify in media without free charges to:

$$\nabla \cdot (\varepsilon \vec{E}) = 0 \tag{2.7}$$

$$\nabla \cdot \vec{B} = 0 \tag{2.8}$$

$$\nabla \times \vec{H} = -i\,\omega\varepsilon\,\vec{E} \tag{2.9}$$

$$\nabla \times \vec{E} = +i\,\omega\mu\,\vec{H} \tag{2.10}$$

with the complex dielectric function $\varepsilon = \varepsilon_0(1+\chi) + i\,\sigma\omega$. The distinction between bound charges (described by χ) and free charges (described by σ) is somewhat arbitrary since the imaginary part of χ also contributes to the imaginary part of ε.

This set of equations (together with the appropriate boundary conditions and the conservation of charge and energy) are sufficient to solve the time and spatial evolution of electromagnetic fields in the presence of matter.

I should mention another quantity, the polarizability α, which is closely related to the electric susceptibility χ. But whereas χ describes the polarization induced in the medium by the *local field*, α relates the induced polarization to the *external field*.

2.2 Solid state theory for optical constants of metals

The material properties needed for the electrodynamical calculations have to be calculated using solid state theory. A simple model for metals was developed by Drude (1900) based on the kinetic gas theory. It assumes independent and free electrons with a common relaxation time. Sommerfeld incorporated corrections originating from the Pauli-exclusion principle (Fermi-Dirac velocity distribution). This so-called free-electron model was later modified to include minor corrections from the band-structure of matter (effective mass) and termed quasi-free-electron model.

This Drude-Sommerfeld model describes very successfully many (but not all!) properties of metals despite its drastic assumptions. At optical frequencies it often fails due to the presence of interband transitions, as we will see by comparison of calculated parameters with measured material properties. Nevertheless it is important to have the basic concepts of the Drude-Sommerfeld model in mind to analyze the experiments described later in this work.

2.2.1 Drude-Sommerfeld model

The basic picture of the properties of metals in the framework of this theory is a gas of independent, point-like electrons. These electrons move freely in between independent collisions with unspecified collision centers (lattice ions, other electrons, defects, phonons, etc.), which occur with an average rate of $\gamma_0 = \tau^{-1}$ with τ being the so-called electron relaxation time. Each collision leads to a complete loss of directional information and results in a random orientation of the electron velocity afterwards.

In an external field, the electrons are accelerated inbetween collisions resulting in a drift motion. In reality, only electrons near the Fermi level contribute, because the Pauli-exclusion principle does not allow deeper lying electrons to change their electronic state. Band-structure corrections lead to a modification of this motion. These corrections are customarily incorporated into an effective mass m^*, which is in general different from the free-electron mass m_e.

Many (but not all) properties of real metals, including their optical properties as described by the frequency dependent dielectric function $\varepsilon(\omega)$, are surprisingly well predicted from this simple model. The resulting equation is:

$$\varepsilon(\omega) = \varepsilon_\infty - \frac{\omega_p^2}{\omega(\omega + i\gamma_0)} \approx \varepsilon_\infty - \frac{\omega_p^2}{\omega^2} + i\frac{\gamma_0\,\omega_p^2}{\omega^3} \tag{2.11}$$

with ω_p the so-called plasma frequency and γ_0 the electron relaxation rate. ε_∞ includes the contribution of the bound electrons to the polarizability and should have the value of 1 if only the conduction band electrons contribute to the dielectric function.

The plasma frequency is given by $\omega_p = \sqrt{n\,e^2/\varepsilon_0 m^*}$ with n and m^* being the density and effective mass of the conduction electrons, respectively. The electron relaxation time can be calculated from the DC conductivity σ by $\tau = \sigma\, m^*/ne^2$. In Tab. 2.2.1 these so-called Drude-parameters are provided for the noble metals Au, Ag and Cu.

	Au	Ag	Cu
$n/\,\mathtt{m}^{-3}$	$5.90 \cdot 10^{28}$	$5.76 \cdot 10^{28}$	$8.45 \cdot 10^{28}$
$\sigma/(\Omega\,\mathtt{m})^{-1}$	$4.9 \cdot 10^{7}$	$6.6 \cdot 10^{7}$	$6.5 \cdot 10^{7}$
m^*/m_e	0.99	0.96	1.49
$\hbar\omega_p/\,\mathtt{eV}$	9.1	9.1	8.8
$\tau/\,\mathtt{fs}$	29	40	40

Tab. 2.1: Drude-parameters for the noble metals Au, Ag and Cu. DC-conductivity σ and electron density n from Kopitzki (1993), effective mass m^* from Johnson and Christy (1972).

2.2.2 Empirical bulk values for noble metals

The optical properties of metals can be determined experimentally by reflection and transmission measurements on clean surfaces under ultrahigh vacuum conditions. They show a somewhat ambiguous behaviour: whereas the low energy values are well described by the Drude-Sommerfeld model, additional contributions are present at higher energies. The reason for this are the excitation of electrons from deeper bands into the conduction band, the so-called interband excitations. In noble metals the electrons originate from completely filled d-bands, which are relatively close to the Fermi-energy. An additional reason for the derivation from the Drude-Sommerfeld behaviour is that the conduction band is increasingly non-parabolic for higher energies.

The example for gold is shown in Fig. 2.1 , where the real and imaginary part of the electrical permeability ε is given as a function of light frequency(ii). Here, strong deviations

---

(ii) Throughout this work, frequencies (ω) are converted to energies by the Planck relation $E = \hbar\omega$ and given in units of electron volts (`eV`).

from the quasi-free-electron model occur above 1.8 `eV`, especially for the imaginary part. Unfortunately, the imaginary part is experimentally given with a large relative error. The reason is the strong dependence on the absolute transmission value, which is difficult to determine. The same applies for the dielectric function of silver shown in Fig. 2.2 : the real part is well described by the model, the imaginary part shows deviations due to interband transitions.

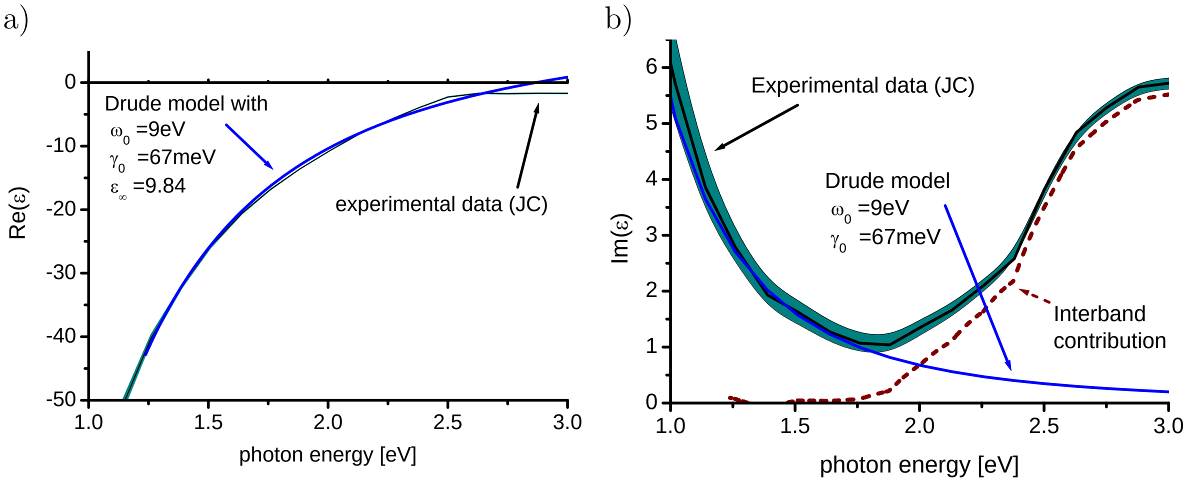

Fig. 2.1: a) Real part of the dielectric function of gold; b) imaginary part. Experimental data (JC) from Johnson and Christy (1972) compared to calculated values using the quasi-free-electron or Drude model with the parameters indicated in the graph. The shaded area around the experimental data indicates the measurement uncertainty. The interband contribution (broken line) is calculated from the difference of the experimental data to the Drude model.

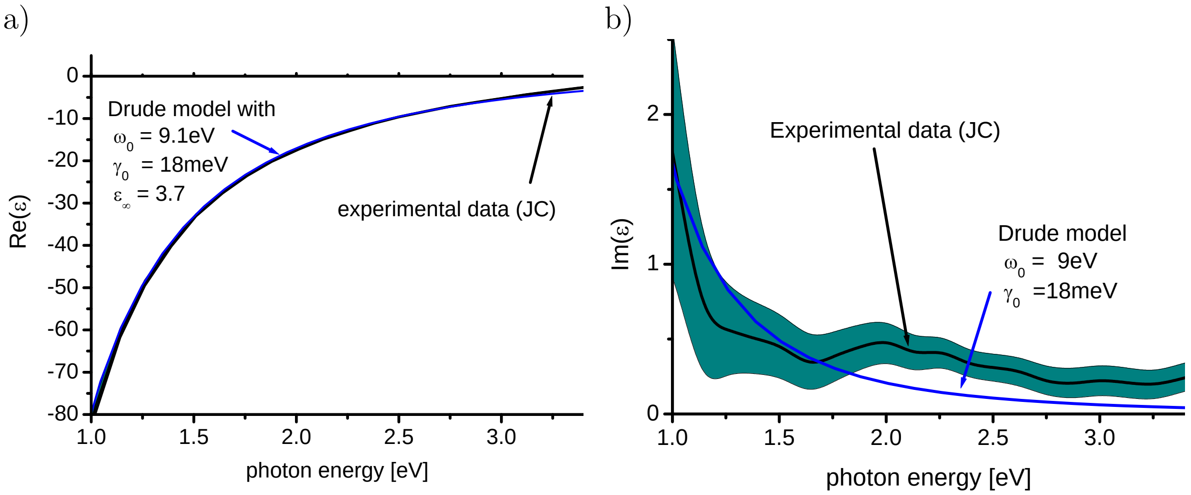

Fig. 2.2: a) Real and b) imaginary part of the dielectric function of silver (JC) from Johnson and Christy (1972) compared to calculated values using the quasi-free-electron or Drude model with the parameters indicated in the graph. The shaded area around the experimental data indicates the measurement uncertainty.

Determining Drude parameters by fitting to experimentally determined dielectric functions (at optical frequencies) leads to somewhat different values than those derived from DC values. In Tab. 2.2.2 some values determined by such a fitting procedure are quoted and should be compared to Tab. 2.2.1 .

	Au	Ag	Au	Ag	Au	Ag
$\hbar\omega_p/\,\mathtt{eV}$	9.0	9.1	8.4	8.75	8-10	8.3-9.2
$\tau/\,\mathtt{fs}$	10	36	6-19	8.6	4-26	15-23
ε_∞	9.84	3.7	6.5-7.5	4.45		
E_{IB}	1.75	1.75	1.5	1.5		
reference	this work		PW		Land./Börn.	

Tab. 2.2: Drude-parameters at optical frequencies for Au and Ag. Interband contributions below E_{IB} are taken into account by ε_∞. Values in this work taken from fits in the region $1.4 < E/\,\mathtt{eV} < 1.75$ of data reported by Johnson and Christy (1972) (cf. Fig. 2.1), PW: Winsemius (1972), Land./Börn.: collection of values by Foiles (1985).

2.2.3 Adjustment for very small particles

The values presented above for the dielectric function of gold and silver were determined for bulk material. Surface scattering leads to additional collisions of the conduction electrons with a rate τ^{-1}, proportional to the Fermi-velocity v_F (about 1.4 nm/fs in Au and Ag). This effect becomes important in small metal particles with high surface to volume ratio. The additional damping $\gamma_{\mathrm{surface}}$ is given empirically by (Kawabata and Kubo, 1966; Genzel and Kreibig, 1980):

$$\tau_{\mathrm{surface}}^{-1} = A\ v_F/r \tag{2.12}$$

with the particle radius r and an empirical parameter A describing the loss of coherence by the scattering event. A is found to be dependent on surface chemistry, i.e. the type and strength of chemical interaction of adsorbates to the surface. Typical values in silver are between 0.1 and 0.7 (Persson, 1993; Charle *et al.*, 1998).

Since all experimental studies of surface scattering rates in very small particles were undertaken on large ensembles, inhomogeneous broadening effects have probably led to a strong overestimation of the surface scattering damping. Even though some authors try to account for this by independently determining the inhomogeneous size distribution, these values should be regarded with some scepticism.

2.3 Quasi-particle lifetime and linewidth of resonances

One of the main subjects of this work is the study of dephasing times of plasmons in metal nanoparticles (Chap. 8). In principle, such dephasing could be studied in time-domain by exciting the plasmon resonance by an ultashort laser pulse and determining the decay of some nonlinear optical effect induced by a second laser pulse by varying the temporal separation between the two laser pulses. Such time resolved techniques are very difficult to conduct on metal nanoparticles because of the extremely fast dephasing times encountered for plasmons in such particles (on the order of 1-10 fs). Another important problem arising in this context are effects due to the inhomogeneous broadening of the particle size and shape.

Instead of measuring the plasmon dephasing in time-domain, it is also possible to determine dephasing times by investigating their spectrum in frequency-domain (Demtröder, 1996). Since frequency and time are connected by the Fourier transformation, a temporal decay leads to a spectral broadening of any oscillating system. I will briefly discuss this in the following section. Subsequently, I want to address the spectral response of an continuously, externally driven oscillator; this closely models the situation for the experiments described in Chap. 8 . At the end of this chapter I will come back to the problem of inhomogeneous broadening and its influence on measured dephasing times.

2.3.1 Fourier-transformation

Time and frequency are closely connected through the Fourier transformation $\mathcal{F}$. Let us investigate the example of an oscillating electric field $E(t)$ with an eigenfrequency ω_0. If the oscillation is damped and decays exponentially with a time constant T, the Fourier transformation $\mathcal{F}$ tells us that the frequency spectrum observes a so-called resonance lineshape or Lorentz-lineshape:

$$E(t) \;=\; \left(E_0 e^{-i\omega_0 t}\right) e^{-t/T} \tag{2.13}$$

$$\Rightarrow E'(\omega) \;=\; \mathcal{F}\left(E(t)\right) = \frac{E_0}{\sqrt{2\pi}} \frac{1/T}{(\omega-\omega_0)^2 + (1/T)^2} \tag{2.14}$$

A Lorentz line is usually characterized by its center position ω_0 and full-width-at-half-maximum (FWHM) $\Delta\omega$. The Planck relation $E = \hbar\omega$ is used to express frequencies in units of energy in this work — the FWHM in units of energy is denoted by $\Gamma = \hbar\Delta\omega$. The halfwidth follows from Eqn. 2.14 by looking for the frequencies at which E' reaches half its maximum value. The maximum is at $\omega = \omega_0$, so the denominator in Eqn. 2.14 has the value $1/T$. E' will have half its maximum value for the denominator $2 \cdot (1/T)$, i.e. for $(\omega - \omega_0)^2 = 1/T$. Therefore

$$\Gamma/\hbar = 1/T + 1/T = 2/T \qquad \Leftrightarrow \qquad T \cdot \Gamma = 2\hbar \tag{2.15}$$

An example for this relations is shown in Fig. 2.3 . Because the Planck constant $\hbar$ has the value 0.658212 `eV fs`, we have the simple relation

$$\frac{T}{\texttt{fs}} = \frac{1316}{\Gamma/\,\texttt{meV}} \tag{2.16}$$

to convert the full linewidth at half maximum to a decay time.

2.3.2 Driven harmonic oscillator

The relation 2.15 follows also by looking at an externally driven damped harmonic oscillator described by

$$\ddot{x} + (2/T)\;\dot{x} + \omega_0^2\;x = F_{\text{ext}} \tag{2.17}$$

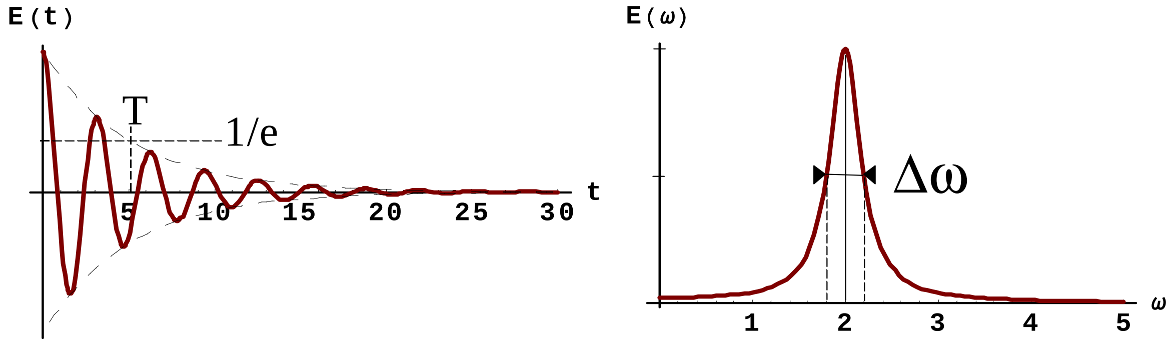

Fig. 2.3: A damped oscillation in time (left) corresponds via the Fourier transformation to a Lorentz-shaped peak in the frequency spectrum (right). Here, an example for an oscillation with frequency $\omega = 2$ and damping time T=5 is shown. The full width at half maximum $\Delta\omega$ of the resonance in frequency space is $2 \cdot (1/T) = 0.4$.

In the case of no external excitation F_{ext} and small damping $(2/T)$, this is the equation of an oscillator with frequency ω_0 decaying with time-constant T. If $F_{\text{ext}} = F_0\, e^{i\omega t}$, the test function $x = x_0\, e^{i\omega t+\alpha}$ leads to the condition:

$$-\omega^2 + (2/T)\; i\,\omega + \omega_0^2 = (F_0/x_0)\; e^{-\alpha} \tag{2.18}$$

Solving it for α separately in the imaginary and real part, it leads to the resonant-like oscillation amplitude x_0:

$$x_0 = F_0 / \sqrt{(\omega_0^2 - \omega^2)^2 + \omega^2 \left(\frac{2}{T}\right)^2} \tag{2.19}$$

and a phase-shift ϕ between driving force and oscillation amplitude:

$$\tan\phi = \frac{\omega\ (2/T)}{\omega_0^2 + \omega^2} \tag{2.20}$$

For weak damping, the maximum amplitude is approximatively at $\omega_{\max} = \omega_0$. At $\omega = \omega_0 \pm (1/T)$ the amplitude has fallen to half this value. The full width at half-maximum $\Delta\omega$ of this resonance is therefore given by the same relation as derived for the Fourier spectrum of a damped oscillator (Eqn. 2.15):

$$\Delta\omega = 2/T \tag{2.21}$$

The amplitude maximum relative to the value at $\omega = 0$ defines the quality factor Q:

$$Q = \frac{x_0(\omega = \omega_{\max})}{x_0(\omega = 0)} = \frac{F_0\,/\,[\,\omega_0\,(2/T)\,]}{F_0/\omega_0^2} = \frac{\omega_0}{(2/T)} = \frac{\hbar\omega_0}{\Gamma} \tag{2.22}$$

The mean energy transfer from the driving force to the oscillator (temporarily averaged over many oscillation periods) follows(iii) the same functional relationship with a maximum at ω_0 and a full width at half maximum (FWHM) of $\Delta\omega = 2/T$ (Demtröder, 1996, p. 61).

(iii) taking the *phase* between driving field and oscillator into account

It is important to keep in mind that the oscillator's energy (=ampitude squared) decays with a rate T_1^{-1} twice as fast as the oscillation amplitude decay rate T_2^{-1}! Note that the times stated above refer to amplitude decay times T_2. We have therefore:

$$T_1 = T_2/2 = 1/\Delta\omega \tag{2.23}$$

2.3.3 Deducing lifetimes

It is, however, not trivial to deduce time constants from measurements. The main problem is inhomogeneous broadening of many oscillating dipoles in the sample with slightly different resonance frequencies. This process is referred to as "free-induction decay".

In the time domain, destructive interference of the oscillating dipoles leads to a faster decay of the overall, macroscopic polarization than the decay of the individual dipoles. If we denote the decay time of an individual dipole by T_2 and the ensemble dephasing time T', the dephasing time T^* due to this inhomogeneous effect is given by:

$$\frac{1}{T'} = \frac{1}{T_2} + \frac{1}{T^*} \tag{2.24}$$

In frequency domain, inhomogeneous broadening gives an additional contribution Γ_{inhom} to the ensemble linewidth Γ_{ensemble} (the symbol $\oplus$ stands for a the correct mathematical 'addition' or folding):

$$\Gamma_{\text{ensemble}} = \Gamma_{\text{hom}} \oplus \Gamma_{\text{inhom}} \tag{2.25}$$

Both linewidth and dephasing times obtained from simple linear experiments on inhomogeneous ensembles are thus meaningless with respect to properties of the individual oscillator. For a *single* resonance of an *individual* oscillator measured for example in single particle spectroscopy, inhomogeneous broadening is obviously no problem, so the measured linewidth is the homogeneous linewidth, i.e. the intrinsic oscillator dephasing time T_2.

Further conceptual complications arise in the case of the eigenmode of the collective oscillation of the conduction electrons in metal nanoparticles, the so-called particle plasmons. These particle plasmons will be discussed in Chap. 4 . I just want to point out here the distinction between collective and single-electron dephasing in the overall dephasing of such a quasi-particle associated with a collective oscillation of many electrons.

The collective oscillation may decay by elastic and inelastic *collective* processes. Elastic processes lead to a change in phase of the collective oscillation without changing the oscillators energy. Such a process is called "pure dephasing". Inelastic processes reduce the oscillators energy or the population of its quantum state, for example by emission of a photon. In general, the population dephasing time denoted by T_1 differs from the overall dephasing time T_2 due to possible elastic or "pure dephasing" processes.

In contrast to viewing the collective oscillation of the electrons in this collective picture, we can use the so-called independent electron approximation. In such an independent electron model, the interaction of an electron with the other electrons is described by time independent corrections to quantities such as the relaxation rate or the effective mass. The independent electron approximation is commonly used in the description of optical, electrical and thermodynamical properties of metals (Ashcroft and Mermin, 1976). It will also be used to describe the inelastic, nonradiative decay of the particle plasmon oscillation(iv). For example, a conduction band electron may scatter inelastically with a d-band electron creating an electron-hole-pair. This does not imply that the energy of the whole plasmon is mysteriously localized into a single electron-hole-pair. Instead, the overall oscillation is viewed as a superposition of many single-electron-oscillations which then dephase by such processes. Since it is difficult to always make a clear distinction between collective and single-electron processes, this topic has been repeatedly discussed — and will surely be discussed further — with respect to particle plasmon dephasing.

(iv) I will even argue that my experimental findings can be explained entirely by photon emission and single-electron dephasing — without any further *collective* dephasing mechanism.

3. PLASMON MODES ON PLANAR METAL-DIELECTRIC INTERFACES – *SURFACE PLASMONS*

The eigenmodes of collective oscillations of the quasi-free electrons in metals are called *plasmons*. Because electrons carry a charge, these oscillations are inherently associated with an electromagnetic field. Therefore a theoretical description has to include this interplay of charges and fields. The boundary conditions for electromagnetic fields lead to different conditions for the occurrence of plasmons for the cases of bulk material, planar metal-dielectric interfaces and metal particles. It is therefore useful to distinguish these modes by speaking of bulk, surface or particle plasmons, respectively. Particle plasmons will be treated in the next chapter. Here, I will focus on surface plasmons, i.e., the electromagnetic eigenmodes at planar metal-dielectric interfaces.

Historically, these surface plasmon modes were studied as early as the beginning of the 20th century by Zenneck (1907) and Sommerfeld (1909) in connection with wireless telegraphy and hence are sometimes called *Zenneck modes* (e.g. Keilmann, 1981). These early investigations focused on frequencies much smaller than that of visible light, where the optical properties of metals are very well described in terms of the Drude-Sommerfeld model, and the phenomenological difference of plasmonic surface waves and plane electromagnetic waves in free-space is very small. Because this work deals with *optical* properties, these early works are therefore of limited use despite the fact that the mathematical treatments are similar to those in the optical regime.

3.1 Properties and applications

Surface plasmons are electromagnetic modes bound to metal-dielectric interfaces, involving charges in the metal and electromagnetic fields in both media. The field intensity in the metal as well as the dielectric medium falls off exponentially in the direction normal to the surface. In the plane of the interface, the field intensity and charge distribution in the metal propagates as a longitudinal wave along the surface. Hence, surface plasmons propagate along the interface with electromagnetic fields, energy and charges highly localized within the interface area. Their properties depend strongly on the exact properties of both the metal (complex dielectric function, corrugations, roughness) and the dielectricum (refractive index).

The strong localization of electromagnetic energy along the metal-dielectric interface can be used to guide light in small structures (Krenn *et al.*, 2001). The high sensitivity of surface plasmons to the metal surface structure provides a tool to study properties such as surface roughness. The sensitivity to the local refractive index of the dielectric close to the interface is used to detect chemical binding by taking a liquid as dielectric. When solvents present in this liquid bind to the metal-dielectric interface, they change the refractive index at the interface, which leads to a measurable change in surface plasmon properties. This method allows not only to detect binding events but also to study binding kinetics (see e.g. the following reviews Canziani *et al.*, 1999; Mullett *et al.*, 2000; Rich and Myszka, 2000, and references therein).

3.2 Electrodynamical theory

For the understanding of surface plasmons, it is very useful to study the results of simple electrodynamical theory applied to an ideal model interface. Obviously this approach neglects many real effects due to the exact surface properties, screening effects, quantum mechanical corrections, etc.. However, the main features of surface plasmons can be understood in this simple model.

The main result obtained for plasmons at a flat metal-dielectric interface is a relation between the lateral momentum $k_{\|}$ and the frequency $\hbar\omega$, the so-called *dispersion*:

$$k_{\|}^2 = k_{\text{photon}}^2 \frac{\varepsilon_r}{\varepsilon_r + 1} \tag{3.1}$$

ε_r is the dielectric function of the metal ($\varepsilon_{\text{metal}}$) relative to the dielectric function of the dielectricum, i.e. $\varepsilon_r = \varepsilon_{\text{metal}}/\varepsilon_{\text{dielectricum}}$. The photon momentum k_{photon} is given by the relation $k_{\text{photon}} = \omega/c$. The derivation of Eqn. 3.1 is lengthy and often oversimplified in literature (e.g. Raether, 1988)(i). An example of the dispersion of surface plasmons at a silver-air interface is shown in Fig. 3.1 together with the dispersion of plane electromagnetic waves in air (photons). As long as the dielectric function for the metals is strongly negative (which is generally the case for metals), the momentum of surface plasmons is larger than that of plane waves. This is seen in Eqn. 3.1, because the denominator is smaller than the numerator for strongly negative ε_r. The high energy modes shown in Fig. 3.1 should be neglected because silver does not behave like a metal at those frequencies — the optical properties are dominated by excitations of electrons from deeper lying bands. These modes also propagate into the bulk and are thus not true surface modes. The momentum of the surface bound modes is slightly larger than that of photons for small energies. The difference increases for higher energies until it reaches the limit of almost stationary waves. The uncertainty in momentum originating from the finite lifetime of these mode is indicated by the width of the line in Fig. 3.1. This shows that the momentum of surface plasmon modes is not well defined for energies approaching the stationary limit.

The surface plasmons discussed above are coupled oscillations of electron density and electromagnetic field. The correct term for this is *surface plasmon polariton*. Surface plasmons are, strictly speaking, the (unphysical) electron density oscillation modes without the coupling with the field. Their energy corresponds to the limiting stationary value

---

(i) A rigorous derivation can be found in Güntzer (1999).

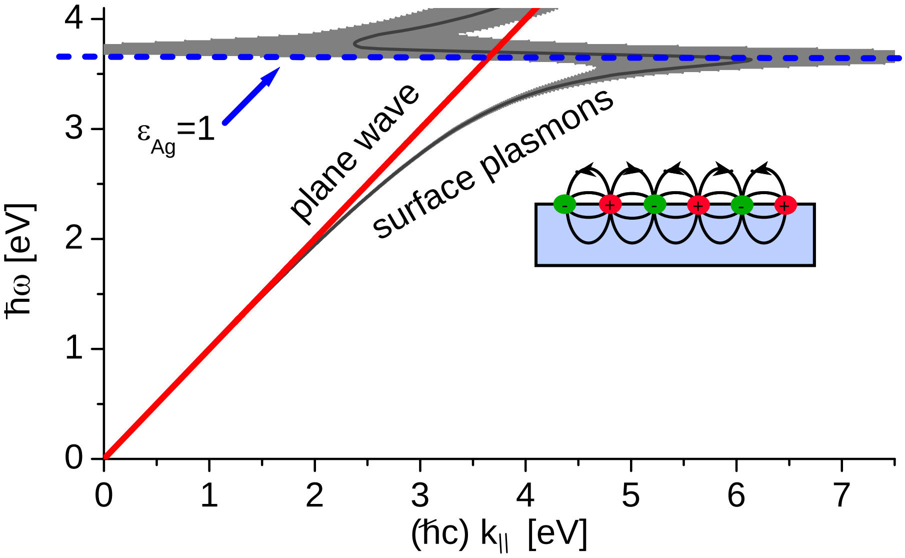

Fig. 3.1: Dispersion of plasmons at an air-silver interface. The width of the line represents the uncertainty of the momentum due to finite lifetime. The low energy modes are true surface plasmons (inset), the high energy modes propagate into the bulk. Here, these high energy modes are not considered any further because the properties of silver are not metal-like at these frequencies. The dotted line presents the stationary limit of nonpropagating surface plasmons. The large width of the line at this energy indicates its strong damping.

in Fig. 3.1 , which is given by demanding $\varepsilon_r(\omega) = 1$. Because the distinction of surface plasmons and surface plasmon polaritons is not central in the context of this work I will just speak of surface plasmons when referring to the coupled mode.

3.3 Surface plasmon excitation by light

Because the surface plasmon dispersion is below the photon dispersion (Fig. 3.1) for all energies, it is clear that surface plasmons cannot be be excited by plane waves incident on the interface from the dielectricum because regardless of the angle of incidence, the surface plasmon modes of the same frequency have a larger momentum. In order to excite surface plasmons, additional momentum has to be somehow provided. In practice, this is usually done either by placing a regular grating structure at the interface (which also disturbs the plasmon mode) or by letting the excitation light pass through a medium with a high refractive index (e.g. a prism). In the latter case, the excitation light can either come from the side of the dielectricum (so-called Otto-configuration, Otto (1968)) or from the metal side (Kretschmann configuration, Kretschmann (1972)), cf. Fig. 3.2 . In the Otto configuration, there has to be a small gap between the dielectric and the metal surface, because otherwise the surface plasmon dispersion would also be altered. In the Kretschmann configuration the metal film has to be very thin in order to allow the light field to reach through the film.

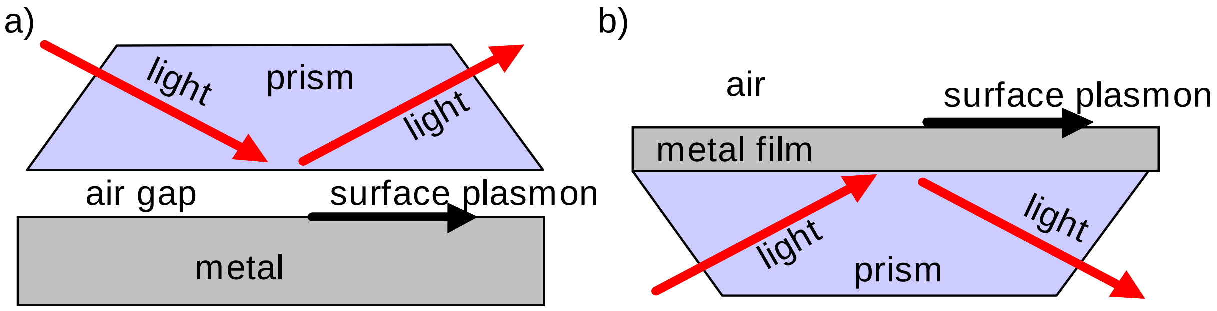

Fig. 3.2: a) Otto configuration b) Kretschmann configuration

3.4 Interaction with nanostructures

It is well known that surface plasmons propagating along a flat metal-dielectric interface are scattered and reflected by defects such as dimples, holes, rims, or dips. Numerous investigators have studied the resulting local field distribution both theoretically and experimentally. In the experimental configuration most commonly used, surface plasmons are excited non-locally by plane waves and locally detected by either photon scanning tunneling microscopy (PSTM) (Marti *et al.*, 1993; Smolyaninov *et al.*, 1996, 1997; Krenn *et al.*, 1997) or apertureless scanning near-field optical microscopy (Dawson *et al.*, 1994; Specht *et al.*, 1992; Kryukov *et al.*, 1997). An alternative approach was used by Hecht *et al.* (1996) who *locally* launched surface plasmons by the tip of a scanning near-field optical microscope (SNOM) in illumination mode. In both configurations the surface plasmons on the two surfaces of the metal film are coupled, because the film thickness is smaller than the penetration depth of the surface plasmons.

3.5 Surface plasmon assisted light transmission through nanoholes

Much interest has been attracted by recent reports (Ebbesen *et al.*, 1998; Ghaemi *et al.*, 1998) that light transmission through arrays of subwavelength sized holes in otherwise optically opaque metal films can be much larger than expected from diffraction theory for isolated holes (Fig. 3.3). This fascinating effect has been suggested for potential use in optical applications such as filters or displays (Tae Jin *et al.*, 1999). This enhanced transmission has been attributed to surface plasmons excited by light incident on the hole array. These surface plasmons are believed to couple through the holes to the other side of the film (Grupp *et al.*, 1999). Such a mechanism has also been proposed in earlier investigations of far-infrared transmission through hole arrays (Keilmann, 1981). However, the precise nature of the surface plasmon interaction with the subwavelength-sized holes is not fully understood and is still under investigation (Fischer, 1986; Schröter and Heitmann, 1998; Treacy, 1999; Grupp *et al.*, 1999; Kim *et al.*, 1999; Grupp *et al.*, 2000; Martin-Moreno *et al.*, 2001; Hohng *et al.*, 2001; Salomon *et al.*, 2001).

I report here near-field optical experiments (Chap. 7) which show directly and unambiguously that excitation and lateral propagation of surface plasmons support light transmission through nanoholes.

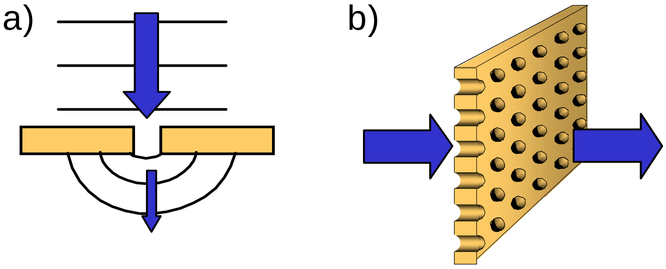

Fig. 3.3: a) single hole transmission is very small for subwavelength sized holes b) an array of such holes sometimes has very large transmission even exceeding unity when normalized to the total hole area.

4. PLASMON MODES IN METAL NANOPARTICLES — *PARTICLE PLASMONS*

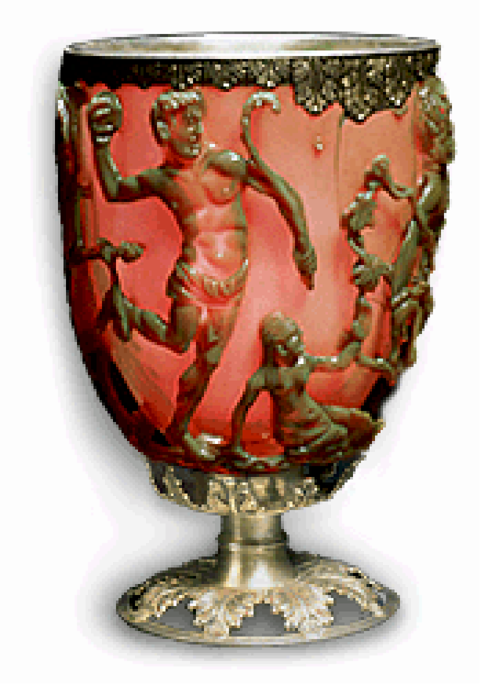

Fig. 4.1: Lycurgus cup, 4th century AD (now at the British Museum, London). The colors originates from metal nanoparticles embedded in the glass. At places, where light is transmitted through the glass it appears red, at places where light is scattered near the surface, the scattered light appears greenish.

Gold and silver particles with diameters on the nanometer scale show very bright colors. These bright colors have fascinated people for many centuries. One example of a historical application is the staining of church windows in the Middle Ages or the beautiful Lycurgus cup manufactured in Roman times — now at the British Museum, London (Fig. 4.1). In modern times gold and silver nanoparticles have found many new applications such as labeling for transmission electron microscopy (TEM) in the biological sciences. Strong research efforts are still underway to exploit new applications of these particles. Most of the more recent literature is summarized in the book by Kreibig and Vollmer (1995) and in review articles by Mulvaney (1996) as well as Link and El-Sayed (2000).

The bright colors of noble metal nanoparticles are due to the resonant excitation of a collective oscillation of the conduction band electrons in the particles termed *particle plasmon*. The particle plasmon mode is related to surface plasmon modes at planar metal surfaces as discussed in the previous chapter. There are, however, some fundamental differences. For example, the singular resonance frequency for particle plasmons opposed to the dispersion in energy and momentum for surface plasmons. In order to make a clear distinction between these plasmon modes, I use the term particle plasmon for plasmons in nanoparticles and surface plasmons for plasmons at extended planar metal surfaces(i).

(i) In the literature, particle plasmons are sometimes also called surface plasmons or localized surface plasmons.

4.1 Simple semi-classical model

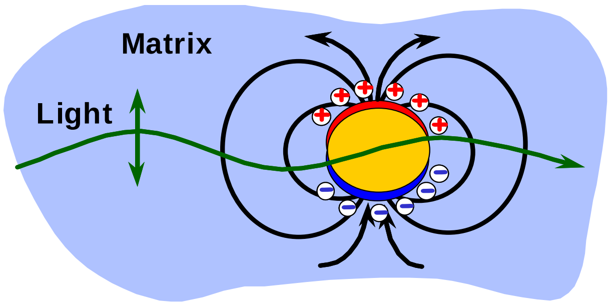

Fig. 4.2: Schematic view of the excitation of a particle plasmon oscillation in a metal nanoparticle by an external light field.

Many properties of particle plasmons are qualitatively understood in the following semi-classical model (Fig. 4.2). Since the diameter of a nanoparticle is on the order of the penetration depth of electromagnetic waves in metals$^{(\mathrm{ii})}$, the excitation light is able to penetrate the particle. The field inside the particle shifts the conduction electrons collectively with respect to the fixed positive charge of the lattice ions. The electrons build up a charge on the surface at one side of the particle. The attraction of this negative charge and the positive charge of the remaining lattice ions on the opposite side results in for a restoring force. If the frequency of the excitation light field is in resonance with the eigenfrequency of this collective oscillation, even a small exciting field leads to a strong oscillation. The magnitude of the oscillation depends only on the damping involved, which can be both radiative and nonradiative. The resonance frequency is mainly determined by the strength of the restoring force. This force depends on the separation of the surface charges, i.e. the particle size, and the polarizability of the medium between and around the charges, which depends on the embedding medium and the polarizability of the core electrons of the metal particle. The alternating surface charges effectively form an oscillating dipole, which radiates electromagnetic waves. This simple model for particle plasmons is reminiscent of an “optical antenna”.

4.2 Properties and applications

As mentioned above, the most striking consequence of particle plasmons excitation is the strong color that noble metal particles exhibit, which depends on size, shape and environment of the particles. In this section I briefly mention some applications of plasmons in metal nanoparticles. The most well-known application is to stain glass, which dates far back in history and is still used today (“Ruby glass”).

A very important application in the biological sciences is the use of gold nanoparticles or colloids to label organic substances or biological material primarily for electron microscopy. The advantage here is that gold has a very high contrast compared to organic substances due to its high electron density, and is therefore easily distinguished in electron microscopy. Because of its inert nature, it is possible to specifically bind gold colloids to a desired target without altering the structure (Hayat, 1989). Recently this gold labeling technique has also been applied to detect specific biological substances (here DNA) with light microscopy (Taton, 2000). It should be noted that no use is made of the plasmon oscillation in these applications.

The strong electromagnetic field around the particles, which can be much higher than the

---

(ii) The penetration depth at optical frequencies is ca. 30 nm for gold and silver exciting light field at the particle plasmon frequency, is used to enhance nonlinear optical effects such as surface enhanced Raman scattering (SERS) (Moskovits, 1985; Kneipp *et al.*, 1996; Nie and Emory, 1997). The exact mechanism of this SERS enhancement remains unclear, but field enhancement seems to be one of the factors (Shalaev, 2000). Other nonlinear applications such as generation of higher harmonics or white light are currently discussed.

The resonance frequency of particle plasmons is sensitive to the polarizability (i.e., the refractive index) of the surrounding medium. All sensor applications of particle plasmons reported to date have used large ensembles of particles (Kubitschko *et al.*, 1997; Takai, 1998; Englebienne, 1998; Gluodenis *et al.*, 1999; Bauer *et al.*, 1999). It has been found that in this cases the particle plasmon sensors compare badly with the well established technique of surface plasmon resonance (SPR) shifts at planar metal surfaces (cf. for example the recent review by Mullett *et al.* (2000). It remains challenging to explore its use as a *local* sensor as suggested in (Klar *et al.*, 1998).

As an additional possible application, the confinement of electromagnetic energy in a very small region in space on plasmon excitation has been suggested to guide light in future photonic devices (Krenn *et al.*, 2001).

4.3 Light scattering and absorption by metal nanoparticles

As I have mentioned above, metal nanoparticles strongly absorb and scatter light at the plasmon resonance frequency, which results in their strong color. The ratio of scattering to absorption changes dramatically with size, as demonstrated in Fig. 4.3 . Large particles scatter light very efficiently, whereas the color of small particles is mainly caused by absorption. Since the the color of most strongly colored substances (dyes) is due to absorption, scattering is usually neglected and the change in transmission, the so-called *extinction*, is solely attributed to absorption. For metal particles with dimensions above 30 nm, scattering becomes very important.

Light scattering, absorption and extinction of particles is described by frequency dependent cross-sections C_{sca}, C_{abs}, and $C_{\text{ext}} = C_{\text{sca}} + C_{\text{abs}}$. The amount of scattered light is then given by:

$$I_{\text{sca}}(\omega) = \frac{I_0(\omega)}{A} \cdot C_{\text{sca}}(\omega) \tag{4.1}$$

if a particle is illuminated with the light intensity per area $I_0(\omega)/A$. Usually these cross-sections are normalized to the particle's geometrical cross-section (πr^2 for spherical particles with radius r) to give the so-called efficiencies Q_{sca}, Q_{abs}, and Q_{ext}. For macroscopic objects, these efficiencies have the value of $Q_{\text{sca}} = 1$, $Q_{\text{abs}} = 1$, and $Q_{\text{ext}} = 2$[iii]. It is also useful to define the radiative quantum yield η, which is the ratio of scattered light to the extinction, i.e.

$$\eta = C_{\text{sca}}/C_{\text{ext}} = Q_{\text{sca}}/Q_{\text{ext}} \tag{4.2}$$

[iii] The apparent paradoxon that twice as much light is taken out of a beam incident on a macroscopic object than incident on its geometrical area is well understood (Bohren and Huffman, 1982).

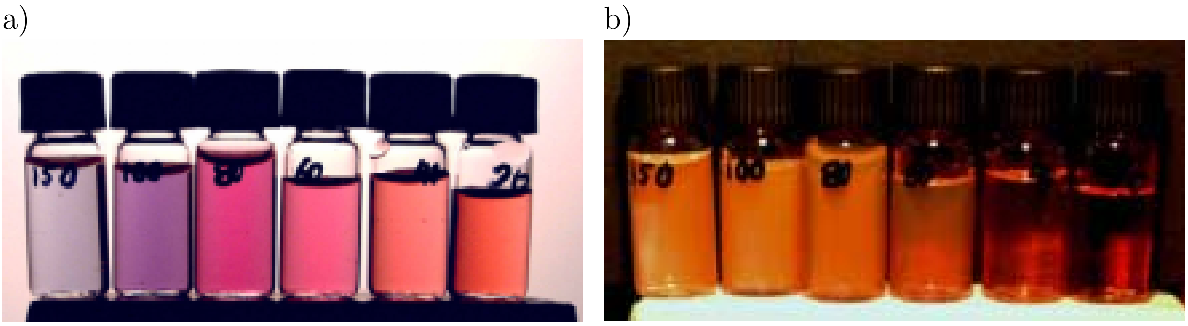

Fig. 4.3: a) Suspensions of spherical gold particles with various diameters ($150, 100, 80, 60, 40, 20\,\mathtt{nm}$ from left to right) in water. Illumination from behind; b) illumination from the front. The (complementary) color in a) is due to extinction, in b) due to diffuse back-scattering. Despite the extremely low concentration of gold particles ($< 10^{-2}$ weight %), the suspensions show bright colors, especially in transmission (a). The difference in transmission and backscattering is due to different scattering and absorption behaviour of small and large gold particles. A size effect on resonance frequency is observed.

From Fig. 4.3 it is clear that η has to increase dramatically with particle diameter, because it is almost zero for $20\,\mathtt{nm}$ particles (no scattering, strong absorption) and high in $150\,\mathtt{nm}$ particles (much stronger scattering than absorption).

It should be emphasized that gold nanoparticles show virtually no luminescence, i.e., the observed light scattering is elastic. This is important to keep in mind when looking at scattering spectra presented in the following chapters. They can only be observed for excitations with *white light*. Plasmons do not emit a broad spectrum in contrast to dyes if excited at a single frequency (Fig. 4.4)!

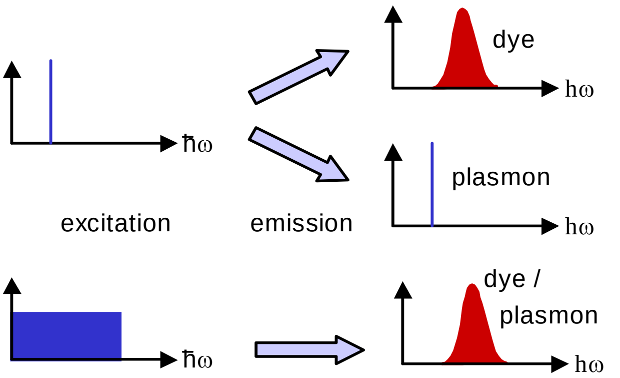

Fig. 4.4: Comparison of luminescence and light scattering for dyes and plasmons. Top: laser excitation leads to broad light emission for dyes but not for plasmons. Bottom: white light excitation leads to a spectrally broad emission of both dye and plasmon.

4.4 Damping mechanisms of particle plasmons

As discussed in Sec. 4.1 , important plasmon properties such as the amplitude of the collective electron oscillation with respect to the driving amplitude, Q, and the width of the particle plasmon resonance, Γ, depends on the amount of damping. In a quasi-particle picture, damping is described as population decay. This decay can be either radiative, i.e. by emission of a photon, or nonradiative (Fig. 4.5).

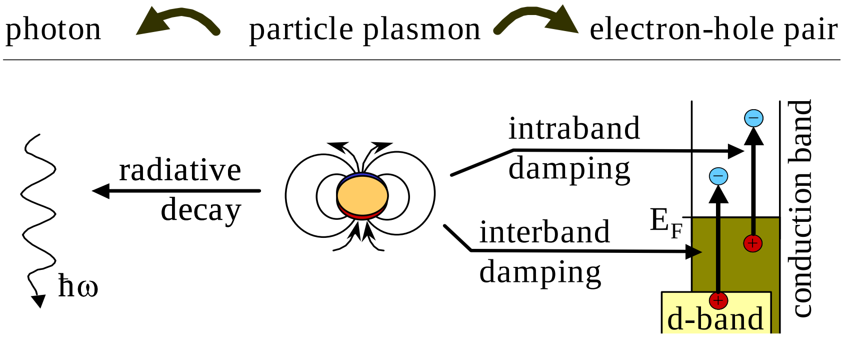

Fig. 4.5: Particle plasmons decay either radiatively (left) or nonradiatively by creation of electron-hole pairs (right). The electron is either excited within the conduction band (intraband) or from the deeper lying d-band into the conduction band (interband).

In order to understand the nonradiative decay of the collective oscillation of the conduction electrons further, it is instructive to treat the electrons independently as in the Drude-Sommerfeld model for optical properties of metals (Sec. 2.2.1). The plasmon is then a superposition of many such independent electron oscillations. Obviously such an approach neglects many-body effects such as a collective scattering with phonons. Nevertheless, the independent electron picture proves to be very useful.

The nonradiative damping is thus due to a dephasing of the oscillation of individual electrons. In terms of the Drude-Sommerfeld model this is described by scattering events with phonons, lattice ions, other conduction or core electrons, the metal surface, impurities, etc.. Because of the Pauli-exclusion principle, the electrons can only be excited into empty states in the conduction band. These excitations can be divided into inter- and intraband excitations by the origin of the electron either in the d-band or the conduction band (Fig. 4.5). Effectively, the movement of the conduction electrons in the particle is a (time dependent) current $\vec{j}(t)$, which feels, of course, the (frequency dependent) resistance of the metal. The frequency dependent conductivity $\sigma(\omega)$ is customarily described by the imaginary part of the dielectric function $\Im(\varepsilon) = \sigma/\varepsilon_0\omega$. The energy dissipated through these nonradiative channels is transferred ultimatively into heat.

These decay mechanism are described by time constants τ_{tot}, τ_{rad}, and τ_{nonrad} (total, radiative and nonradiative decay, respectively). They are connected with the cross-sections discussed in the previous section by:

$$\tau_{\mathrm{rad}} \leftrightarrow Q_{\mathrm{sca}}, \quad \tau_{\mathrm{nonrad}} \leftrightarrow Q_{\mathrm{abs}}, \quad \tau_{\mathrm{tot}} \leftrightarrow Q_{\mathrm{ext}} \tag{4.3}$$

and with the radiative quantum yield η, given by:

$$\eta = \frac{\tau_{\text{rad}}}{\tau_{\text{tot}}} = \left.\frac{Q_{\text{sca}}}{Q_{\text{ext}}}\right|_{\omega=\omega_{\text{res}}} \tag{4.4}$$

4.5 Electrodynamic theories for particle plasmons

A more detailed understanding of the plasmon resonance in metal particles is gained by classical electrodynamics. As mentioned in Sec. 2.1.1 , there are limitations of this electrodynamical treatment. The most severe is that it depends on the knowledge of material parameters, specifically the complex dielectric function ε. Even if those are given, the electrodynamical models assume idealized geometries, namely perfectly sharp boarders and spatially homogeneous materials, and neglect some many-body effects. Many important features observed experimentally for particle plasmons follow from these simple considerations nevertheless.

4.5.1 Quasi-static approximation — Rayleigh Theory

I will first present a simple quasi-static model, attributed to Lord Rayleigh[(iv)], for particle plasmons neglecting effects due to self-induction of electromagnetic fields (retardation). This approach effectively means that a region in space is investigated which is much smaller than the wavelength of light, so the electromagnetic phase is constant throughout the region of interest. For small metal particles with diameters below 40 `nm`, this proves to be a reasonable simplification. It has the advantage that simple electro-statics can be used to calculate the response of a metal sphere to an electric field (Fig. 4.6).

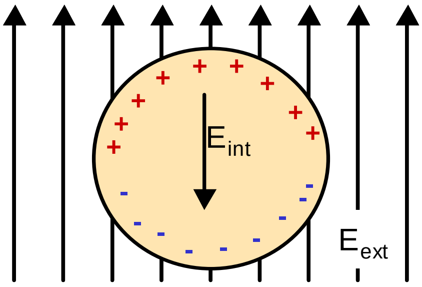

Fig. 4.6: Quasi-static model for particle plasmons.

This simple picture yields for the polarizability α of the metal sphere with dielectric constant relative to the medium $\varepsilon_r = \varepsilon_r' + i\varepsilon_r'' = \varepsilon_{\text{metal}}/\varepsilon_{\text{medium}}$ and volume V (e.g. Nolting, 1993, Sect. 2.4.2.):

$$\alpha = \varepsilon_0 3V \frac{\varepsilon_r - 1}{\varepsilon_r + 2} \quad \text{(Clausius – Mossotti relation)} \tag{4.5}$$

The scattering and absorption cross-section are then (Bohren and Huffman, 1982):

$$C_{\text{sca}} = \tfrac{k^4}{6\pi}\left|(\alpha/\varepsilon_0)\right|^2 = \frac{k^4}{6\pi}(3V)^2\frac{(\varepsilon_r'-1)^2+\varepsilon_r''^2}{(2+\varepsilon_r')^2+\varepsilon_r''^2} \tag{4.6}$$

$$C_{\text{abs}} = k\Im(\alpha/\varepsilon_0) = k3V\frac{3\,\varepsilon_r''}{(2+\varepsilon_r')^2+\varepsilon_r''^2} \tag{4.7}$$

with $k = 2\pi/\lambda$.

[(iv)] *12.11.1842 Langford Grove (Essex), † 30.6.1919 Witham (Essex)‡

It is evident from equation Eqn. 4.6 , that scattering and absorption exhibit the plasmon resonance at approximatively the frequency $E_{\text{res}}/\hbar$, where $\Re(\varepsilon_r) = \varepsilon_r' = -2$. For free particles in vacuum, resonance energies of 3.48 `eV` for silver (near UV) and 2.6 `eV` for gold (blue) are calculated. When embedded in polarizable media, the resonance shifts towards lower energies, i.e. towards the red side of the visible spectrum.

A sum-rule holds for the extinction cross-section:

$$\int_0^\infty C_{\text{ext}}(\lambda) d\lambda = V \cdot C \tag{4.8}$$

with C depending only on DC-material properties (Bohren and Huffman, 1982, Sect. 4.4.6). This means that the total energy taken out of a while light beam by a particle is proportional only to the volume V. It can be either scattered or absorbed. For gold spheres of 100 `nm` diameter, the plasmon resonance accounts for approximatively 90% of the integrated extinction as estimated by numerical integration of Eqn. 4.6 over the plasmon peak. Only the remaining 10% are scattered and absorbed by other processes such as interband absorption.

4.5.2 Scattering by elliptical particles

The electrostatic theory for light scattering by spherical particles with diameters much smaller than the light wavelength λ has a relatively simple extension to ellipsoidal particles. Ellipsoidal particles are characterized by the three semiaxes $a \geq b \geq c$. Of particular interest are those cases where two of these axis have identical length, the *spheroids*. Cigar-shaped spheroids ($a > b = c$) are called *prolate*, pancake-shaped ($a = b > c$) *oblate*, see Fig. 4.7 .

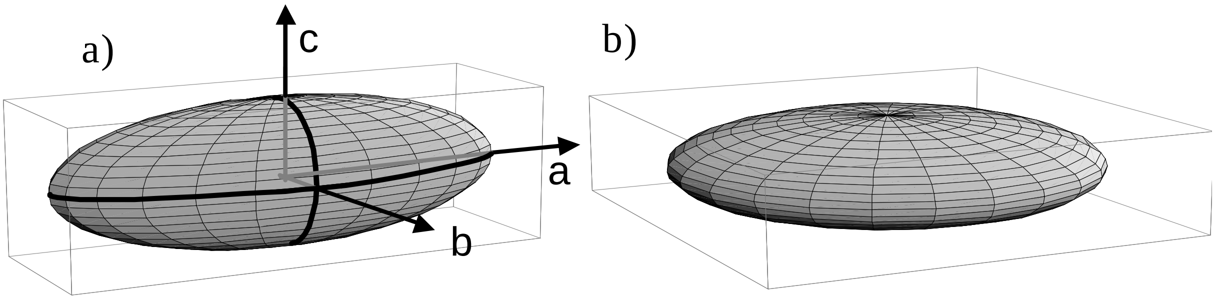

Fig. 4.7: a) prolate (cigar-shaped) sheroid, b) oblate (pancake-shaped) sheroid

The polarizability α_i of such a spheroidal particle along the axis i is given by (Bohren and Huffman, 1982):

$$\alpha_i = \frac{V\varepsilon_0}{L_i} \frac{1 - \varepsilon_r}{(1/L_i - 1) + \varepsilon_r} \tag{4.9}$$

with L_i a geometrical factor related to the shape of the particle.

The sum-rule $L_a + L_b + L_c = 1$ holds, therefore $L_i = \frac{1}{3}$ for spheres (Eqn. 4.9 reduces in this case to Eqn. 4.5). The geometrical factor L_a for a prolate particle along its long axis is given by:

$$L_a = \frac{1 - e^2}{e^2} \left(-1 + \frac{1}{2e} \ln \frac{1 + e}{1 - e} \right), \qquad e^2 = 1 - \frac{b^2}{a^2} \tag{4.10}$$

For practical calculations I found it useful to approximate this relatively complicated expression. The various approximations used in literature (van de Hulst, 1957; Bohren and Huffman, 1982; Shalaev, 2000) are sometimes a factor of 2 off the real value — too crude for comparison with experimental values. I found that for all realistic values of the aspect ratio a/b, L_i is very well approximated by (cf. Fig. 4.8):

$$L_a = \left(1 + \frac{a}{b}\right)^{-1.6} \tag{4.11}$$

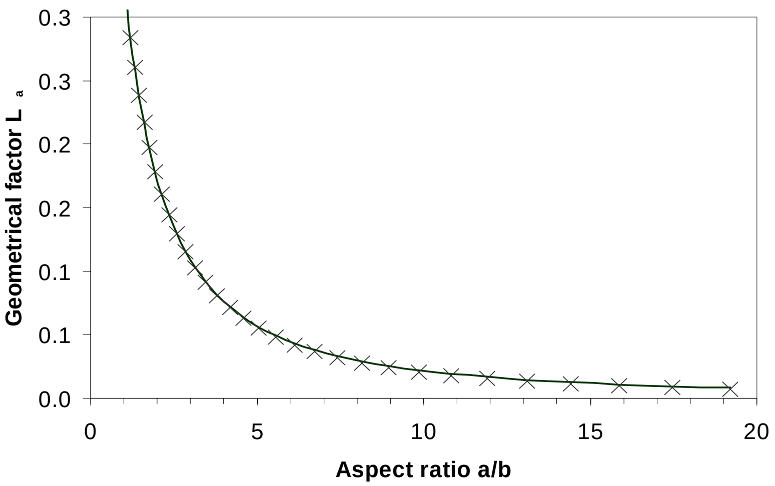

Fig. 4.8: The geometrical factor L_i of the long axis of a prolate spheroid – comparison of the exact formula (crosses) and a simple approximation (line) given by $L_a = (1 + a/b)^{-1.6}$.

4.5.3 Mie theory

The response of a metal sphere to an external electromagnetic field can be calculated by solving Maxwell's equations. For uncharged spherical particles in a homogeneous medium an analytical solution exists. This exact analytical electrodynamical treatment is nowadays attributed to Mie (1908). He was not the first to derive a solution of this problem, but the first to apply it to the problem of light scattering of metal spheres (Logan, 1965). It is therefore customary to call his results *Mie theory.* I will briefly summarize the main results here following the derivation by Bohren and Huffman (1982).

The spherical symmetry suggests the use of a multipole extension of the fields, here numbered by n. The Rayleigh-type plasmon resonance, discussed in the previous sections, corresponds to the dipole mode $n = 1$. In the Mie theory, the scattering and extinction efficiencies are calculated by:

$$Q_{\mathrm{sca}}^{(n)} = \frac{2}{x^2}(2n+1)(|a_n|^2 + |b_n|^2) \tag{4.12}$$

$$Q_{\mathrm{ext}}^{(n)} = \frac{2}{x^2}(2n+1)\mathrm{Re}(a_n + b_n) \tag{4.13}$$

with $x = k\,r = \hbar\omega\, r\, N_{\mathrm{medium}}/(\hbar c)$, k: wave vector, r: particle radius, N: refractive index, and a_n, b_n the Mie coefficients, which are calculated by:

$$a_n = \frac{m\psi_n(m\,x)\psi_n'(x) - \psi_n(x)\psi_n'(m\,x)}{m\psi_n(m\,x)\xi_n'(x) - \xi_n(x)\psi_n'(m\,x)} \tag{4.14}$$

$$b_n = \frac{\psi_n(m\,x)\psi_n'(x) - m\psi_n(x)\psi_n'(m\,x)}{\psi_n(m\,x)\xi_n'(x) - m\xi_n(x)\psi_n'(m\,x)} \tag{4.15}$$

with $m = \sqrt{\varepsilon_r} = N_{\mathrm{particle}}/N_{\mathrm{medium}}$ and the Riccati-Bessel functions ψ_n and ξ_n (Bohren and Huffman, 1982).

These equations allow the calculation of scattering cross-sections in a relatively straight forward manner using algebraic programs such MATHEMATICA™. An implementation is shown in Fig. 4.9 .

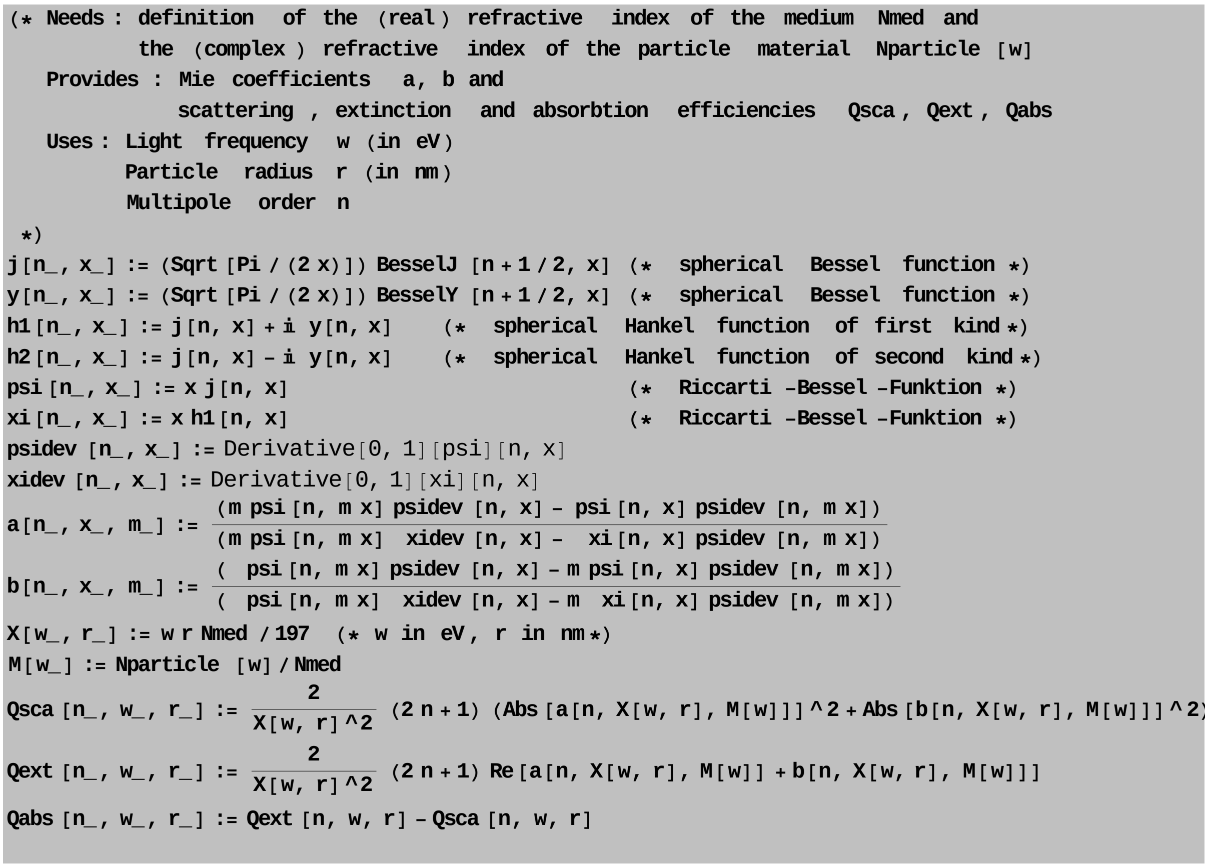

```
(* Needs : definition  of the  (real ) refractive  index  of the  medium  Nmed  and
         the  (complex ) refractive  index  of the  particle  material  Nparticle [w]
   Provides : Mie  coefficients   a, b and
              scattering , extinction  and absorbtion  efficiencies  Qsca , Qext , Qabs
   Uses : Light  frequency  w (in eV)
          Particle  radius  r (in nm)
          Multipole  order  n
 *)
j[n_, x_] := (Sqrt [Pi / (2 x)]) BesselJ [n + 1 / 2, x]  (*  spherical  Bessel  function *)
y[n_, x_] := (Sqrt [Pi / (2 x)]) BesselY [n + 1 / 2, x]  (*  spherical  Bessel  function *)
h1[n_, x_] := j[n, x] + i y[n, x]    (*  spherical  Hankel  function  of first  kind *)
h2[n_, x_] := j[n, x] - i y[n, x]    (*  spherical  Hankel  function  of second  kind *)
psi [n_, x_] := x j[n, x]                                (*  Riccarti -Bessel -Funktion *)
xi [n_, x_] := x h1[n, x]                                (*  Riccarti -Bessel -Funktion *)
psidev [n_, x_] := Derivative[0, 1][psi][n, x]
xidev [n_, x_] := Derivative[0, 1][xi][n, x]
                  (m psi [n, m x] psidev [n, x] - psi [n, x] psidev [n, m x])
a[n_, x_, m_] := ─────────────────────────────────────────────────────────────
                  (m psi [n, m x]  xidev [n, x] -  xi [n, x] psidev [n, m x])
                  (  psi [n, m x] psidev [n, x] - m psi [n, x] psidev [n, m x])
b[n_, x_, m_] := ───────────────────────────────────────────────────────────────
                  (  psi [n, m x]  xidev [n, x] - m  xi [n, x] psidev [n, m x])
X[w_, r_] := w r Nmed / 197  (* w in eV, r in nm*)
M[w_] := Nparticle  [w] / Nmed
                          2
Qsca [n_, w_, r_] := ─────────── (2 n + 1) (Abs [a[n, X[w, r], M[w]]] ^2 + Abs [b[n, X[w, r], M[w]]] ^2)
                      X[w, r] ^2
                          2
Qext [n_, w_, r_] := ─────────── (2 n + 1) Re [a[n, X[w, r], M[w]] + b[n, X[w, r], M[w]]]
                      X[w, r] ^2
Qabs [n_, w_, r_] := Qext [n, w, r] - Qsca [n, w, r]
```

Fig. 4.9: MATHEMATICA$^{\text{tm}}$ script to calculate Mie coefficients. The dielectric function of the particle eAu[w] and the refractive index of the medium Nmed must be priorly defined.

4.5.4 Some results of electrodynamic calculations

Tabulated bulk dielectric functions (e.g. Johnson and Christy, 1972) and the models discussed above allow to calculate scattering, absorption, and extinction cross-sections. I present here results of such calculations for a number of different particle geometries to show some of the involved phenomena.

Fig. 4.10 shows an example of the results of such an electrodynamic calculation using the Mie theory. In this case, the cross-sections are calculated for a 60 nm gold nanosphere embedded in a medium with refractive index $n = 1.5$. At the high energy side, interband contributions lead to an offset, especially for the absorption cross-section. To systematically study the influence of size, shape and embedding medium on the plasmon resonance, I extract resonance position E_{res} and the full linewidth at half maximum (FWHM) Γ from the calculated scattering cross-section(v).

First, the influence of size and shape on the particle plasmons resonance energy and linewidth is studied for gold nanoparticles embedded in a medium with refractive index $n = 1.5$. Fig. 4.11 a shows the results for gold nanospheres with increasing diameter. A

(v) Scattering cross-sections are chosen in order to allow for comparison with scattering experiments presented later in this work.

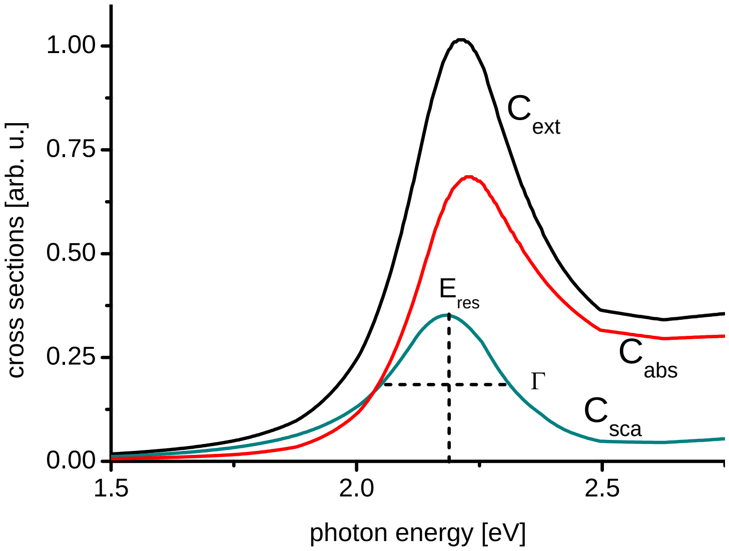

Fig. 4.10: Example for extinction, absorption and scattering cross-sections (C_{ext}, C_{abs}, C_{sca}, respectively) of a 60 `nm` gold sphere embedded in a medium with refractive index $n = 1.5$. The cross sections are calculated with the Mie theory using the tabulated values for the dielectric function for gold (Johnson and Christy, 1972). Resonance energy E_{res} and full width at half maximum (FWHM) Γ of the scattering cross-section are indicated.

red-shift is observed for increasing size, and simultaneously a broadening of the resonance. The broadening is due to increasing radiation damping for larger nanospheres. The red-shift is partly due to increased damping and to retardation effects (Kreibig and Vollmer, 1995).

Since red-shift of the resonance position increases monotonously, the resonance position can be used to calculate “backwards” the particles diameter. By fitting the values presented in Fig. 4.11 a, one obtains the simple relation ($20 < d/\,\mathtt{nm} < 160$):

$$d\,/\,\mathtt{nm} = 215\sqrt{2.262 - E_{\text{res}}/\,\mathtt{eV}} \tag{4.16}$$

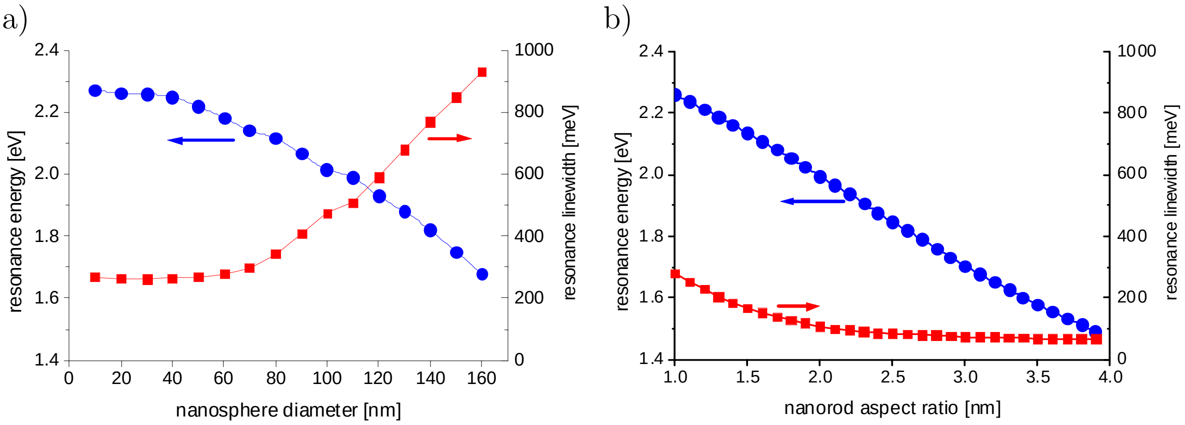

Fig. 4.11: a) Influence of size and, b) shape, on the resonance position and linewidth of the scattering cross-section for gold nanoparticles. a) spherical gold particle spectra calculated by Mie theory. b) gold nanorods calculated by the Rayleigh theory for ellipsoidal particles.

As mentioned above, Mie calculations for particle shapes other than spheres are not readily performed. For very small particles, however, the Rayleigh approximation may be used. I present the results for such a Rayleigh calculation for gold nanorods by varying their aspect ratio in Fig. 4.11 b. (I approximate the rods by cigar shaped spheroids, which is reasonable considering their small size). Also, a red-shift of the resonance is observed with increasing aspect ratio. In contrast to the nanospheres shown in Fig. 4.11 a, the linewidth of the nanorods decreases. Since radiative effects are neglected in the Rayleigh approximation, this decrease in linewidth reflects the decrease of the damping described by the imaginary part of the dielectric function of gold for lower energies, cf. Fig. 2.1 .

Similar to the case of gold nanosphere, the values presented here can be used to calculate "backwards" the aspect ratio for a given resonance energy E_{res} by fitting the values in Fig. 4.11 b. Since the Rayleigh calculation assumes particles with dimensions much smaller than the wavelength of light, the resulting equation may only be used for such nanorods. It is given by $(1 < a/b < 4)$:

$$a/b = 1 + 3.6\ (2.25 - E_{\mathrm{res}}\,/\,\mathtt{eV}) \tag{4.17}$$

Not only particle parameters such as size and shape influence the plasmon resonance, but also the refractive index of the surrounding medium. I show here the effect of an increasing refractive index on the resonance position and linewidth of a 20 nm gold nanosphere. The results, calculated with the Mie theory, are shown in Fig. 4.12 a. Increasing refractive index of the medium leads to a red-shift of the resonance and a narrowing of its linewidth. The red-shift is due to the shielding of the surface charges by the polarization of the embedding medium. The linewidth narrowing is due to a smaller damping for higher resonance energies due to smaller values of the dielectric function for gold with decreasing energy (Fig. 2.1).

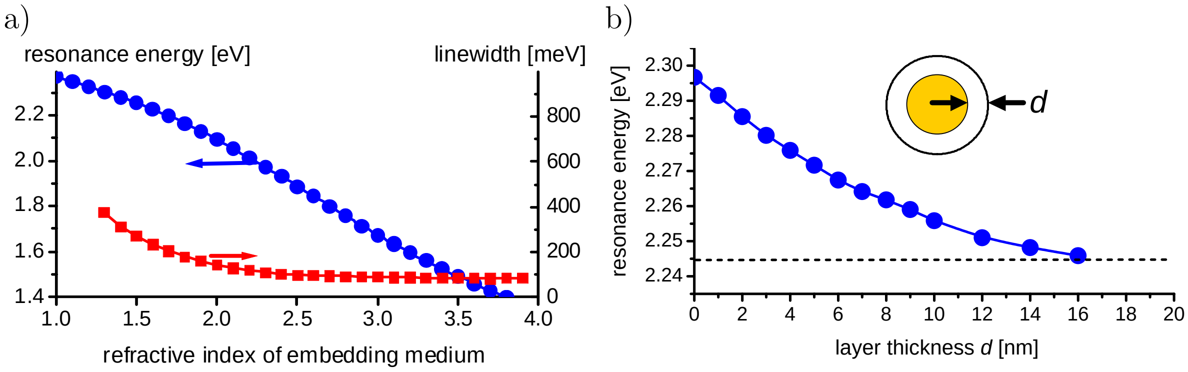

Fig. 4.12: a) Influence of the refractive index of the embedding medium on the resonance position and linewidth of the particle plasmon resonance of a 20 nm gold nanosphere. Calculated using the Mie theory. b) Resonance energy for a 40 nm gold nanosphere embedded in water (n = 1.33) with increasing thickness d of a layer with refractive index n = 1.5. Dotted line: resonance energy for an infinite layer thickness.

It is important in context of the experiments described in Chap. 9 that only a small layer of the medium around the particle substantially influences the plasmon resonance. This is demonstrated in Fig. 4.12 b. I show here the resonance position of a 40 nm gold nanosphere embedded in water ($n = 1.33$) with an increasingly thick layer of a material with refractive index of $n = 1.5$ around it.

4.5.5 Limits of the electrodynamic theory

It might seem that with the powerful theoretical tools discussed in the previous sections, experiments should be able to reproduce those results. This is, however, not the whole truth. It is not known a priori if the bulk values for the material properties entering the calculations are indeed valid for particles with nanometer dimensions (Serra and Rubio, 1997; Shahbazyan *et al.*, 1998). Possible effects could be quantum mechanical confinement, surface melting, surface adsorbates, etc.

Also it is unclear whether the assumptions in the theoretical models, for example sharp boundaries, no many-body effects, etc., are reasonable. So the applicability and limits of the electrodynamical and electrostatic theory have to be experimentally investigated.

Electrodynamical theory alone cannot give insight into the microscopic processes leading to the experimentally observed or calculated particle spectra. Only in conjunction with the underlying explanation of the optical material constants by solid state theory are the "real" physical processes revealed.

4.6 Open questions

Central to the understanding of particle plasmons is of course the question about the applicability and limits of the electrodynamical and electrostatic theory. The experimental challenge is two-fold: first, reliable techniques to measure particle properties (which can be compared to theory) have to be found. Second, metal particles have to be produced with the desired shape, purity and crystal structure. The latter is a material science problem. Depending on the point of view of the investigator, the experimental results can therefore either be interpreted fundamentally by comparing theory and experiment — or in a material science context to determining the quality and properties of real samples produced by a certain method.

The most important open question regarding fundamental particle plasmon properties is the amount and origin of their damping. Many conflicting results have been reported in literature, especially on the role of surface scattering and pure dephasing. There is disagreement about the damping mechanism as well as their amount in real samples. Intense research efforts have been conducted to determine the exact amount of damping for various particles (e.g. Heilweil and Hochstrasser, 1985; Kreibig and Vollmer, 1995; Puech *et al.*, 1995; Klar *et al.*, 1998; Lamprecht *et al.*, 1999; Link and El-Sayed, 1999b, 2000; Stietz *et al.*, 2000; Adam *et al.*, 2000; Liau *et al.*, 2001). Due to experimental problems and a limited control over sample geometry, a satisfying answer regarding the amount, origin and dependence on particle parameters of the plasmon dephasing time is missing. The reported lifetimes vary between $T_1 = 2\text{–}11\,\mathtt{fs}$ (for gold and silver). One reason is the underestimation of inhomogeneous broadening effects, which contributes significantly to many experimental observations and was not duly taken into account for some time (Vartanyan *et al.*, 1999). A way to circumvent this problem is to study individual particles. So far only very few reports of investigations on individual particles exist. A study in time-domain on large silver clusters of unknown size and shape was recently reported (Liau *et al.*, 2001). In the spectral domain there are very few reports of single nanoparticle spectra (Silva, 1994; Michaels *et al.*, 2000; Klar *et al.*, 1998). Only the latter study, however, actually determines the homogeneous linewidth and dephasing time from the measured data. The values of $T_2 = 8\,\mathtt{fs}$ reported for a special sample (spherical gold particles with $40\,\mathtt{nm}$ diameter in a titanium dioxide matrix) does not sufficiently answer the general question about dephasing times in other types of nanoparticle samples.

The results of experiments described in Chap. 8 of this work are the first reliable and systematic study of these dephasing times and solve the question about the amount of damping and its dependence on size and shape for the classes of particles studied.

Another open question is: how can particle plasmons be employed in real devices? Among the potential applications I discussed in more detail in Sec. 4.2 are guiding light on a nanometer scale and employing it as a *local* sensor. I will show in Chap. 9 how such a nanosensor application can be realized. A new type of application, namely employing particle plasmon to electrically control light scattering out of a waveguide, is demonstrated in Chap. 10 . It also remains a challenge to apply particle plasmons to enhance nonlinear effects, to understand plasmon modes of more complicated metal structures and to understand the interaction of plasmon resonances with molecular resonances or other photonic devices such as lasers or photonic crystals.

5. EXPERIMENTAL METHODS

In this chapter I will introduce the main experimental methods used in this work. In particular, these are near- and far-field optical microscopy in various configurations. At the end of this chapter I will compare the applicability of near- and far-field techniques for single nanoparticle spectroscopy. I find far-field techniques to be highly advantageous over near-field microscopy for this application.

5.1 Near-field microscopy

Resolution in conventional far-field microscopy is limited by the well-known diffraction limit to approximately the wavelength of light. Scanning near-field microscopy (SNOM) circumvents this limit by scanning a local source of radiation across the sample surface. The resolution is then mainly limited by the source dimension and the sample to source distance, both of which have to be much smaller than the wavelength of visible light to improve resolution as compared to conventional light microscopy. The most commonly employed realization of this concept is to use light leaking out of a small aperture at the tip of a metal coated sharpened glass fiber as the local light source. This fiber tip is then brought very close to the sample surface. The tip to sample distance is usually kept constant by a feedback mechanism, which allows simultaneous collection of topography and optical signals. Of course, many variations of this idea exist, see for example Paesler and Moyer (1996).

The scanning near-field optical microscope used for the experiments in this work has been described in detail before (Klar, 1997; Grosse, 1998; Perner, 1999) and is shown in Fig. 5.1 . The SNOM is used in illumination mode, i.e. laser light is incident on the sample through the aperture of the SNOM tip, which is scanned across the surface. A tunable c.w. dye laser (wavelength range 520-570nm), a helium-neon laser (633nm) and a tunable continuous wave (c.w.) titanium:sapphire laser (750-1000nm) are used as light sources. The fiber tips are produced by controlled local melting of a single mode glass fiber and subsequent pulling. By choosing the right parameters, a fine tip is produced at the end of the single mode fiber. The resulting fiber is metal coated by evaporation at an angle from the back, which leaves a small opening at the apex of the tip. Aluminum with a thin chromium adhesion layer is used for this coating. The sample-to-tip distance is kept constant at $\approx 7nm$ via shear force feedback (Karrai and Grober, 1995). The intensity of the light radiated from the rear side of the sample is measured with a PIN photo diode fixed to the glass substrate.

The near-field optical setup described so far was developed by Stephan Grosse for time resolved low temperature measurements. For room temperature spectroscopy, some adjustments and improvements were necessary. Besides considerably increasing the stability

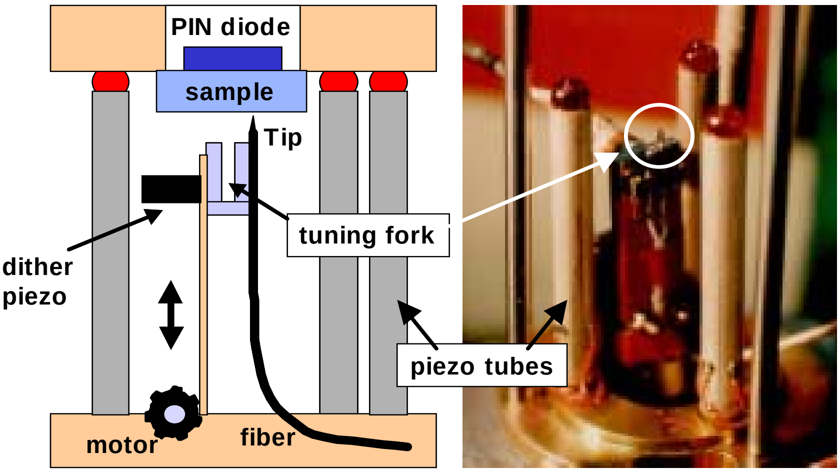

Fig. 5.1: The SNOM setup used in this work is shown schematically on the left. The fiber tip is glued to a tuning fork which is externally excited by a dither piezo for shear-force feedback. The tip to sample distance is first coarse regulated with a step-motor and then fine regulated by the piezo tubes which are also responsible for the scanning. Light emmitted by the SNOM tip and transmitted through the sample is collected by a PIN photo-diode behind the sample. Right: photograph of the real setup without the sample holder.

of the whole setup, the main improvement realized during the studies described in this work is the use of an X-shaped fiber coupler. It allows the coupling of two lasers into the fiber simultaneously and gives a reference output to monitor the efficiency of the coupling process (Fig. 5.2). The use of two lasers is particularly useful if working in the (invisible) near infrared. The visible light from the helium-neon-laser can then be used to adjust and check the setup. For the measurements, one of the laser beams is blocked. Carefully removing or setting a beam blocker can be done with the tip engaged (i.e., with the feedback loop keeping it at 7 nm above the surface), which enables measurements at the same sample position at both laser frequencies.

Besides the practical advantages mentioned above, the simultaneous use of two lasers with different wavelengths gives interesting and beautiful color effects — an illustration of this is shown in Fig. 5.3.

Scanning near-field microscopy as described above has the advantages of simultaneous collection of topographic and optical information in conjunction with high resolution that is beyond the diffraction limit. The disadvantages are the enormous experimental effort necessary for a single experiment, the low signals collected and the difficulty in interpretation of the results due possible topographic artifacts (Paesler and Moyer, 1996). If the experimental circumstances allow the placement of the samples far enough from each other to be distinguished in the far-field, the advantages of near-field microscopy vanish. Conventional far-field microscopy should be used in this case. Some far-field methods to measure *scattering* spectra will be described below.

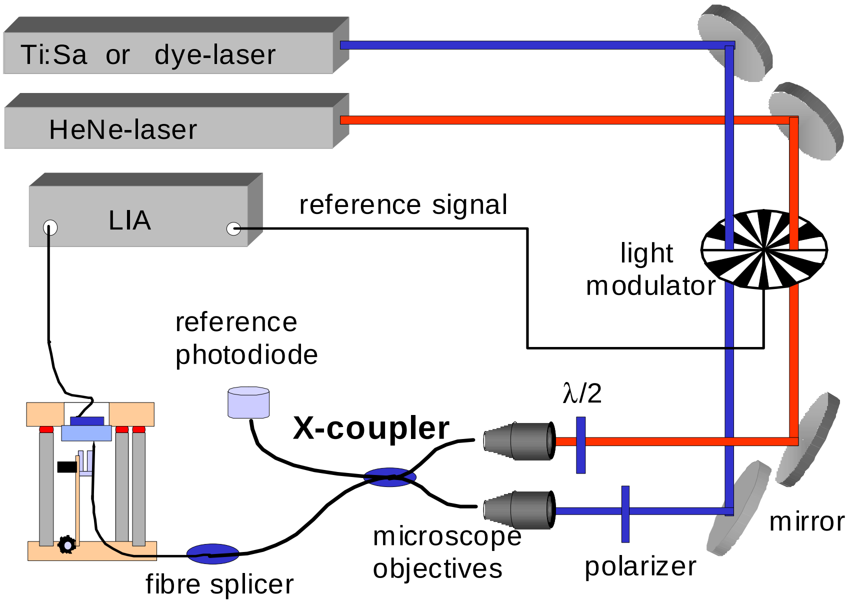
Ti:Sa or dye-laser
HeNe-laser
LIA
reference signal
light
modulator
reference
photodiode
λ/2
X-coupler
microscope
objectives
polarizer
mirror
fibre splicer

Fig. 5.2: Experimental setup used to couple two lasers into the SNOM fiber. LIA: LockIn Amplifier. Light from two lasers is modulated and coupled into a glass fiber. Polarizer and half-wave-plates are used to control the polarization direction. One output of the X-type fiber coupler is used as reference.

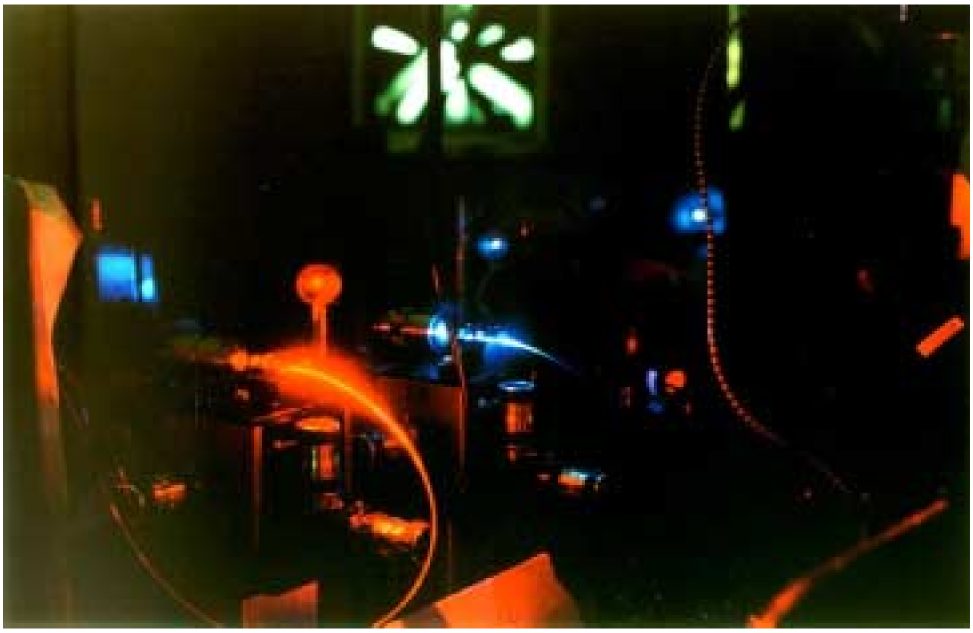

Fig. 5.3: Red and blue lasers coupled simultaneously into the SNOM fiber.

5.2 Microscopic scattering spectroscopy in the far-field

The resolution of conventional far-field microscopy is limited by diffraction to approximately the wavelength of light. Achieving this limit usually poses no problem. Also, the signal intensity usually does not limit the observation of even single molecules due to the high power of modern light sources such as halogen lamps or lasers in combination with very sensitive detection devices such as charge coupled device (CCD) cameras or photomultipliers. The main challenge is therefore the signal to background contrast. There are, for example, many methods to enhance the low contrast usually observed in mostly transparent biological material (e.g. phase contrast, differential interference contrast (DIC), polarization contrast, etc.). In order to investigate very small objects (such as single molecules) some mechanism has to block the exciting light completely. In fluorescence microscopy this is achieved by blocking the exciting light with a high quality interference filter. In Raman spectroscopy a spectrometer is usually used for the same purpose. Obviously these methods of spectral filtering are limited to objects that emit light at a frequency different from the exciting light. This is not the case for metal nanostructures.

Most of the previously published work on metal nanoparticles has focused on their light *absorption* or extinction. There is no simple way to measure single particle absorption for particles much smaller than the wavelength of light as their extinction cross section is roughly given by their geometrical size. A diffraction limited beam of light will therefore only lose a very small fraction of its intensity. This is the reason why previous spectroscopic studies of metal nanoparticles have been performed on large ensembles of particles.

There is, however, a way to circumvent this problems. Instead of trying to measure the particle absorption, the light *scattered* by the particle can be investigated. Since scattering is a change of propagation direction, it allows the suppression of the excitation light *spatially*. Even though this relatively simple idea has been used for a long time in many research areas, it was unknown for the spectroscopic study of individual metal nanoparticles. The reason is probably that very small spherical particles (smaller than 10 nm), which have traditionally received most of the attention, are poor light scatterers and hence are not suited for this method. The great increase of contrast over conventional microscopy in transmission or reflection (the so called bright-field methods) is shown in Fig. 5.4 .

There are a number of different approaches to achieve scattering contrast, three of which are used for the studies in this work and will be described below.

5.2.1 Total internal reflection microscopy

The most simple way to suppress the excitation light is to place the particles in an evanescent, i.e. non-propagating light field. Naturally, only light converted into propagating modes can reach the detector. This approach is very similar to the situation in a near-field microscope, where a large fraction of the light field at the SNOM tip is of an evanescent nature and has to be converted into propagating modes by the sample in order to reach the detector. In the far-field setup used here, this evanescent field is produced by

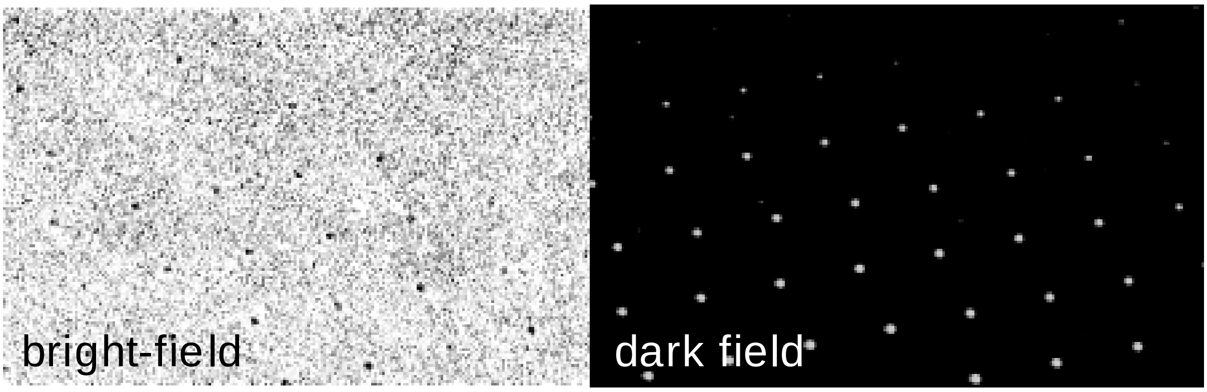

Fig. 5.4: Sample of small gold islands in a conventional microscope (left) and in a scattering microscope (right). Particles separated by 10 μm

total internal reflection of the excitation light at the surface of the substrate. The setup is schematically shown in Fig. 5.5 .

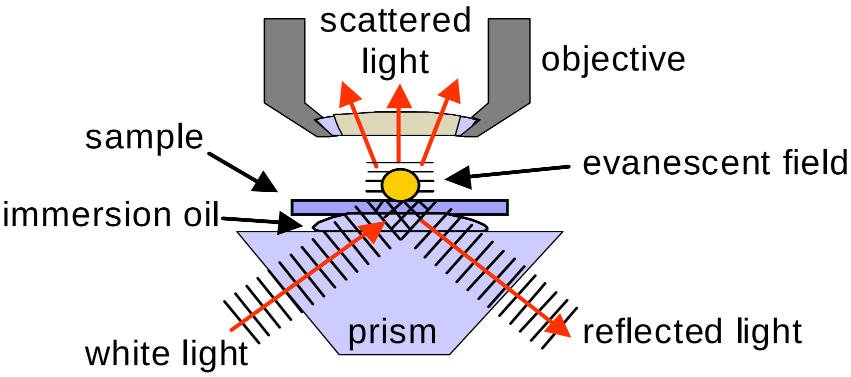

Fig. 5.5: Total internal reflection microscope (TIRM) setup.

The total internal reflection at the surface of the sample is achieved by directing the light through a prism, which has been attached to the sample with an index matching fluid. Particles placed in the evanescent field above the substrate surface scatter light out of this field. *Only* this scattered light is collected by a conventional microscope. Visual inspection through the eyepieces allows fast and reliable localization of the structures of interest on the sample. To gain flexibility, the light is brought to the setup via a multimode glass fiber.

The advantage of this setup — besides its simplicity — is the control of the angle of incidence and polarization state of the excitation light field. Another advantage is the exclusive use of standard optical components (prism, multimode-fiber, lenses) in the excitation light beam path, which can be easily adapted to sustain strong laser pulses. It is therefore ideally suited for time-resolved or nonlinear experiments.

Disadvantages are the asymmetry of the excitation from the side of the setup and the need for a large change in the index of refraction at the substrate surface to allow for total internal reflection. These constrains inhibit polarization dependent studies of particles in a homogeneous dielectric environment.

However, total internal reflection is not the only way to suppress the excitation light beam. By carefully designing the excitation and collection geometries, this can be achieved without any reflection in a rotationally symmetric way. The general term describing such setups is *dark-field* microscopy, because the observer sees scattering centers on the sample as bright spots on a dark background. The contrast achieved crucially depends on the efficient suppression of the excitation light. Many conventional microscopes allow for a so-called 'dark-field mode' by placing ring-shaped apertures in the light path. The contrast achieved in this way is very poor, though, and does not truly justifying the name.

In the design of microscopes one distinguishes between transmission and reflection geometries depending on whether the light has to pass through the sample or not. Obviously the samples have to be transparent for transmission microscopy. In this study, dark-field microscope setups of both types are used and will be described in the following.

5.2.2 Dark-field microscopy in reflection

A dark-field microscope in reflection geometry requires specially designed microscope objectives, which have a light path outside of the actual objective as shown in Fig. 5.6 . The light is then reflected from the side to the center of the field of view by a ring-shaped mirror at the end of the objective. Part of the excitation light is reflected at the sample surface, the other part is transmitted through or absorbed in the sample.

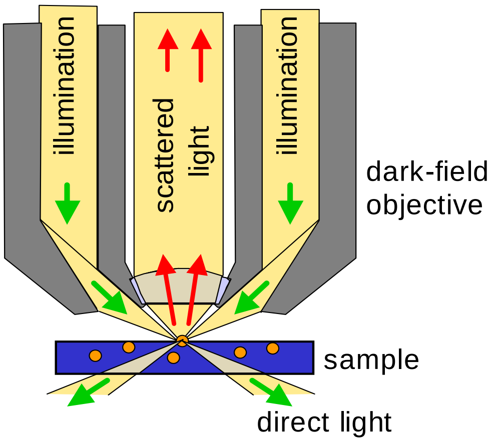

Fig. 5.6: Dark-field objective for reflection type microscopy. The excitation light is directed to the sample surface along the side of the real objective and reflected to the center by a ring-shaped mirror at the end of the objective.

This type of microscope is used primarily to inspect non-transparent surfaces of minerals and structured semi-conductors. Besides the ability to inspect non-transparent substrates, the big advantage is that it does not require any immersion oil on or below the sample. A disadvantage is the inherently low collection efficiency of the objectives. A practical limitation is the fact that dark-field microscope objectives are relatively rare. For example, there are (to the best of my knowledge) no dark-field objectives available which are corrected for water immersion. Also, the dark-field objectives require a special microscope setup to inject the light into the objective.

5.2.3 Dark-field microscopy in transmission

Dark-field microscopy with a transmission geometry operates with conventional microscope objectives. The only change to a conventional microscope is the dark-field condensor, which illuminates the sample from behind as shown in Fig. 5.2.3 . The illumination and detection angle have to be chosen carefully in order to ensure that no direct light enters the objective. In microscopy, angles are usually expressed as numerical apertures N.A. defined by:

$$N.A. = n \sin(\alpha) \tag{5.1}$$

with α: angle of incidence measured with respect to the optical axis, n: refractive index of the medium in which the light propagates. The condensor N.A. has to be larger than the objective N.A. The dark-field aperture has to block exactly the light which would propagate directly into the objective, i.e. has to block the objective N.A. The condensor used here has an illumination N.A. of 1.4 to 1.0, which means that objectives with N.A.s up to 1.0 may be used. This poses no limitations for air objectives, but restricts the use of immersion objectives.

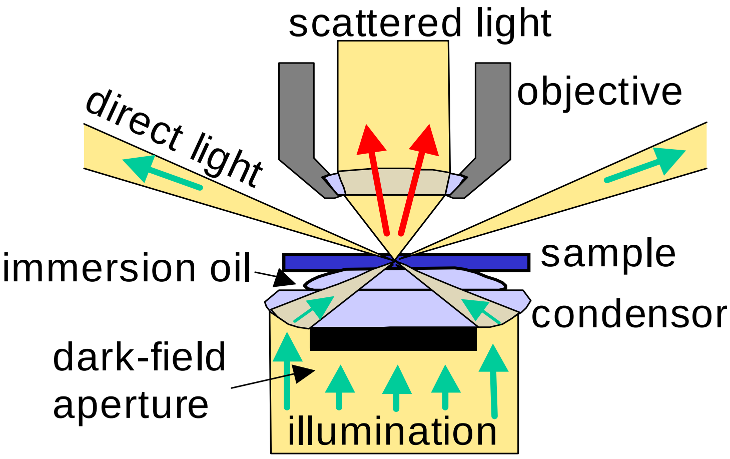

Fig. 5.7: Dark-field setup for transmission-type microscopy. The sample is illuminated from the back by a high aperture condensor with a dark-field aperture blocking the central light beam.

5.2.4 Recording of scattering spectra

In the previous sections, three types of setups have been shown to achieve dark-field or scattering contrast. The remaining challenge for scattering *spectroscopy* is the recording of spectra of small sample regions. An imaging spectrograph (SpectraPro 300i, Acton Reasearch) is used for this purpose. In order to avoid chromatic aberrations, no additional optics should be placed between the microscope and the spectrometer, which means that the spectrometer has to be placed exactly at the focal plane behind the exit port of the microscope. The actual configuration is shown in Fig. 5.8 .

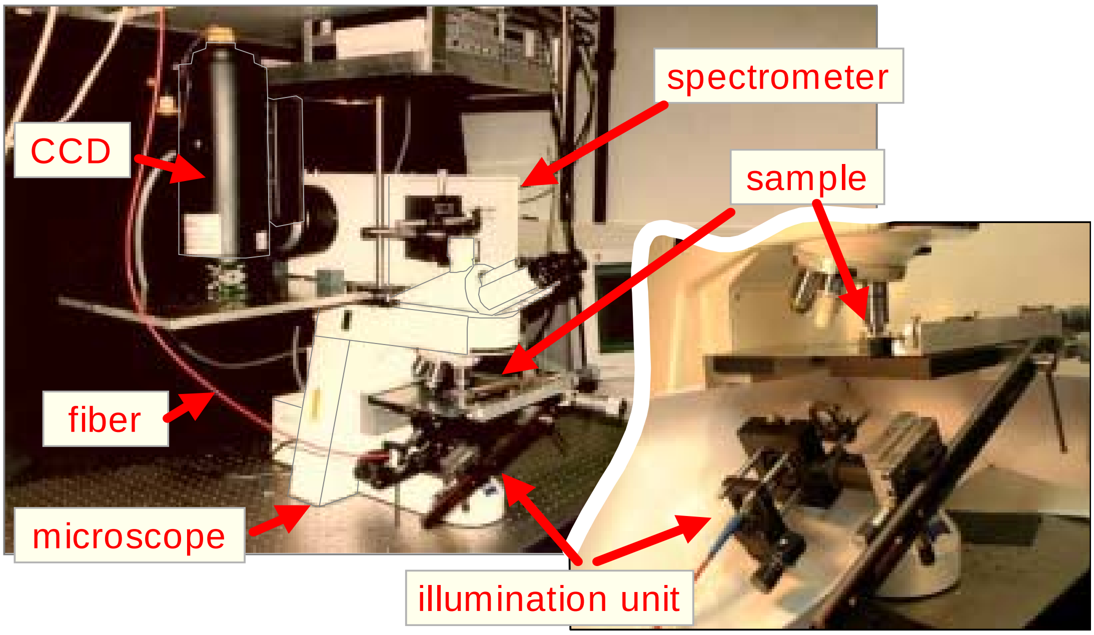

Fig. 5.8: Photograph of the total internal reflection (TIR) setup. The scattered light collected by the conventional microscope is focused on the entrance of a spectrometer, which is read out by a nitrogen cooled CCD camera.

Hence, the central portion of the field of view is imaged on the entrance slit of the spectrograph. The exit port of this spectrograph is coupled to a liquid nitrogen cooled, back illuminated charged coupled device (CCD) array (Princeton Instruments). The spectrograph can also be operated in an imaging mode using a mirror in place of the grating in order to identify and select the particles of interest (Fig. 5.9).

If the mirror is replaced by a grating, the light entering the entrance slit is horizontally dispersed according to its frequency. The software (WinSpec32) allows the integration of the light collected from an individual particle in a so-called region of interest (ROI) to record the single particle spectrum. Up to seven spectra can be recorded at the same time by this procedure by vertical stacking of ROIs. In practice, this is mainly used to record a background spectrum together with the particle spectrum.

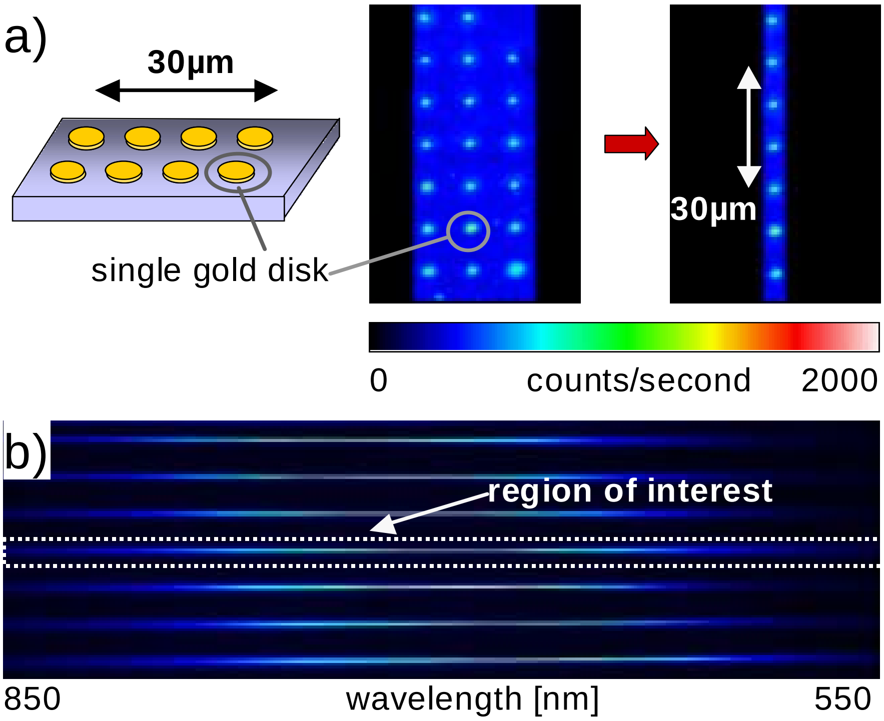
a)
30µm
single gold disk
30µm
0
counts/second
2000
b)
region of interest
850
wavelength [nm]
550

Fig. 5.9: a) The imaging mode of the spectrometer allows the identification of particles of interest. The entrance slit is then closed until only those particles, which are to be spectrally investigated, are visible. b) Switching to spectroscopy mode by replacing the mirror with a grating, the light from the selected particles is spectrally dispersed in the horizontal direction. The spectrum is obtained by software-integration of the light from a region of interest (ROI, dotted lines).

5.3 Determination of dephasing times from single particle scattering spectra

A study by Thomas Klar in the Photonics and Optoelectronics Group was the first, in which a particle plasmon dephasing time was determined from a measured homogeneous linewidth. A sample of gold nanospheres embedded in a titanium dioxide matrix was examined by a near-field microscope. When a particle was below the SNOM tip and the light frequency used corresponded to the plasmon resonance frequency, a strongly enhanced light transmission was observed (Fig. 5.10 a). The reason was the scattering of light intensity out of the evanescent field below the SNOM tip by the metal particle. By changing the excitation light frequency, near-field scattering spectra could be recorded.

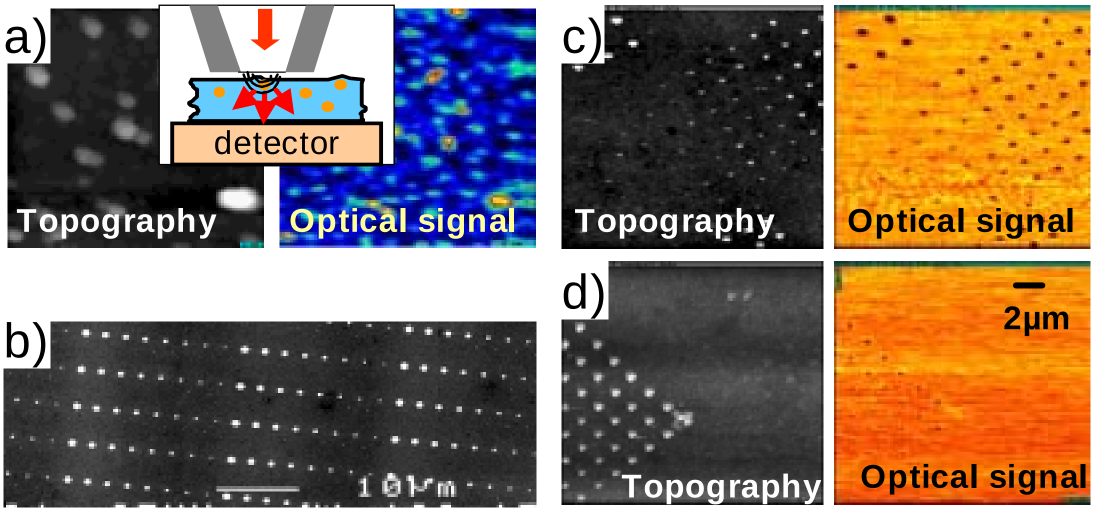

Fig. 5.10: a) SNOM images of the same sample studied in (Klar *et al.*, 1998). Clearly, particles found to be sticking out of the surface (left) give high signal in transmission (right). b) Scanning electron microscopy (SEM) image of a sample of gold nanodisks with different diameters. c) and d) SNOM image of the sample shown in b) for two different wavelength of the exciting light (633 nm and 550 nm, respectively). Particles observed in the topographic image (left) are *dark* in transmission (right).

From theoretical considerations, it was clear that the plasmon dephasing time and resonance position should depend on a number of different parameters, for example the particle size. The initial aim of the present study was to determine the exact influence of such parameters. First experiments on a sample provided by Gerburg Schider (University of Graz) with particles of different sizes (Fig. 5.10 b) showed no enhanced transmission regardless of excitation wavelength (Fig. 5.10 c,d), which is now known to be due to the poor radiative quantum efficiency(i) of the particles in this sample. The overall light emission by a SNOM tip is low even for scans over perfectly transparent substrates due to its mainly evanescent nature. Thus, the small absorption of metal nanoparticles only weakly changes this already weak signal. It is therefore not well suited for single particle spectroscopy.

(i) ratio of scattered to absorbed light energy

This fundamental problem together with the enormous experimental effort required for single particle spectroscopy using SNOM, led to the development of the far-field techniques presented in this work. The great progress in signal to noise ratio during the development of these techniques becomes clear by comparing the spectra in Fig. 5.11 , which shows examples of the first and latest scattering spectra of single particles.

Another great advantage of the techniques presented here is the enormous reduction in measuring time from a couple of hours per spectrum in the case of the SNOM measurements to between a few tens of minutes to a few seconds in the latest setup Fig. 5.11 . These numbers do not include the sample and setup preparation time, which is on the order of days to weeks for SNOM measurements and a matter of one or two hours for the far-field measurements! It is immediately obvious that the range of experiments presented in this work would have been impossible with the original technique used by Klar *et al.* (1998). The enormous increase in measurement accuracy and speed allows a detailed study of the dephasing process in nanoparticles, presented in Chap. 8 . In addition, the flexibility gained by switching to far-field microscopy allows the use of particle plasmon resonances for a number of applications as described in Chap. 9 and Chap. 10 .

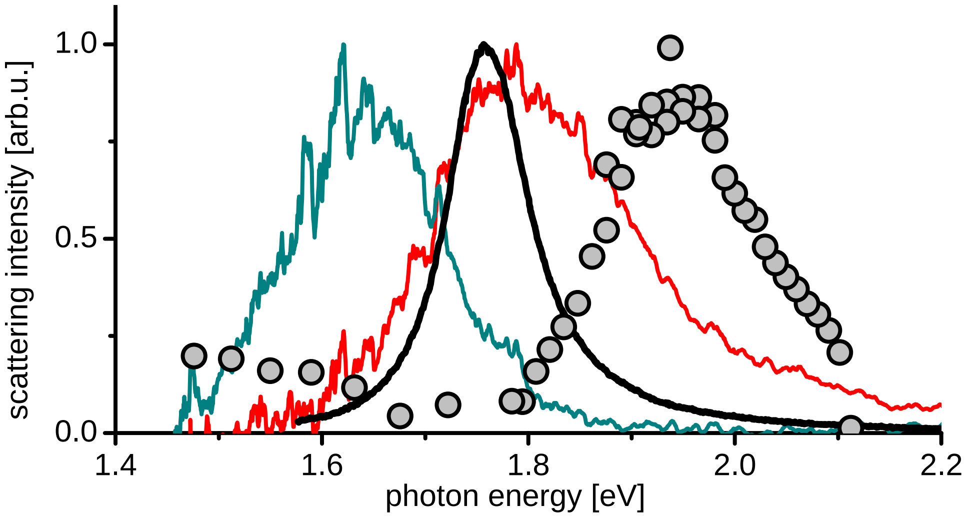

Fig. 5.11: Examples of far-field single particle spectra demonstrating the huge progress in measurement accuracy and speed. Dots: best spectrum obtained with the near-field microscope (Klar *et al.*, 1998). Red and green (light gray) lines: first single particle spectra observed in a simple far-field setup constructed early in this work (30 minutes measuring time). Black line obtained within 20 seconds with the latest dark-field setup constructed in this work (raw data, no smoothing or averaging).

6. SAMPLES

Two types of metal nanostructures are examined in this study: nanoholes in metal films and nanoparticles of different shape and sizes. The former will be described in Sec. 6.3 at the end of this chapter.

Samples for single nanoparticle spectroscopy should meet two criteria: particle properties have to be well defined and the sample structure should allow easy localization and identification of individual particles. Metal nanoparticles can be produced either by thermal evaporation of metal onto pre-structured substrates or by wet-chemical synthesis. Both methods have been used in the present study due to their respective advantages and will be presented in the following.

6.1 Electron-beam lithography: nanodisks

The important task for the production of metal nanoparticles by thermal evaporation is to structure the substrates. These structures with lateral feature sizes of $> 20\,\mathtt{nm}$ are produced by electron-beam lithography, in which the electron beam of a scanning electron microscope (SEM) is used to expose small areas in a positive resist on top of the sample (Fig. 6.1). These exposed areas are subsequently removed in a chemical development process. If metal is evaporated onto such substrates, the metal is deposited on the substrates in the exposed areas and on the remaining resist on all other parts. By 'lifting off' the remaining resist one ends up with flat metal films at the exposed areas.

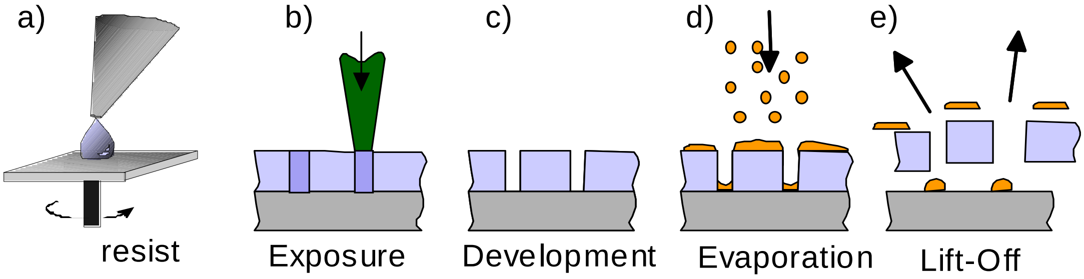

Fig. 6.1: Electron beam lithography processes: a) thin layer of resist spin-cast onto the substrate; b) writing of the structure with an electron beam; c) washing away the exposed areas; d) thermal evaporation of a thin layer of metal; e) removal of the remaining resist and the metal covering it ("lift-off") leaving small metal disks behind.

Electron beam lithography is a standard method to structure semiconductors. For the experiments performed here, transparent substrates have to be used. To remove the electrons deposited during exposure to avoid charging effects, the glass substrates are first covered by a thin conducting layer of indium tin oxide (ITO). Producing nanodisks requires the exposure of circular areas. In practice this is just the area exposed by the electron beam pointed at a single spot if the electron microscope is properly aligned. The disk diameter can be controlled within certain limits by varying the exposure dose (time) because of the Gaussian intensity profile of the electron beam (Fig. 6.2).

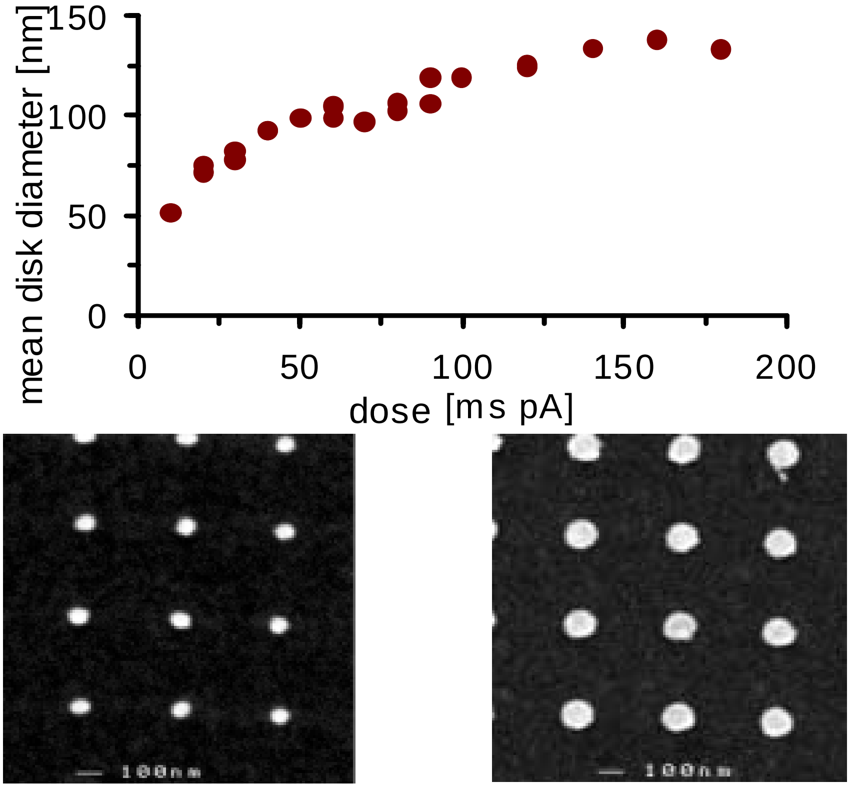

Fig. 6.2: Because of the Gaussian spread of intensity of the electron beam, an increase in exposure dose produces nanodisk of increasing mean diameter as subsequently determined by electron microscopy (top). Sizes between 50 nm (bottom left) and 150 nm (right) were produced by this method (up to 260 nm by additional de-focusing).

Just as important as the careful production of nanoparticles, is the clever design of the macroscopic sample structure with feature sizes on all length scales to allow repeated identification of the same individual particles in different measurements. The structure adopted here is shown in Fig. 6.3 . On a macroscopic level, lines are made by scratching the resist with a fine needle. These lines allow the localization of the exposed area under the microscope as well as in the SEM during sample preparation. Disabling the beam blanker during the exposure process produces thick lines when the electron beam is moved from one area to the next, which connect the exposed areas. The particles are arranged in arrays which consist of nine fields of 14× 14 particles. Particles in a field have the same exposure dose, and each field has a higher dose as compared to the previous field.

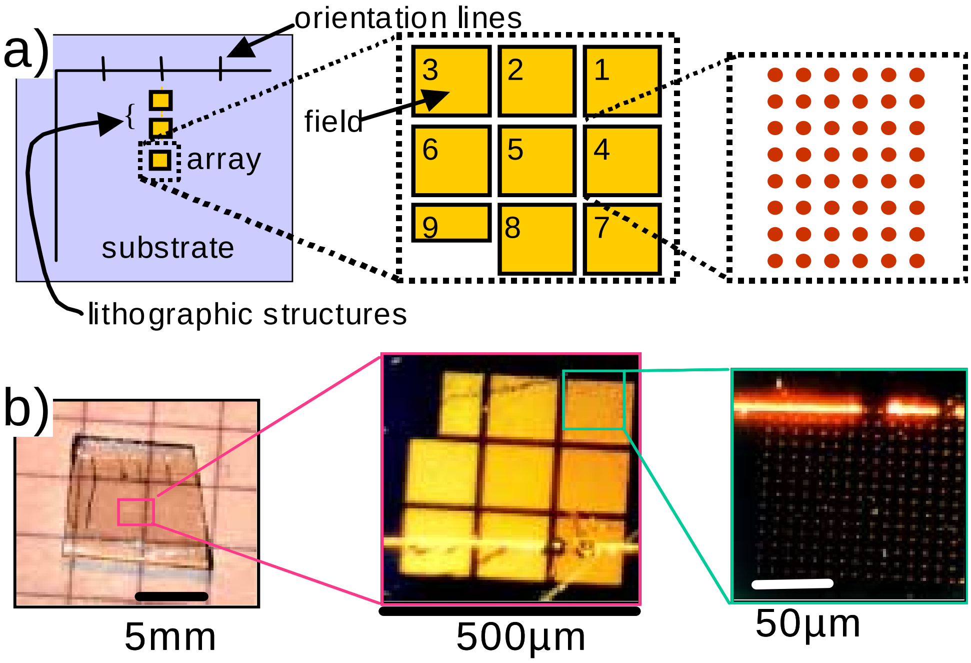
a)
orientation lines
array
substrate
lithographic structures
field
3
2
1
6
5
4
9
8
7
b)
5mm
500µm
50µm

Fig. 6.3: a) Schematic sample structure; b) photographs of a real sample. Increasing magnification from left to right showing the different orientation marks on all length scales down to individual particles (right).

6.2 Chemical synthesis: nanospheres and -rods

Another method to produce nanoparticles is the chemical synthesis by reduction of gold salts in solution. Many different approaches exist, cf. for example Hayat (1989). It is a challenge for chemists to produce monodisperse and monocrystalline particles. Spherical gold and silver particles or nanospheres are commercially available with reasonably small size variations(i). Examples of gold nanospheres of various diameters in aqueous suspensions are shown in Fig. 6.4 together with a transmission electron microscopy (TEM) image. The TEM image shows clearly deviations from the spherical shape due to facets.

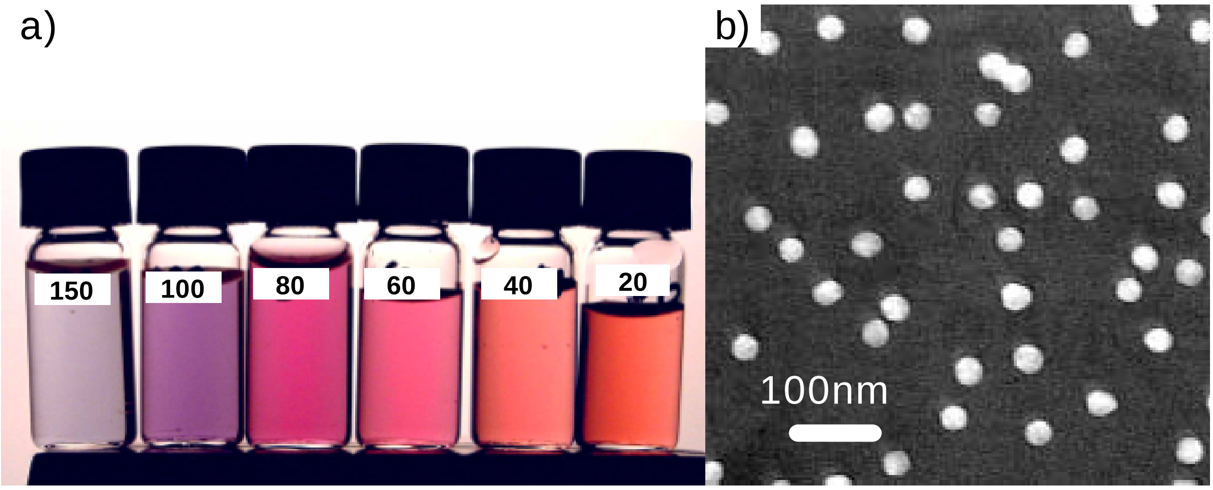

Fig. 6.4: Chemically produced gold and silver spheres in aqueous suspension are commercially available with different mean diameters. Here, gold nanospheres are shown with mean diameters between 20 nm and 150 nm. The transmission electron microscopy (TEM) image on the right shows the inhomogenity in shape among the particles.

The clear advantage of these chemically produced particles is their extremely monocrystalline structure. Their inhomogenity should, however, not be underestimated. Even if their diameter observed by TEM is reasonably uniform, their shape deviations can lead to considerable inhomogeneous effects. This is well illustrated by recent reports of Link and El-Sayed (1999a, 2000), who have produced extremely monodisperse nanosphere samples. They claim a standard deviation in diameter below 1%. Nevertheless, the apparent inhomogeneous broadening in their particle spectra is about 20% compared to the single particle measurements shown later in this work. This highlights the importance of single particle measurements even for apparently monodisperse samples.

In Fig. 6.5 examples of measured and calculated extinction spectra are shown. Clearly the gold nanospheres seem to be in better agreement with theory. One reason is their smaller size variation due to a more optimized production process. Another reason is the uncertainty of the experimentally determined dielectric function of silver which enters the calculation. Two lines are shown for different tabulated values (Johnson and Christy, 1972; Palik, 1985). Clearly a decision about the applicability of either of these tables cannot be made on the basis of the ensemble measurement.

(i) BBInternational, Golden Gate, TY Glas Ave., Cardiff CF4 5DX, UK

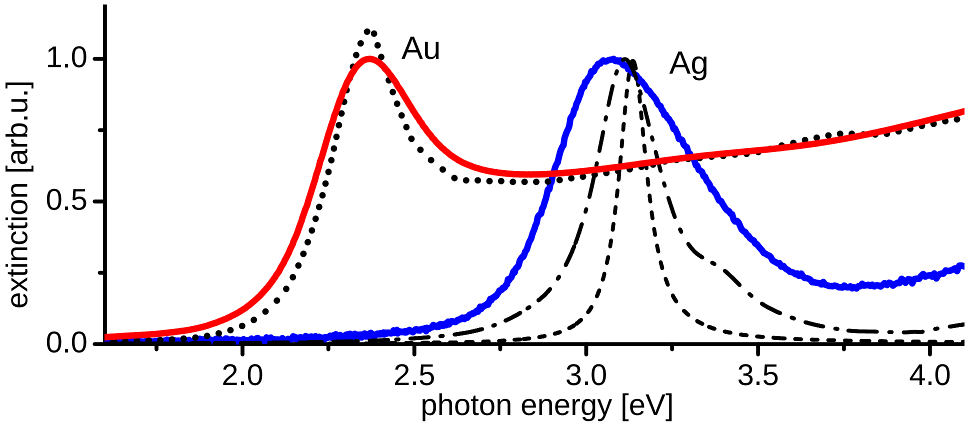

Fig. 6.5: Solid lines : measured ensemble extinction spectra of 20 `nm` gold (left) and silver (right) nanospheres in aqueous solution compared to theoretical calculations based on two different sets of data for the dielectric function (dashed and dotted lines). The observed and calculated spectra for gold nanospheres are very similar, which suggests a relatively monodisperse size distribution. The large discrepancy for silver sphere is partly due to their larger size variation and partly due to less well known input parameters for the theoretical calculations as demonstrated by the two different theoretical lines.

Another type of nanoparticle samples produced chemically are so-called nanorods. Nanorods are typically very small, only 15-20 `nm` in diameter along their short axes. The long axis can be very large, sometimes several hundred nanometers. The rods studied here are produced by Orla Wilson in the group of Paul Mulvaney in cylindrical micelles following the electrochemical method described by Chang *et al.* (1999)(ii). The nanorod suspension contains both spherical and rod-shaped particles. A centrification step (3 500 r.p.m., 20 minutes) removes most of the spheres from the supernatant solution and a further centrification (12 000 r.p.m, 30 minutes) removes any excess surfactant and concentrates the suspension.

The nanorods produced by this methods have many different diameters and aspect ratios as observed by transmission electron microscopy (Fig. 6.6). For single particles spectroscopy this is an *advantage* as those parameters are varied in *one* sample. The enormous advantage of single particle spectroscopy in such inhomogeneous samples is shown in Fig. 6.7 , where ensemble and single particle spectra are compared. In this case, ensemble spectra contain almost zero information about the real system.

(ii) The electrochemical cell consists of a sacrificial gold anode (10× 10× 1 `mm`) and a platinum cathode (10× 40× 1 `mm`) maintained at a separation of 2 `mm`. A silver plate (10× 10× 1 `mm`) is immersed 2 `mm` behind the Pt electrode. The electrolytic solution is made up of 3 $\mathtt{cm}^3$ of 0.08ĉetyltrimethylammonium bromide (CTAB, 99%, BDH Laboratory Supplies) and 10 `mg` of tetraoctylammonium bromide (TOABr, 98%, Aldrich). This solution is sonicated for 10 minutes prior to electrolysis after which time 100 `ml` of acetone and 45 `ml` of cyclohexane are added to assist a) solubilization of TOABr and b) formation of the rod-shaped micelles, respectively. The electrolysis is carried out at 3.5 `mA` for 45 minutes in an ultrasonic bath maintained at a temperature of 35°C during the reaction.

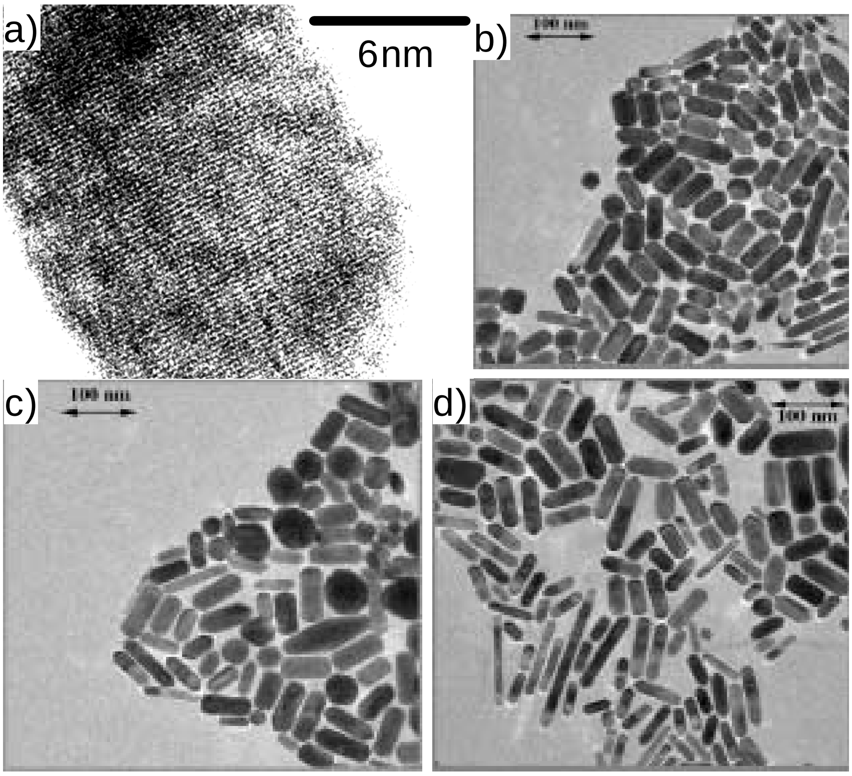

Fig. 6.6: Transmission electron microscopy (TEM) images of gold nanorods from the sample studied in this work. a) high resolution image resolving the gold lattice planes indicating the mono-crystallinity of the nanorods. Images b)-d) show the large size and shape variations. (TEM images by Michael Giersing, Berlin.)

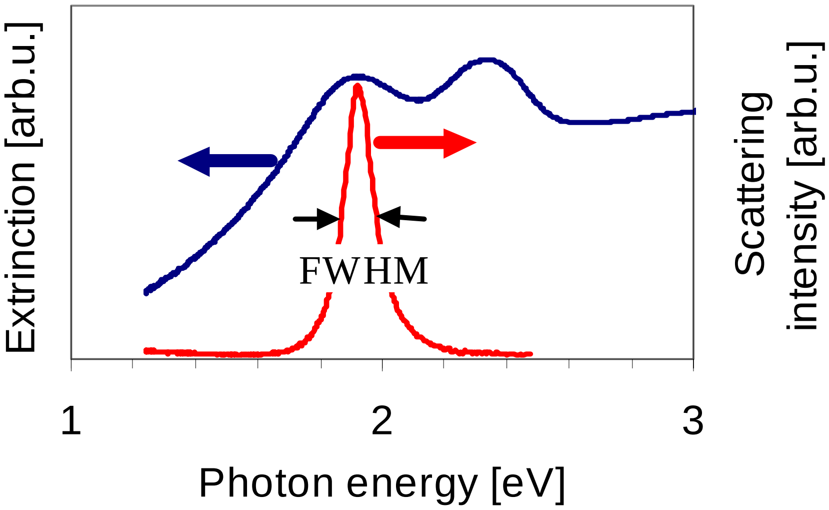

Fig. 6.7: Ensemble extinction spectrum and single particle scattering spectrum to demonstrate the large inhomogeneous broadening in the ensemble spectra of nanorods.

6.2.1 Sample preparation

The nanoparticles described above are produced and stored in aqueous suspensions. In order to investigate them in a microscopic setup, they are fixed to a glass substrate. To increase adhesion to the glass surface, the glass is prepared with an adhesion layer of a positively charged polymer (the particles themselves are slightly negatively charged). Subsequently, a properly diluted suspension of particles is spin-cast onto the substrate (Fig. 6.8). Visual inspection in the dark-field microscope immediately shows the average spacing of the particles, which has to be adjusted to about 10 μm for single particle spectroscopy.

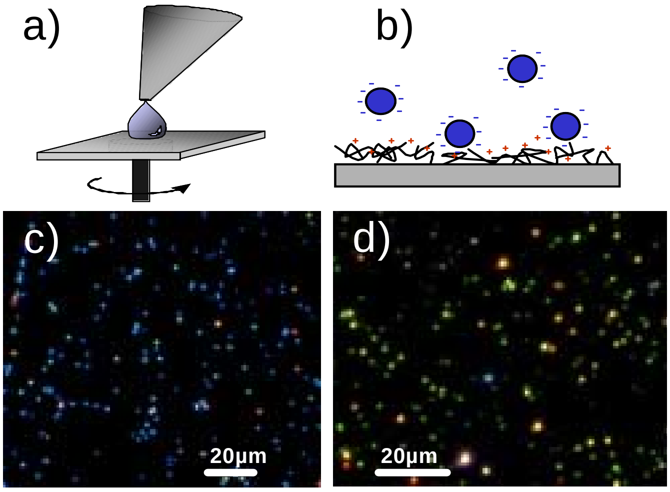

Fig. 6.8: a) Sample preparation procedure: a dilute solution of negatively charged nanoparticles in suspension are spin-cast on clean glass substrates prepared with a positively charged adhesion layer b). The average particle spacing can be checked in a dark-field microscope: c) silver, d) gold nanospheres.

More difficult is the task to introduce structures which allow identification of individual particles. Scratching the surface carefully with a soft needle wipes the particles away leaving clearly visible ‘gaps’. Care has to be taken not to damage the glass surface as this produces strong stray light. Crossing points of such lines (or with naturally occurring lines), can be used to identify a specific sample area. A sketch of the particles in this area allows then the identification of individual particles (Fig. 6.9).

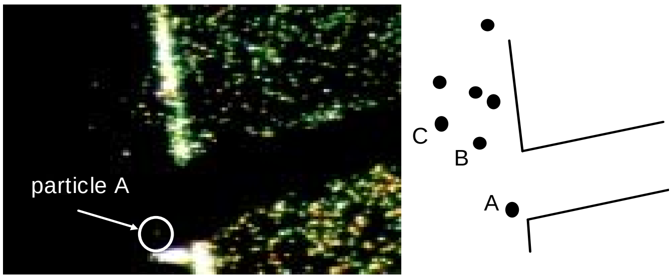

Fig. 6.9: Lines drawn with a soft needle (left to right) allows identification and mapping of individual particles (right).

Another, more difficult but more elaborate method developed at the University of Ulm (Chan *et al.*, 2001) has been employed briefly during initial experiments. Pre-structuring the sample by electron beam lithography before spin-casting the particle solution leads to a selective deposition of particles in the holes produced lithographically in the resist (cf. Fig. 6.10). Metallic nanoparticles sequestered within large micelles are used in order to allow only one particle in a hole. Chemical groups in the outside bind to the glass surface. Washing away the resist together with the micelles produces samples with particles only at the desired positions.

This method allows the structuring of chemically produced nanoparticles. However, for single particle spectroscopy, the exact arrangement of particles is not of huge importance, thus the more simple spin-casting method is preferred here. Only at an early stage was the arrangement used to check the reliability of the single particle scattering spectroscopy setups by comparing the observed patterns with the patterns designed by this electron-beam lithography method.

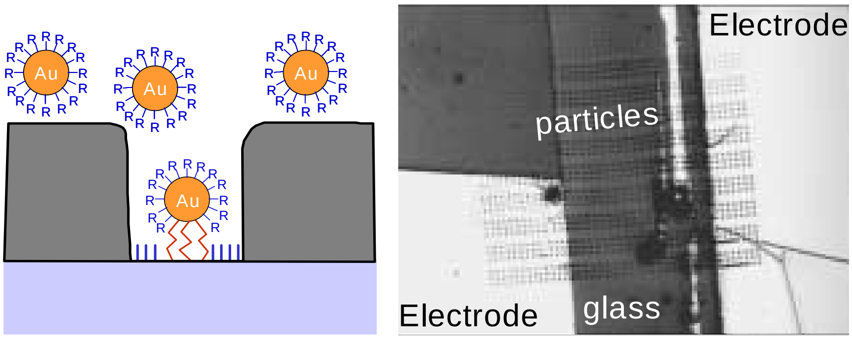

Fig. 6.10: Patterning of nanoparticles in artificial structures written by electron beam lithography into resist on glass substrates. The nanoparticles are enclosed by micelles functionallized by chemical groups to bind to the glass substrates in the areas not covered by the resist (left). After washing away the resist together with the remaining particles, only tightly bound particles remain on the substrate. An array of particles placed between and on top of two electrodes is shown in a microscopic image on the right (left electrode partially removed).

6.3 Nanoholes in gold, silver and aluminum films

With a combination of the techniques described above, the opposite to metal nanoparticles can also be produced: nanoholes in a metal film. Polystyrene spheres are randomly distributed on the surface of a glass substrate by spin-casting a dilute suspension which is then used as a mask for the evaporation process. The average distance between holes can be controlled by varying the concentration of the suspension before spin-casting. After the metal is evaporated onto the substrate, the spheres are removed together with the metal covering leaving holes at the original positions of the spheres (Fig. 6.11). This method is similar to the projection pattern described by Fischer (1986) where densely packed ordered arrays of polystyrene spheres are used to produce triangular shaped islands.

Polystyrene spheres are commercially available with extremely narrow size distribution ($< 2\%$). The holes produced by this method have exactly the particle size and very

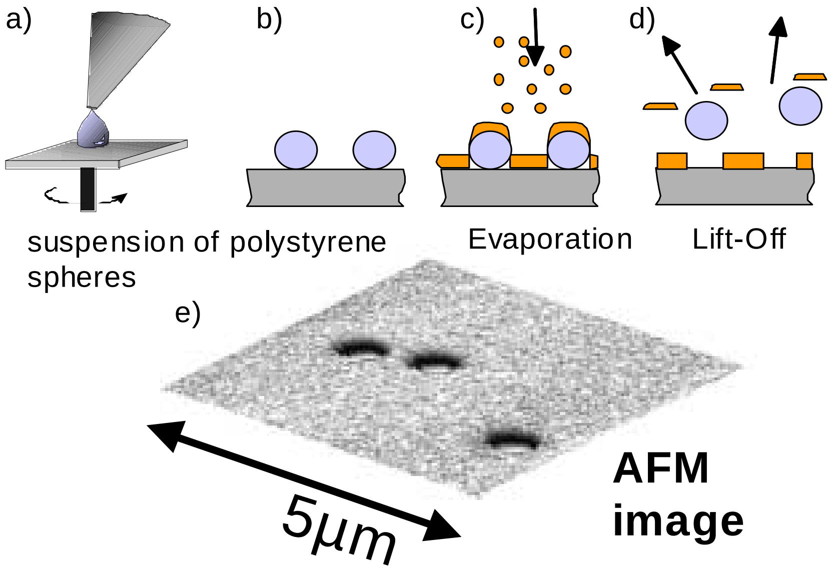

Fig. 6.11: Production of nanoholes: a suspension of polystyrene spheres is spin-cast on a glass substrate (a) resulting in a random distribution of spheres on the substrate (b). Gold is evaporated on top (c). After removal of the spheres (d), uniformly sized holes remain at the positions originally occupied by the spheres (e).

smooth borders as shown by atomic force microscopy (AFM) (Fig. 6.11 e) The metal film thickness is chosen to be large enough to prevent any direct light transmission through the film ($\approx 130\,\mathtt{nm}$). To ensure homogeneous metal films, an adhesion layer of a few nanometers of chromium-nickel is used, which is evaporated onto the substrate prior to the metal film.

7. LIGHT TRANSMISSION THROUGH NANOHOLES

As discussed in Sec. 3.5 , the mechanism of light transmission through subwavelength sized holes in optically opaque metal films has been the subject of recent discussion due to the surprisingly large light transmission through regular arrays of subwavelength sized holes in metal films (Ebbesen *et al.*, 1998).

The aim of the experiments described in this chapter is to investigate this mechanism using scanning near-field optical microscopy (SNOM). The results show unambiguously that excitation and lateral propagation of surface plasmons support the light transmission through these nanoholes. The direction of the surface plasmon propagation is given by the light polarization, thus controlled addressing of individual holes is possible. In addition, characteristic interference effects due to scattering of surface plasmons off holes are observed.

7.1 Experimental configuration

The experimental configuration is schematically shown in Fig. 7.1 b. The samples consist of opaque gold, silver or aluminum films of 130 nm thickness with randomly arranged holes of 300 nm diameter (the production process was described in Sec. 6.3). I aim to investigate the interaction of surface plasmons with individual holes in these metal films. The illumination mode scanning near-field microscope described in Sec. 5.1 is used to locally launch surface plasmons. The SNOM tip represents a point source of surface plasmons which is scanned across the surface area around one individual hole. The light associated with the radiative decay of surface plasmons is measured on the other side of the film by a photo diode. The metal films are thick enough to prevent direct light transmission through the films ($< 10^{-3}$) and to suppress the direct coupling of surface plasmons on the two sides of the films. Therefore light transmission can only occur via the holes. In most cases I select areas of the samples with spacings between the holes larger than the surface plasmon decay length, so that in these cases all light originates from one individual hole. A tunable c.w. dye laser (wavelength range 520-570 nm), a helium-neon laser (633 nm) and a tunable c.w. titanium:sapphire laser (880-1000 nm) are used as light sources.

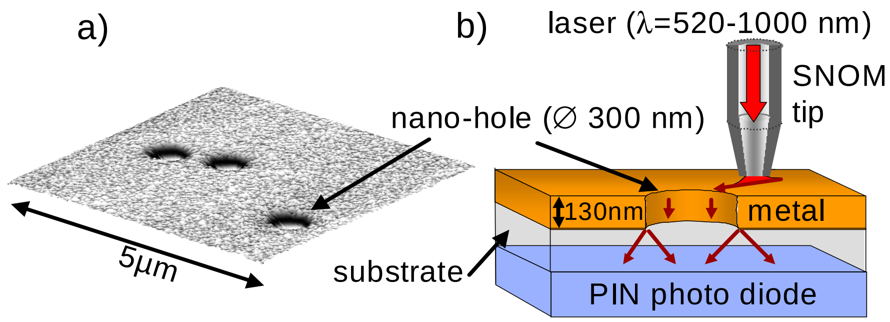

Fig. 7.1: a) Surface topography as measured by atomic force microscopy (AFM). The holes have a diameter of 300 nm. b) Experimental setup.

7.2 Experimental results

Fig. 7.2 shows a SNOM image taken on a gold film with 300 nm holes. It shows pronounced light-intensity maxima at the spatial positions of the holes confined to approximately the geometrical hole area. In addition, a weaker intensity is observed within an area elongated along the diagonal of the image. The direction of this prolate area is the same for all holes. A closeup scan around the area of one hole shows that the extent of this prolate area is much larger than the geometrical extent of the hole (Fig. 7.3). The extent and shape of this pattern is very similar for all excitation wavelengths (520-1000 nm) and metals (Al, Au, Ag).

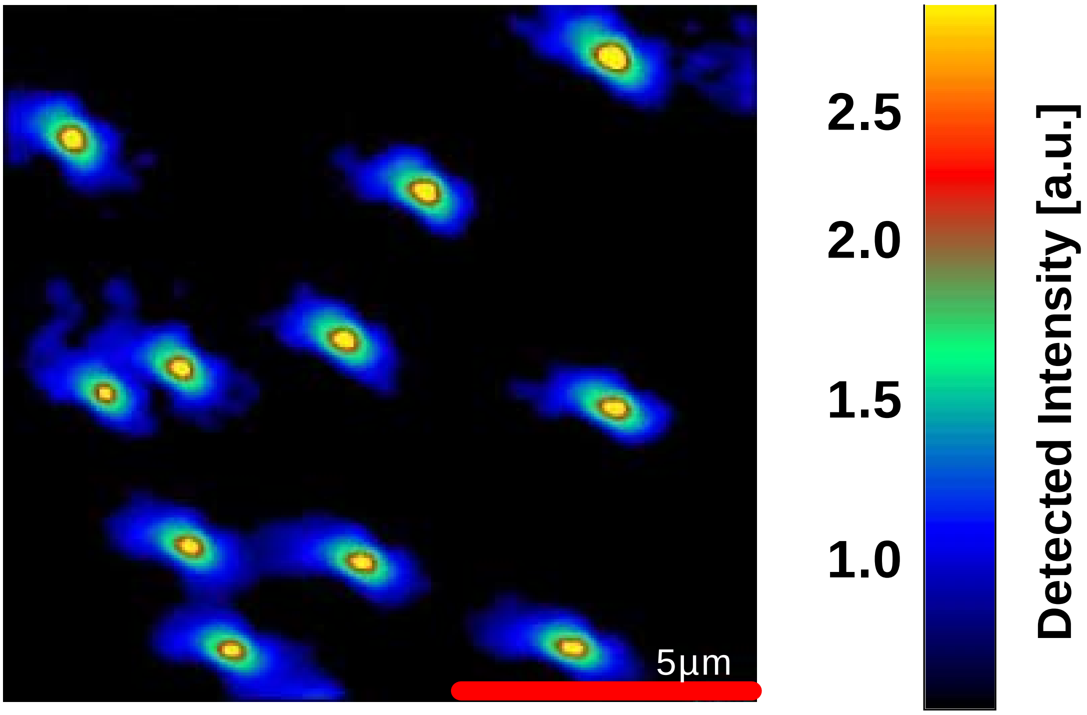

Fig. 7.2: SNOM image for a large area scan of a nanohole sample with 300 nm holes in a gold film for an illumination wavelength of 990 nm.

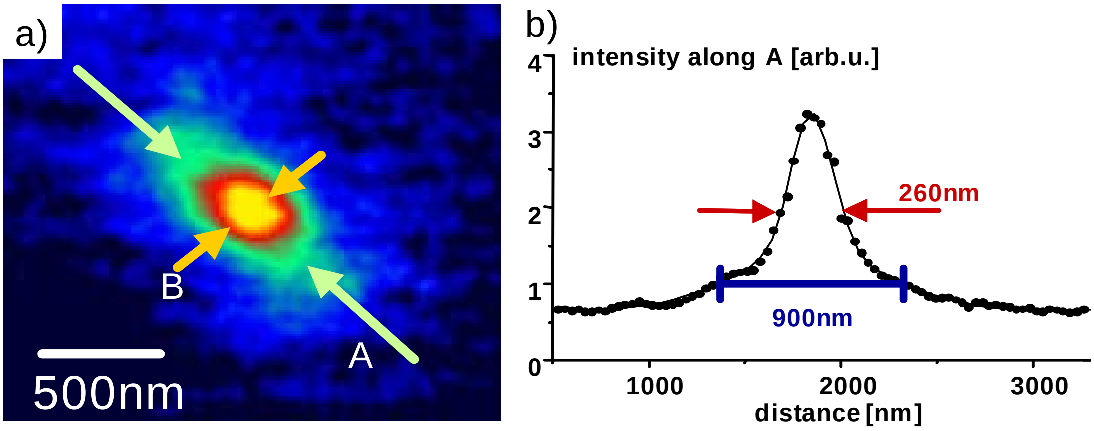

Fig. 7.3: a) Higher magnification of one of the holes in Fig. 7.2 . The image is composed of a circular central peak and an elongated shape extending farther out (long/short direction indicated by arrows A/B, respectively). Color-scale as in Fig. 7.2 .
b) A line-cut in the direction of A shows the intense central peak — with a width (260 nm) of approximately the hole diameter (300 nm) — and tails extending much farther out (900 nm)

7.2.1 Polarization effect

The direction of this prolate area rotates with the polarization of the incident light, as shown by Fig. 7.4 . This proves that it is not due to tip artifacts.

It is known from Hecht *et al.* (1996) that surface plasmons launched by a SNOM tip exhibit a $\cos^2\phi$ dependence of their density on the angle ϕ with respect to the polarization direction. The prolate intensity distribution therefore confirms the surface plasmon excitation by the SNOM tip. These surface plasmons will propagate along the surface of the film until they encounter a hole. There they are transformed into radiation, possibly by direct interaction with the edges of the hole or via coupling to surface plasmon modes at the rear surface of the film and subsequent radiative decay of those modes. In contrast to the surface plasmon contribution to the measured light intensity, the central peak in Fig. 7.4 is essentially independent of the light polarization. This peak is attributed to direct transmission through the hole of propagating light modes emitted by the SNOM tip.

7.2.2 Wavelength effect

Qualitatively the same pattern observed in Fig. 7.4 is found at all illumination wavelengths used here (520 nm–570 nm, 633*nm* and 880 nm–1000 nm), for gold, silver and aluminum films and for holes with diameters of 300 nm and 500 nm. The spatial extent of the prolate surface plasmon pattern does not change appreciably with excitation wavelength. This is surprising at first, since the propagation length of surface plasmons is known to change dramatically with wavelength and material. Here, however, the lateral divergence of the surface plasmons seems to be the dominant effect. The symmetric, central transmission peak at the position of the hole changes both in absolute intensity and in relative intensity compared to the prolate region when the excitation wavelength is changed. This might be

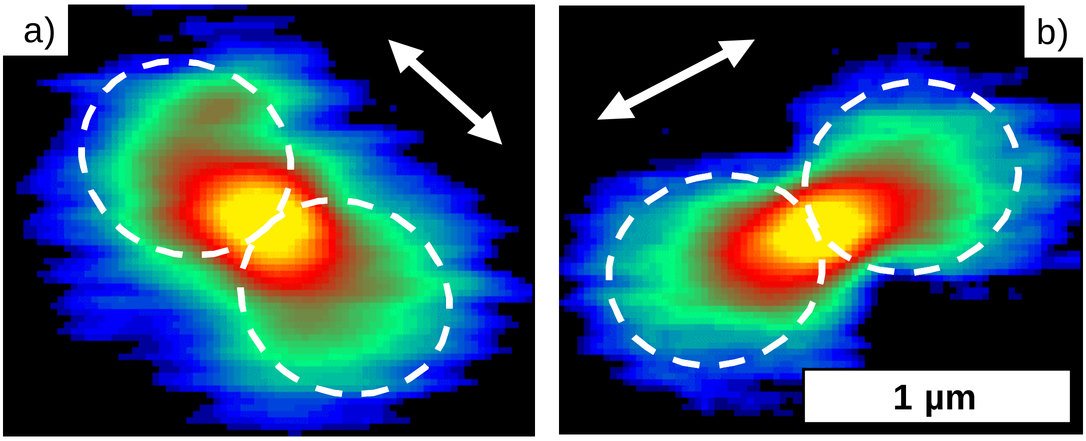

Fig. 7.4: SNOM images of a 300 nm hole in gold at an illumination wavelength of 900 nm for two different angles of polarization of the exciting light. The different orientations of the prolate shapes in a) and b) (indicated by the dashed lines) proves the directed launching of surface plasmons in the direction of polarization (arrows). The absolute polarization direction at the SNOM tip is not known from the measurement because of unknown bends and twists of the fiber, thus the directions indicated by the arrows are interpreted from the form of the observed pattern. (Color-scale as in Fig. 7.2 .)

due to a wavelength dependence of the coupling efficiency of the tip to surface plasmons on the sample and to transmission properties of the near-field probe itself.

7.2.3 Interferences

Fig. 7.5 shows the results of SNOM measurements on a portion of a silver film where a hole lies in close proximity (2.5μm distance) to another (double) hole; the relative positions are shown in Fig. 7.5 d. Fig. 7.5 a and b show, for two different light polarizations, the part of the scanned area indicated by the dotted box in d. In Fig. 7.5 a a periodic structure along the connecting line between the two holes is observed. The observed periodicity of $290 - 340$ nm corresponds within experimental uncertainty to half of the expected surface plasmon wavelength ($\approx$ 260 nm) and changes with the illumination light frequency as expected from the surface plasmon dispersion.

This pattern is explained by scattering of surface plasmons off one of the holes in the direction of the other one (as indicated in Fig. 7.5 c). At the location of the latter, the scattered surface plasmons interfere with the surface plasmons coming directly from the tip. The interference pattern disappears by changing the light polarization as seen in Fig. 7.5 b, because the surface plasmons no longer propagate along the connecting line of the holes (Fig. 7.5 e).

7.3 Conclusion

In conclusion, I have investigated optical transmission through individual nanoholes in gold, silver, and aluminum films. Using a SNOM in illumination mode, surface plasmons

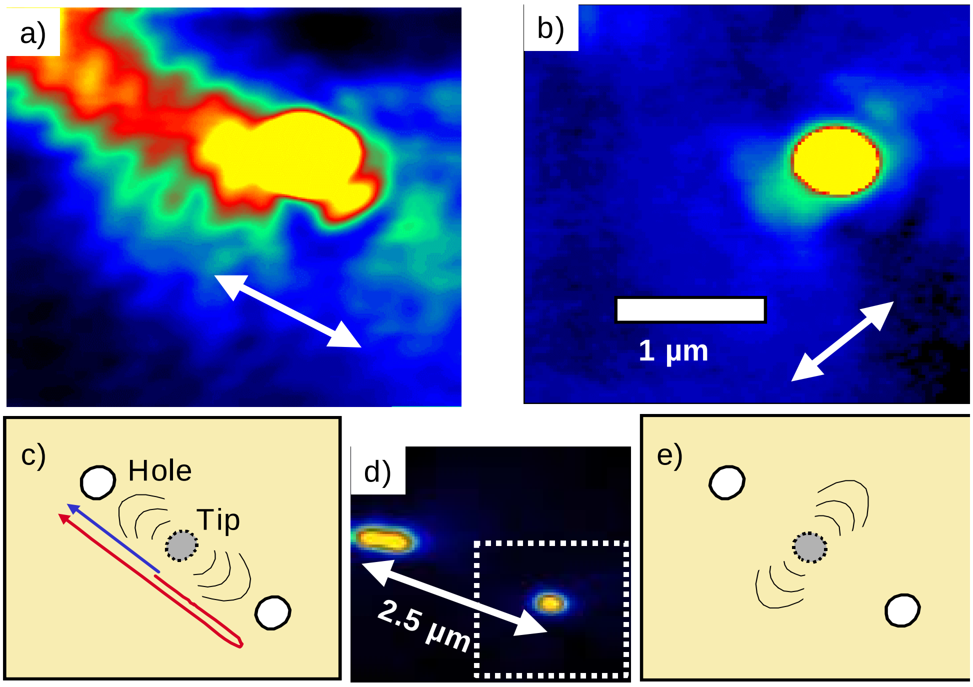

Fig. 7.5: a) and b) are close-up SNOM images of a silver film at 550 `nm` illumination wavelength in the area indicated by the dotted box in d). (Color-scale as in Fig. 7.2.) The interference pattern in a) is explained by the process indicated in c): at each hole surface plasmons coming from the tip directly and indirectly (scattered off the other hole) interfere. The pattern disappears by changing the polarization, b); this is a consequence of the directed propagation of surface plasmons, e).

were locally excited on the films. This approach avoids complications associated with surface-plasmon excitation via gratings. The patterns observed show unambiguously that light transmission through the nanoholes is supported by surface plasmons propagating along the surface of the films. The propagation direction is given by the light polarization. I have found characteristic interference effects due to scattering of surface plasmons off neighboring holes.

The directed launching of surface plasmons below a SNOM tip may be used to selectively transmit light through distinct holes according to the light polarization in the fiber — a process that may figuratively be described as “nanogolf”. This polarization controlled addressing of specific holes may be applicable for de-multiplexing purposes in future optical systems.

8. PARTICLE PLASMON DAMPING

As mentioned in Sec. 4.6 , the amount of particle plasmon damping (described by the dephasing time) has received considerable attention during the last decade, without obtaining satisfying results.

In the following sections experimentally determined dephasing times for a range of different nanoparticle samples are reported. The dephasing time is deduced from the homogeneous linewidth which is determined by spectrally investigating the scattering efficiency of individual particles using the experimental methods described in Chap. 5 .

In this chapter, I will first separately present experiments on gold nanodisks, gold and silver nanospheres and nanorods. Since each class of particles is investigated with slightly different experimental methods, I will briefly mention those wherever necessary. A comparison and discussion of the relevance of the results will be presented at the end of the chapter.

The results shown in the following not only give reliable *values* for dephasing times for a number of nanoparticle classes, but also allow to deduce the underlying damping *mechanisms*. In addition, the results allow the deduction of — for the particle classes under investigation — the *local field enhancement factors*, which is the figure of merit for nonlinear optical applications of nanoparticles.

8.1 Gold nanodisks

Nanodisks are produced by electron beam lithography (cf. Sec. 6.1) which has the big advantage that it allows the controlled arrangement of the particles on the substrate during the production process. Studying samples with known particle arrangement has been an important test of the single particle spectroscopy setup. By comparing the observed pattern to the known arrangement, it allows the establishment that the observed scattering centers may be attributed to single particles. Hence, an important reason for studying nanodisks is the check of the single particle spectroscopy setup. The main purpose for the study on nanodisks is, however, to determine their dephasing time. It is possible to obtain nanodisks of any aspect ratio and volume by adjusting their diameters and height independently. (In practice, this is a very laborious process.) Examples of scattering spectra for two samples with nanodisks of different height will be presented here. Dephasing times extracted from these range from T_2=1.9 to 7.3 `fs`. An increase of the dephasing rate with the volume of the nanodisks is observed.

The experiments are performed using a simple total internal reflection (TIR) setup (cf. Sec. 5), where the particle plasmon resonance is excited by an evanescent field produced by a white light beam undergoing total internal reflection at the substrate surface (Fig. 8.1 , inset). The nanodisks are therefore on one side exposed to air and on the other side to the substrate, which is glass covered by a thin layer of indium tin oxide (ITO) in this case.

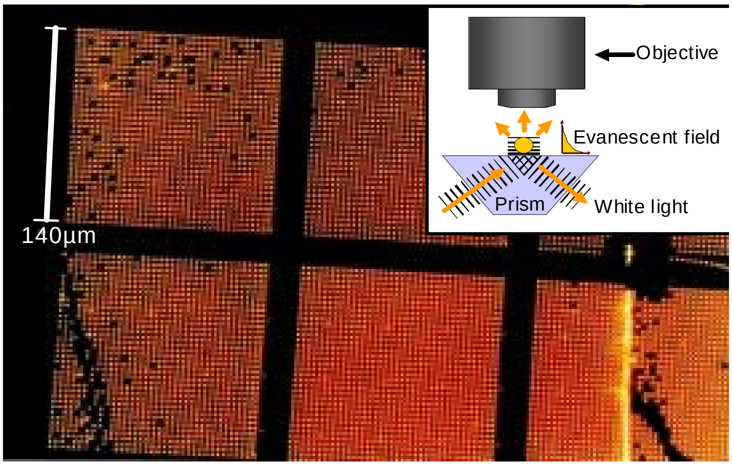

Fig. 8.1: True color photograph of a nanodisk sample. 35 × 35 disks of the same nominal diameter are arranged in an array. Each of these arrays has a different nominal disk diameter. For example, the nominal nanodisk diameter increases in the three arrays in the second row from left to right.
Inset: setup used to obtain the photograph and single nanodisk spectra. Total internal reflection of white light at one side of a prism produces an evanescent field. Metal particles placed in this field scatter the light which is observed with a conventional microscope.

The obtained contrast (signal to background) is very large, up to 100:1 (Fig. 8.1). In contrast to conventional fluorescence microscopy, where the background is eliminated by spectrally filtering out the excitation light, the contrast is purely due to a suppression of direct light transmission. The extremely low background signal allows the observation of very small light scatterers. By comparing the image observed in the microscope with the real arrangement of particles on the sample known from the production process, it is possible to prove that the individual light scatterers are indeed single nanodisks.

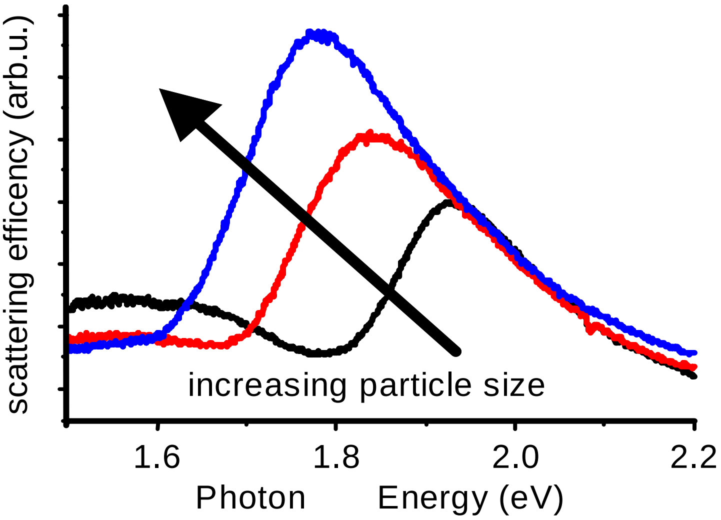

Fig. 8.2: Examples of single particle spectra. Larger particles show an increased intensity, a larger linewidth, and a red shift of the resonance energy.

The measured spectral composition of light scattered by gold islands with various diameters is shown in Fig. 8.2 . The observed maxima are caused by the resonant excitation of particle plasmons. It is clearly observed that the particle plasmon resonance of larger particles shifts towards the red end of the spectrum and the peak broadens. The red shift is expected from the higher aspect ratio and increased electromagnetic retardation effect of larger particles (Kreibig and Vollmer, 1995). The observed increase in scattering intensity of larger particles is mainly a consequence of their larger volume.

To investigate the plasmon resonances of different particles more systematically, I extract the homogeneous linewidth Γ (full width at half maximum, FWHM) and peak position E_{res} of the plasmon resonance for each measured spectrum. Both increasing volume and increasing aspect ratio lead to a red-shift of the plasmon resonance (Sec. 4.5.4). The peak position E_{res} is therefore a convenient measure of the particle form. The results of this analysis are shown in Fig. 8.3 , where linewidth is plotted against resonance energy for two nanodisk samples with 15 nm and 25 nm height, respectively, and disk diameters between 68 nm and 260 nm (i). The data in Fig. 8.3 demonstrate a larger linewidth for more red-shifted plasmons in nanodisks. The increase in linewidth is stronger for disks with 25 nm height compared to disks with 15 nm height.

Since nonradiative damping in gold particles is expected to be approximatively constant for resonance energies below 1.8 eV (cf. end of this chapter), the drastic increase in linewidth has to be due to an increased radiation damping. This can be understood in a more quantitative way by the following arguments: The resonance position is — to a first approximation — a function of only the aspect ratio, since the red-shift due to the increased particle volume should be relatively small. Thus, if we compare nanodisks

---

(i) Plotting linewidth versus resonance energy is attributed (Kreibig and Vollmer, 1995) to K.J. Berg and therefore sometimes called “Berg-plot”.

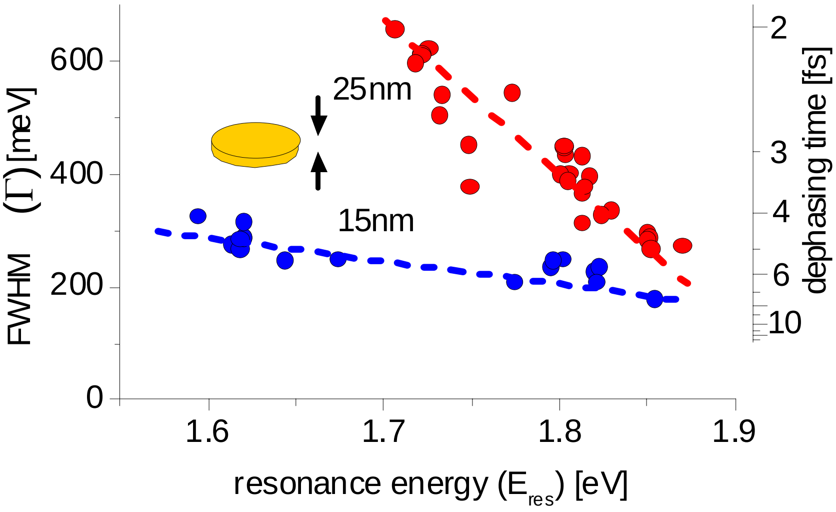

Fig. 8.3: Full linewidth at half maximum (FWHM) of the plasmon resonance in individual nanodisks plotted against the corresponding resonance energy. Data for two samples of nanodisks with different heights (15 and 25 nm) and diameters ranging from 68 nm to 260 nm. The dotted lines indicate the general trend.

with the same resonance energy, they should roughly have the same aspect ratio. The difference in linewidth between the two samples of different height is therefore due to the larger *volume* of the thicker nanodisks. The volume ratio for particles of the same aspect ratio is about $25^3/15^3 \approx 5$, which is very roughly the difference in slope for the increase in linewidth as function of resonance energy, cf. Fig. 8.3. This is an indication that radiation damping increases with the volume to the power of one. Even though these arguments are more or less indirect, this finding is correct as confirmed by measurements on nanorods and -spheres, which will be discussed at the end of this chapter.

Since the spectra are taken from individual particles, the linewidth is the intrinsic homogeneous linewidth, which is directly related to the dephasing time T_2 by $T_2 = \Gamma/2\hbar$. The widths of the particle plasmon resonances shown in Fig. 8.3 correspond to dephasing times of 1.9 fs to 7.3 fs. It is difficult to compare this to theory, since an exact analytic solution for particle plasmon decay including radiation damping is only available for spherical particles and homogeneous embedding media (Mie theory). Numerical calculations based on Green's dyadic method (Lamprecht *et al.*, 1997), which allows arbitrary particle and substrate geometries, predict decay times between 3 and 9 fs for particle sizes and shapes similar to my experiments. This is a reasonable agreement with my measurements taking into account the large uncertainty about the exact microscopic shape of the particles and the embedding medium.

Another important quantity follows immediately from the results in Fig. 8.3: the quality factor of the resonance $Q = E_{\mathrm{res}}/\Gamma$. For weakly damped oscillators, the quality factor is the enhancement of the oscillation amplitude with respect to the driving amplitude, i.e. in the case of particle plasmons the local field enhancement. This value is the figure of merit for all nonlinear applications of particle plasmons such as surface enhanced Raman scattering (SERS), which is believed (Moskovits, 1985; Michaels *et al.*, 2000) to depend on

Q^4. The quality factors for the nanodisks studied here are between 2.5 and 11 as shown in Fig. 8.4 . It decreases for increasing red-shift and is generally larger for the thinner nanodisks.

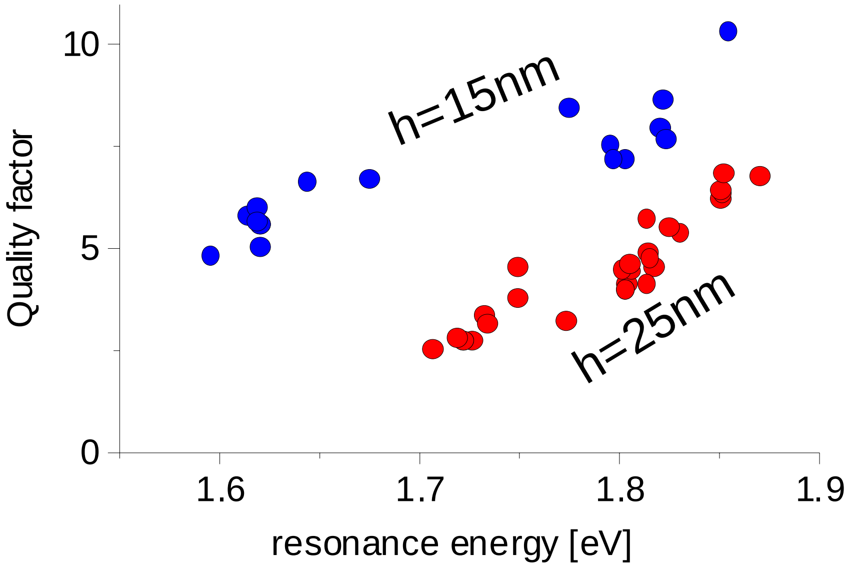

Fig. 8.4: Quality factors for the plasmon resonance in individual nanodisks plotted against the corresponding resonance energy. Data for two samples of nanodisks with different heights (15 and 25 `nm`).

The results in this section demonstrate the ability to measure the particle plasmon resonance of *individual* metallic nanoparticles (here nanodisks) by spectrally investigating the light scattered by these particles. The homogeneous linewidth of the particle plasmon resonance of individual gold nanodisks with diameters between 68 `nm` and 260 `nm` and heights of either 15 `nm` or 25 `nm` is determined. The observed *homogeneous* linewidths Γ between 180 and 680 `meV` correspond to dephasing times of $T_2 = 1.9$ `fs` to 7.3 `fs` and quality factors Q between 2.5 and 11. For these measurements, the nanodisks are supported by a substrate of indium tin oxide (ITO) covered glass and exposed to air. This inhomogeneous environment makes comparison with theory difficult. The interpretation of the results is further complicated by the simultaneous increase in volume *and* aspect ratio for disks with larger diameters. Even though indirect arguments strongly suggest that increased radiation damping causes the increased linewidth observed for more red-shifted resonances, more controlled experiments are highly desirable. This can be achieved by studying nanospheres embedded in a homogeneous matrix as shown in the next section.

8.2 Gold nanospheres

Nanospheres are easily produced in large quantities by reduction of gold salts and thus widely used, for example as labels for biological substances in electron microscopy (Hayat, 1989). They are an important type of nanoparticles not only because of their frequent usage in biological science, but also for fundamental reasons: spheres are the only shape of particles for which theoretical calculations including retardation effects are easily possible (Sec. 4.5.3). The strong shape dependence of the plasmon resonance is avoided which allows to study the size effect separately.

In order to allow a comparison with theory, all nanoparticles studied in this section are supported by a glass substrate and embedded in immersion oil. This ensures a homogeneous and isotropic refractive index around the particles, which is, effectively, the same as embedding the particles in a glass matrix. The scattering spectra are collected using the dark-field setup in transmission as described in Sec. 5.2.3 . The actual configuration for the experiments described in this section is shown in Fig. 8.5 . To ensure that only spherical particles are considered for the following discussion, each single particle spectrum is recorded at least three times for different polarization directions of the exciting light. Strongly irregular shaped particles will show a shift in resonance frequency depending on the polarization angle as will be shown in Sec. 8.4 . Here, only particles are considered which showed a polarization dependent shift of resonance frequency of less than 1%.

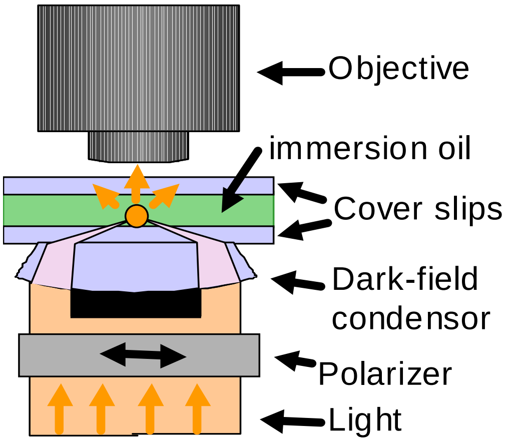

Fig. 8.5: Experimental configuration used here: Nanospheres are embedded in immersion oil and sandwiched between two cover-slips. Since good correction is crucial to achieve high resolution and contrast in the collection of scattered light, an objective with 63× magnification and adjustable correction for the top cover-slip and the layer of oil is used.

Some examples of scattering spectra for gold nanospheres of different nominal diameters are shown in Fig. 8.6 . In this figure they are also compared to theoretical calculations using the Mie theory described in Sec. 4.5.3 with the nominal diameter of the spheres and bulk values for the dielectric function. Note that the theory has no additional free parameters! It is remarkable how accurately the theory describes not only peak position and linewidth but also the exact shape of the spectrum. It is also noteworthy that the experimental spectrum clearly resolves the quadrupole peak at the high energy side of the plasmon resonance in 150 nm particles. Comparing the spectra of different sizes, it is clear that the resonance energy shifts towards lower energies for increasing nanosphere diameter and at the same time the linewidth increases.

The perfect agreement of spectral position, width and exact lineshape between experiment and theory has some important implications. Since the calculation uses bulk values for the dielectric function for gold, all damping mechanisms have to be already included in these values. In particular, no contributions from surface effects such as surface scattering or chemical adsorbate damping are observed. Also, a significant contribution of non-local effects can be excluded. This excludes *collective* dephasing of the whole plasmon, for example, by a collective scattering with a particle phonon-mode. The dephasing of the collective oscillation is thus well described by single electron dephasing.

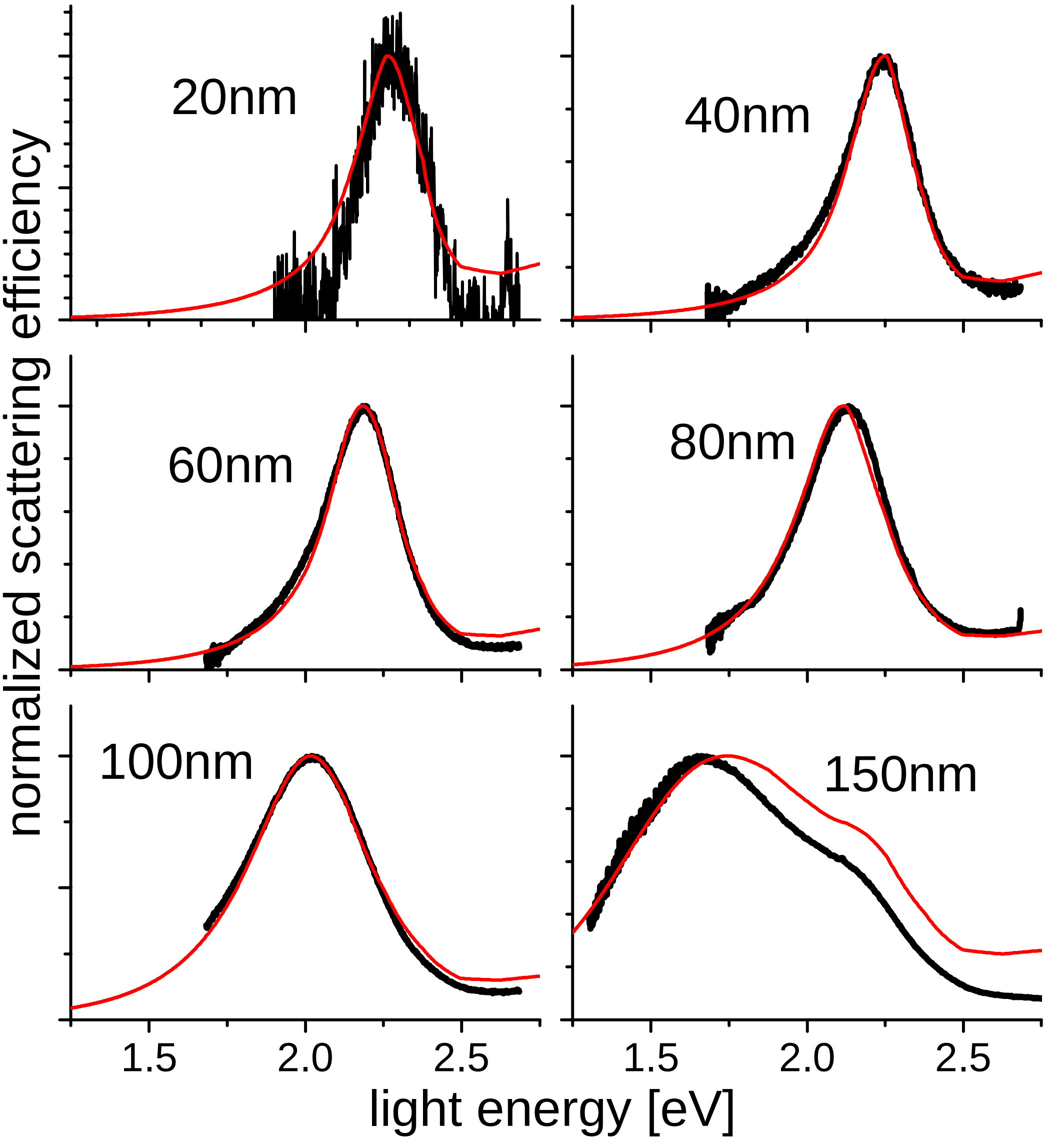

Fig. 8.6: Measured scattering spectra for gold nanospheres of different diameters (as indicated in the graphs) compared to theoretical calculations using the Mie theory described in Sec. 4.5.3 (theory: light lines, whole energy range; experiment: dark lines, from 1.65 – 2.65 `eV`). The theory describes remarkably accurately not only peak position and linewidth, but also the exact shape of the spectrum. Note the well resolved quadrupole peak in the spectrum for the 150 `nm` particle. The slight deviation from theory in this case results from a difference in excitation and collection geometry.

To systematically compare a greater number of single particle spectra than those shown in Fig. 8.6 , I use again a plot of linewidth versus resonance energy, both of which are extracted from the single particle spectra. The result is shown in Fig. 8.7 a[(ii)]. The spectra for different nominal sizes are distinguished by color. Theoretical results using Mie theory with bulk values for the dielectric function are shown for different sphere diameters by the solid line. The calculated values for diameters of 10, 20, 30,... 160 `nm` are indicated by small triangles.

The experimental error is indicated by the bars and is sometimes better than the symbol size, i.e., the apparent distribution of resonance position and linewidth around the general trend is due to intrinsic sample properties. Small variations in the particle environment due to contamination on a molecular scale, charges in or on the particles or the facetting of the particle surfaces could be responsible for this distribution. However, the experimentally observed trend follows the theoretical prediction, which yields an increase of damping for larger particles. The reason for this is increased radiation damping as illustrated at the end of this chapter.

The quality factor or local field enhancement factor Q calculated from these data is shown in Fig. 8.7 b. The quality factor decreases for increasing particle diameter from approximately 7.5 for $20 - 40$ `nm` spheres to values of only 2.5 for spheres with 150 `nm` diameter.

Of course, the dephasing times T_2 can be deduced from the measured homogeneous linewidths Γ as shown by the right-hand scale in Fig. 8.7 a. As mentioned above, we can conclude from the good agreement of theory and experiment that collective dephasing is negligible, so these dephasing times directly relate to the plasmon lifetime τ or population decay time T_1 via $\tau \equiv T_1 = T_2/2$. The mean values for each nominal size are summarized in Tab. 8.1 .

d [nm]	20	40	60	80	100	150
T_2 [fs]	4.6	4.5	4.1	3.3	2.7	2.1
$\tau \equiv T_1$ [fs]	2.3	2.3	2.1	1.6	1.4	1.1

Tab. 8.1: Dephasing times T_2 and lifetime τ of gold nanospheres with different diameter d embedded in a matrix with refractive index $n = 1.5$.

In conclusion, the data presented in this section give a reliable answer to the long debated question of the dephasing time of plasmons in spherical gold particles. It is shown that this dephasing time decreases with increasing particle diameter, possibly due to increased radiation damping (see the discussion at the end of this chapter). The good agreement with theoretical calculations using the bulk dielectric function for gold, lets me conclude that surface and non-local dephasing processes do not contribute significantly in my samples. The dephasing time is therefore directly connected with the particle plasmon lifetime $\tau \equiv T_1$. In addition I determine the local field enhancement factor or quality factor Q for gold nanospheres between 20 and 150 `nm`.

[(ii)] At the high energy side of the resonance, it is sometimes difficult to assign a meaningful halfwidth (for example due to the quadrupole peak in the 150 `nm` nanosphere spectra). Twice the half width at half maximum at the low energy side is used in such cases.

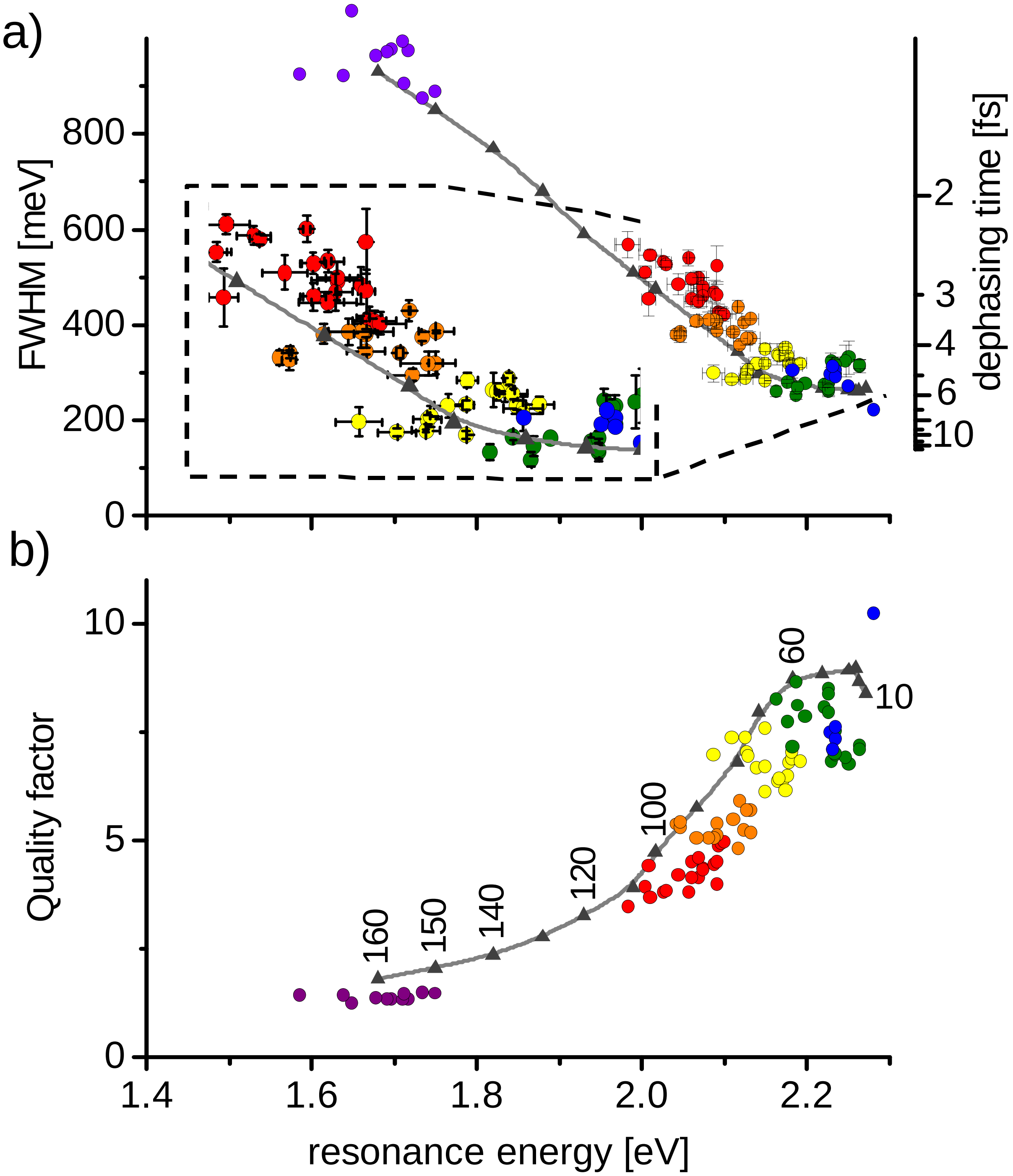

Fig. 8.7: a) FWHM and dephasing time T_2 for scattering spectra of gold nanospheres (dots). Colors indicate different nominal diameters (150, 100, 80, 60, 40, and 20 `nm`, from left to right). Close-up of the data for diameters from 20–100 `nm` shown in the inset. Solid line: Mie calculation. b) Quality factors derived for the data in a). Numbers correspond to the diameters used in the calculation.

The technical implications of the above mentioned results are as follows: For optical applications demanding a small linewidth, gold nanospheres with diameters below 60nm should be used. If visibility, i.e. a large scattering efficiency, is also important (for example for nanosensors employing the sensitivity of the particle plasmon resonance on the refractive index of the embedding medium), 60 `nm` diameter nanospheres should be used. For nonlinear applications, a high quality factor is desirable, therefore the choice will be towards smaller particles. If, however, particle heating is a problem due to light energy absorption, larger particles with higher quantum efficiency should be used. A reasonable compromise is likely to be 40 `nm` diameter gold nanospheres.

8.3 Silver nanospheres

Silver is another material yielding high quality plasmon resonances as metal nanoparticles. In theory, there should be less damping in silver compared to gold, because of the longer free-electron dephasing time of the conduction electrons and smaller interband damping. In real samples, this low damping is mainly observed under ultra-high vacuum conditions (Johnson and Christy, 1972) due to the surface reaction of silver with air (AgS_2). Due to this contamination problem, the dielectric function for silver is not as well known as for gold (see Fig. 2.2). A prediction of the dephasing time of real samples of silver nanospheres from theory is therefore not reliable.

In this section I will present experimental data on silver nanospheres, which are obtained in a similar manner to the gold nanospheres presented in the previous section. The only difference is the use of a xenon light source because of the high energy of the silver particle plasmon. Xenon lamps have a 5-10x higher light intensity output at 3 `eV` than the halogen lamps normally used. The spectrum is, however, much less smooth due to some distinct emission peaks, which demands great care in normalizing to the excitation spectrum.

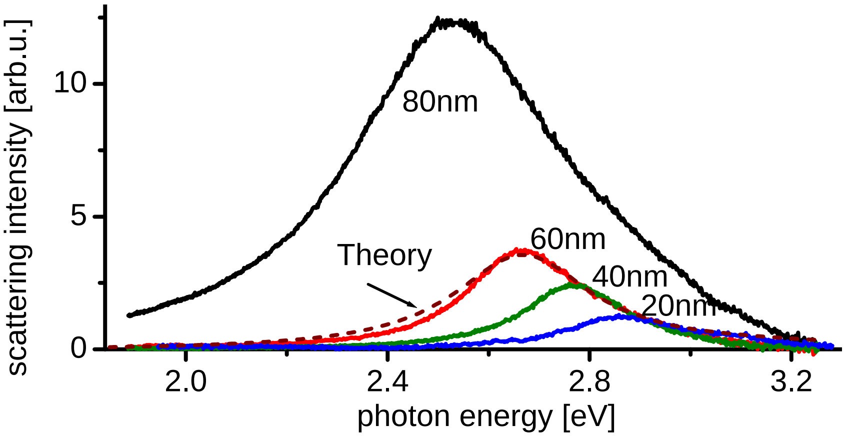

Fig. 8.8: Measured scattering spectra for silver nanospheres of different diameters (80,60,40,20 `nm`) demonstrating the red-shift, line-broadening, and stronger scattering intensity by increasing nanosphere diameter. Broken line: Mie calculation for 60 `nm` diameter.

Examples of scattering spectra for silver nanospheres of different diameters are shown in Fig. 8.8 . As for gold nanospheres one observes a red-shift of the resonance energy for increasing nanosphere diameter and at the same time an increase in linewidth. The calculated spectrum shown by the broken line agrees well with the experiment. This is not the case, however, for all other particles studied.

These deviations from theory are more apparent from the plot of linewidth versus resonance energy as described in the previous sections: see Fig. 8.9 a. Similar to the gold nanospheres, the measured data points scatter around a general trend, possibly due to facetting, charges, or surface contaminations due to local deviations in particle environment. The averages for the same nominal sizes (20–80 `nm`) are indicated by open circles.

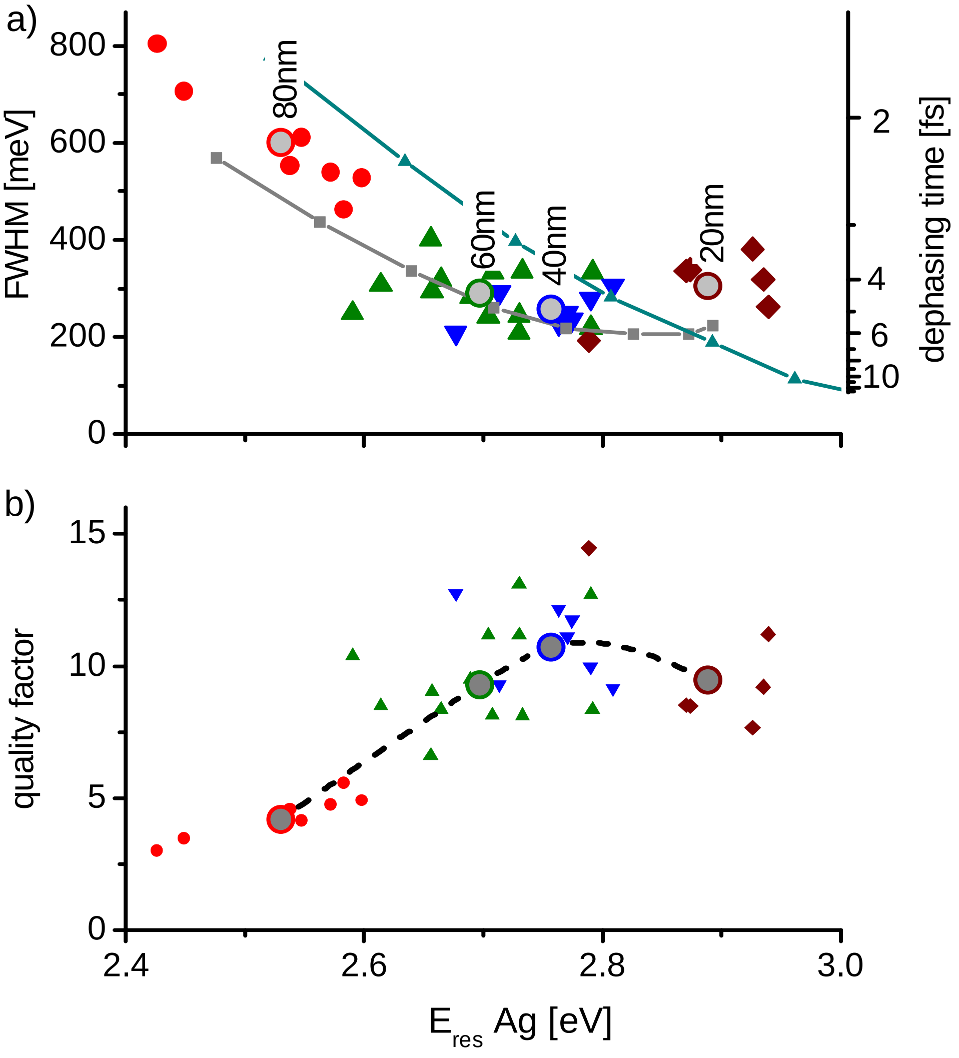

Fig. 8.9: a) Linewidth versus resonance energy for measured scattering spectra of silver nanospheres with different nominal diameters (20, 40, 60, 80 `nm`). Large open circles: averages for the corresponding nominal diameter. Lines: theoretical calculations using dielectric functions by Johnson and Christy (1972) (triangles) and Quinten and Kreibig (1996) (squares). b) same data plotted as quality factor. Averages connected by dashed line.

Generally, the resonance position shifts to lower energies for larger particles which is also observed for gold nanospheres. However, a considerable increase in particle linewidth is only observed for particles with 80 `nm` diameter. This hints to an additional damping mechanism for small silver nanospheres, for example surface scattering. It has been postulated that surface scattering should play a larger role in silver than in gold due to the larger mean-free-path of the conduction electrons (Kreibig and Vollmer, 1995). My experimental results seem to support this. Other effects, for example a larger contamination with AgS_2, could also be the cause.

As mentioned in the beginning of this section, the values for the dielectric function of silver reported in literature vary considerably(iii). Mie calculations for two sets of such values, reported by Johnson and Christy (1972) and Quinten *et al.* (1985), are shown in Fig. 8.9 . It is clear from these calculations that a reliable theoretical prediction is not possible, but the experimental trend is observed to lie inbetween those two theoretical calculations.

The dephasing time for the resonances in Fig. 8.9 a can be obtained from the scale on the right. The actual values obtained for the dephasing times are given in Tab. 8.2 . A conclusion about possible collective dephasing can not be given here, because there is only weak agreement with theory, so I do not quote plasmon lifetimes. However, the quality factor can be calculated as in the previous sections. The result is shown in Fig. 8.9 b. The average values range from 5 to 11, which is only slightly better than the values obtained for gold nanospheres.

d [nm]	20	40	60	80
T_2 [fs]	4.5	5.2	4.7	2.3

Tab. 8.2: Dephasing times T_2 of silver nanospheres with different diameters d.

In conclusion, measured values for the dephasing times in silver nanospheres are presented. The scattering among the measured values and the agreement with theory is poor. The latter is presumably due to errors in the tabulated input parameters for the calculations. Similar to gold spheres, the resonance position shifts towards the red for increasing particle size. Radiation damping increases the linewidth only for diameters above 60 nm, which could be due to additional dephasing mechanisms in small particles such as surface scattering or adsorbate damping.

For optical applications demanding the combination of a small linewidth, high quantum efficiency, and large scattering intensity, silver nanospheres with 60 nm diameter should be used.

(iii) e.g. Johnson and Christy (1972); Winsemius (1972); Weaver *et al.* (1981); Palik (1985); Quinten and Kreibig (1996); Seider (1996).

8.4 Gold nanorods

It is well known that the particle shape has a strong influence on particle plasmons. Chemically produced nanorods are an ideal system to study this influence. The advantage over lithographically produced "nanowires" is their smooth surface and monocrystallinity. Also, the production method yields very inhomogeneous ensembles with many different aspect ratios, i.e. ratio of length to width. For ensemble measurements this poses a problem; for single particle measurements, however, this is an advantage as the effect of the shape within only one sample can be easily studied . In addition, presently great interest in the optical properties of such nanorods exists because the chemical production method for nanorods is relatively new.

The experiments presented in this section shows very interesting and surprising effects, namely extremely long dephasing times and at the same time large scattering efficiencies, which not only allow to deduce fundamental properties of the plasmon dephasing process but also makes them very promising candidates for optical applications.

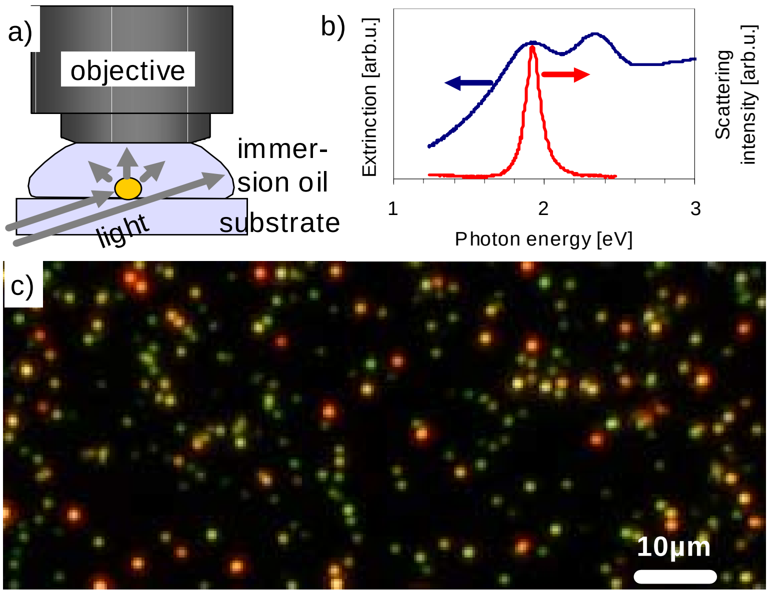

Fig. 8.10: a) Dark-field microscope setup with 100× oil immersion objective with adjustable aperture b) comparison of ensemble and single particle spectra c) true color dark-field photograph of a sample of nanorods.

The light scattering spectra of single nanorods presented in this section are obtained with basically the same configuration of the dark-field setup used to measure gold and silver nanospheres. It is further optimized by using a high N.A. oil immersion microscope objective with an adjustable aperture.

This allows the abandonment of the top cover slip which further improves the dark-field contrast and collection efficiency (Fig. 8.10 a).

An example of a true-color photograph taken with the microscope setup is shown in Fig. 8.10 c. It is quite an accurate reproduction of the intensity and contrast observable with the naked eye through the microscope eye-piece. Already from the many different colors of the nanorods in this picture it is clear that nanorods have a much larger inhomogeneous broadening in the spectral positions of their plasmon resonances than nanospheres. This is confirmed by looking at an ensemble extinction spectrum in comparison to a single particle spectrum (Fig. 8.10 b). The linewidth of the single particle spectrum is only a small fraction of the ensemble linewidth which highlights the importance of single particle spectroscopy.

Single particle spectroscopy gives another very interesting possibility: to change the polarization of the excitation light with respect to the long axis of the nanorod. Due to their very inhomogeneous shape, nanorods should exhibit a large anisotropy with respect to the polarization angle. This is confirmed by Fig. 8.11 , where two spectra are shown for the same nanorod with orthogonal polarization of the excitation light. If the polarization is parallel to the long axis, the observed resonance is strongly red-shifted, has a small linewidth and a high intensity. The short axis mode is slightly blue-shifted compared to small nanospheres, is broad, and very weak.

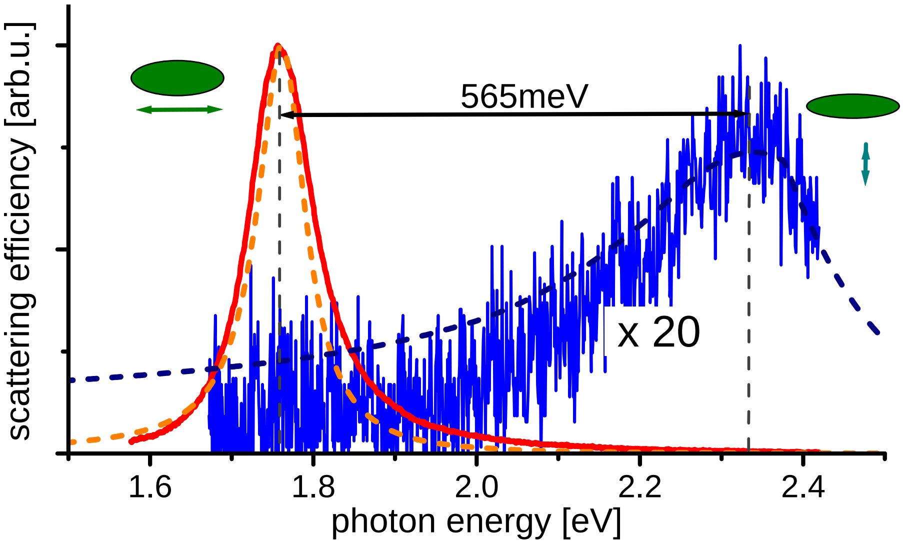

Fig. 8.11: Long axis (left) and short axis (right) plasmon modes of nanorods. Spectra recorded with the same integration time, short axis mode data multiplied by a factor of 20. Besides the peak position and linewidth for each of the modes, the energy splitting (here 565 `meV`) can be determined. Resonance energy, splitting and the intensity ratio are reproduced by a simple electrostatic calculation (dashed lines) using bulk dielectric functions. The only free parameter in the calculation is the aspect ratio (here 2.9 : 1)

Interestingly, these results are modelled by the simple electrostatic theory (Rayleigh approximation) for small spheroids presented in Sec. 4.5.2 using bulk dielectric functions. With only one free parameter (the aspect ratio), the theory fits the experimental peak position for both modes, the splitting in resonance energy, the corresponding linewidth and the relative intensities! Similar to the argument for gold nanospheres, we have to conclude from the good agreement of experiment and theory that all damping mechanisms are already included in the theory. In particular, surface scattering seems to be negligible despite the small size of my nanorods. Since no radiation damping is included in the Rayleigh approximation, we have to further conclude that radiation damping is very weak for these nanorods. Considering the small size of the nanorods, this might not be surprising at first, but it seems to contradict the strong scattering intensity observed in the microscope (Fig. 8.10 c). This apparent paradox will be resolved at the end of this section.

Before the linewidths are discussed in more detail I wish to look again at the polarization dependence. Spectra of the same nanorod for many different polarization angles of the excitation light are shown in Fig. 8.12 a. Clearly the intensity of the long-axis resonance shows a strong polarization dependence. To study this in greater detail, Fig. 8.12 b shows the intensity of this peak versus the polarization angle, which follows a sinusoidal line. This is also clearly seen in Fig. 8.12 c, where the same data is plotted in a polar diagram. The observed intensity distribution as a function of polarization angle θ follows almost perfectly the well-known dipole $\cos^2\theta$ characteristic.

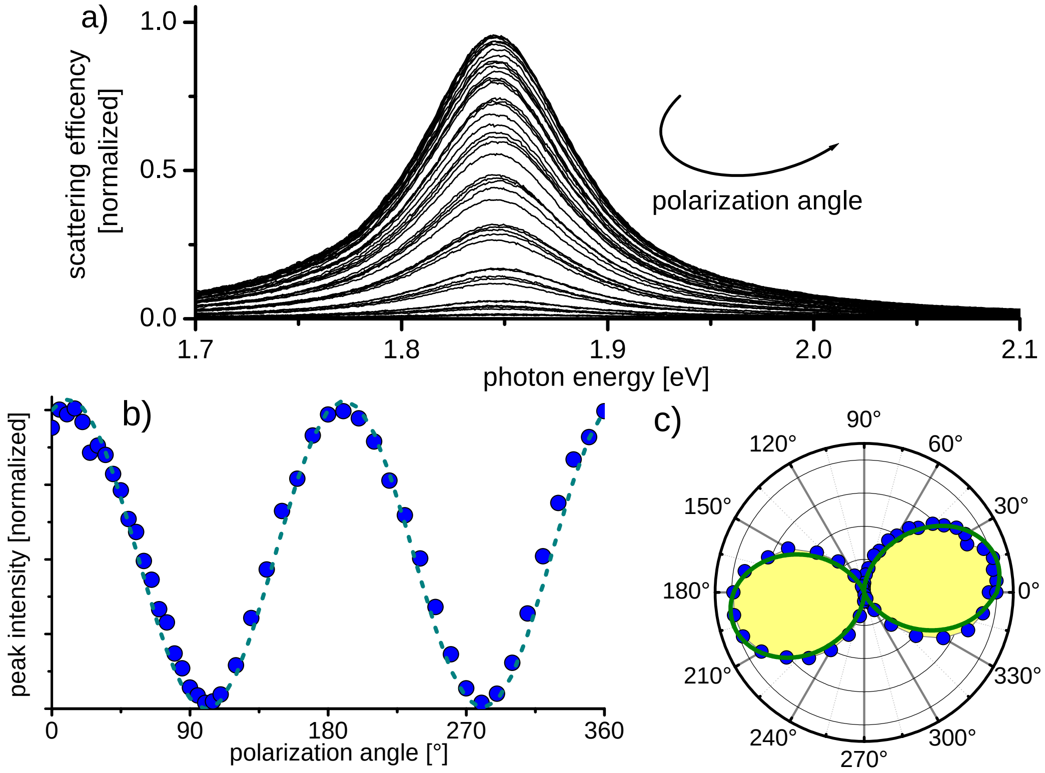

Fig. 8.12: a) Scattering spectra of a single nanorod for different angles of polarization (0-360 degrees in steps of 5 degrees). The contrast between the highest and lowest long-axis plasmon intensity is greater than 50, the short axis plasmon is not visible on this scale; b) intensity of the long-axis resonance in a) as a function of polarization angle θ. The dashed line is a fit of $\cos^2\theta$. c) same data plotted in a polar diagram.

From the above observation follows that it is possible to selectively excite one plasmon mode at a time by adjusting the polarization direction. The contrast between the orthogonal polarization directions is very high — here more than 50, and is limited because of the instrumentation (quality of the polarization filters). The polarization dependence is that of a dipole.

Let us return now to the question of linewidth and dephasing time of plasmons in nanorods. As in all previous sections on particle plasmons, I use a plot of linewidth versus resonance energy extracted from single particle scattering spectra to investigate the results more systematically. In contrast to nanospheres, where the resonance position is a function of particle diameter, the resonance of nanorods is a function of aspect ratio. Their volume will of course also have an influence, but the actual nanorods under investigation are so small that this volume dependence is negligible compared to the very strong shape influence. I concentrate in the following on the long axis plasmon as it is by far the stronger mode (cf. Fig. 8.11).

The resulting graph is shown in Fig. 8.13 a. A sharp decrease in linewidth for increasing red-shift of the long-axis resonance (hence increasing aspect ratio) is observed. The linewidth decreases from values above 220 meV down to 75 meV. Again, theoretical calculations (solid lines) using the simple electrostatic approximation (cf. Sec. 4.5.2) are in excellent agreement with the observations, thus confirming the conclusions drawn above about the absence of additional dephasing mechanisms. The theory allows to calculate the back calculation of the aspect ratio of a specific nanorod from its resonance frequency (Eqn. 4.17). The resonance positions shown here correspond to aspect ratios smaller than 4:1.

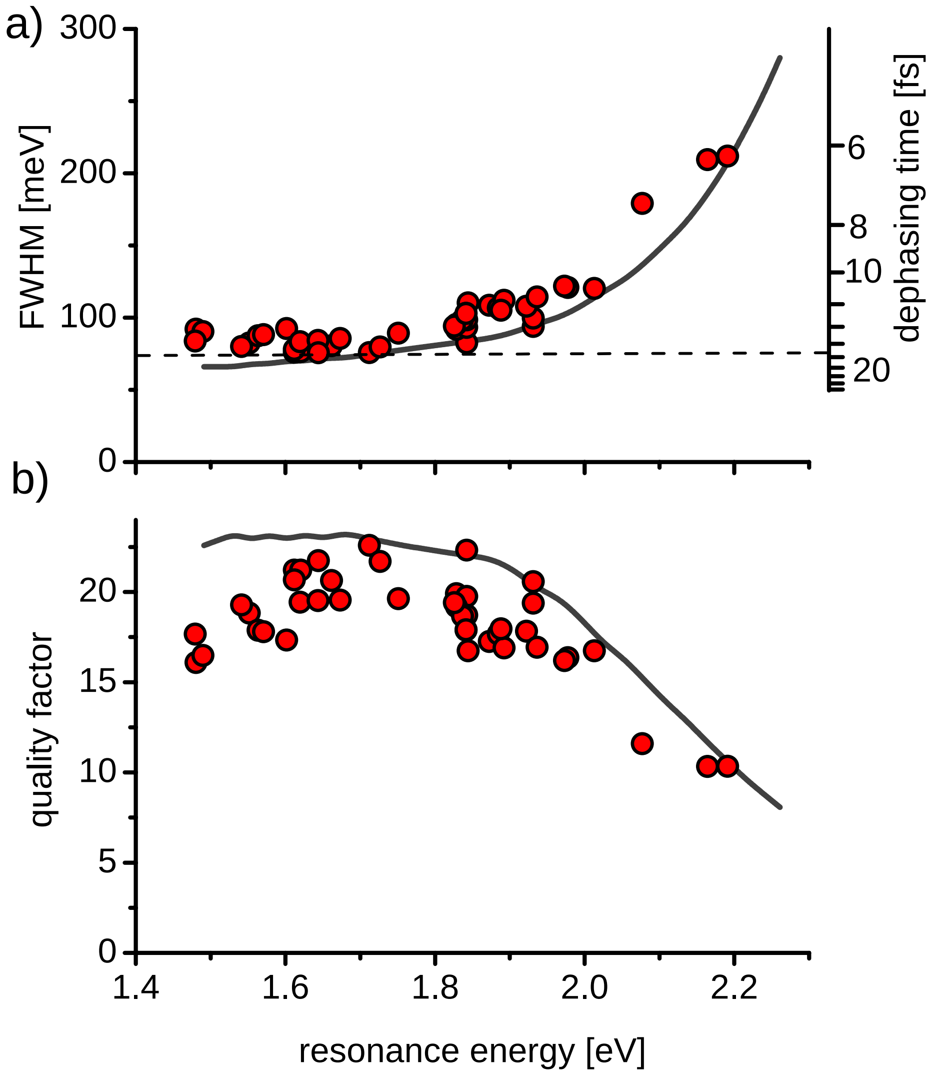

Fig. 8.13: a) linewidth versus resonance energy for the long-axis plasmon of different nanorods (dots) and calculated by a simple electrostatic model (line). Dephasing time is indicated by the scale on the right hand side; 'true' plasmon dephasing time as marked by the dashed horizontal line (see Sec. 8.6.4); b) quality factors calculated from linewidths data in a) with maximum values around 1.7 eV.

The linewidths observed (75-220 meV) are extremely small compared to the smallest value observed for gold nanospheres (270 meV) or even silver nanospheres (240 meV). Since it is known that radiation damping is already negligible in the smallest gold nanospheres studied here, the reduction in linewidth in nanorods cannot be due to further decreased nonradiative damping. This is confirmed by the fact that the observed linewidths are well explained by the electrostatic theory which neglects radiation effects. I conclude therefore:

1. Nonradiative damping is reduced in nanorods with increasing aspect ratio.
2. Radiative damping is small compared to nonradiative contributions.

The reduction in nonradiative damping can be understood by the model presented in Sec. 4.4 . The main nonradiative damping mechanism are intra- and interband electron-hole excitations. Interband excitations require a threshold energy given by the energy spacing between the d-band and Fermi-energy. Decreasing the plasmon resonance energy below this threshold energy (1.8 `eV` in gold) suppresses inter-band damping completely. I conclude that interband damping is suppressed in gold nanorods above a certain aspect ratio.

Another observation supporting the conclusion about suppressed interband damping in gold nanorods is their strong scattering efficiency as compared to nanospheres of the same volume. Already from the picture in Fig. 8.10 it is obvious that the strongly red-shifted particles (orange and red dots) are much brighter than the round particles (green dots). Actually, it is surprising that nanorods are visible by the naked eye in a dark-field microscope as nanospheres of 20 `nm` diameter are barely observable with the help of a nitrogen cooled CCD camera. This is quantitatively confirmed by the spectra in Fig. 8.14 , where a typical nanorod spectrum is quantitatively compared to spectrum of a nanosphere with 60 `nm` diameter.

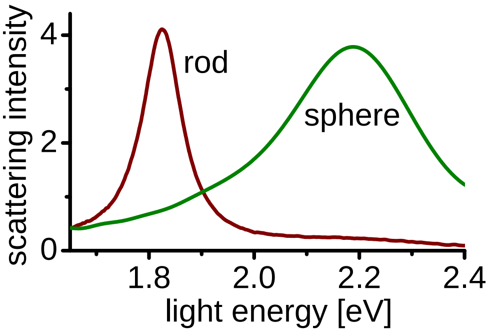

Fig. 8.14: Scattering intensity of a nanorod and a 60 `nm` nanosphere under identical conditions.

An explanation for the apparently high scattering efficiency of nanorods is the fact that a reduced nonradiative damping leads automatically to an increased radiative quantum yield η. The radiative quantum yield η is defined by:

$$\eta = \frac{\tau_{\text{rad}}^{-1}}{\tau_{\text{rad}}^{-1} + \tau_{\text{nonrad}}^{-1}} \tag{8.1}$$

Because η is simultaneously related to the cross-sections at the resonance frequency E_{res} by $\eta = C_{\text{sca}}/C_{\text{ext}}$, an increased quantum yield will automatically increase the observed scattering intensity — in agreement with the experimental findings mentioned above. Note that the observed scattering intensity ($\propto C_{\text{sca}}$) increases even more if the extinction cross-section C_{ext} is increased, e.g. by increasing the particles polarizability. For nanorods, the latter effect also contributes significantly.

If we look at the quality or field enhancement factor Q presented in Fig. 8.13 b, we see an increase in Q as the resonance energy decreases until a maximum value of about 23 is obtained around 1.7 `eV`. Further reduction of the resonance energy decreases the quality factor. The maximum value of 23 is very large compared to nanospheres (11), so nanorods should exhibit large local field enhancement if excited at the resonance frequency. Note that it reaches the values obtained by theory (line). These calculations neglect radiation damping as well as all nonradiative damping processes other than the bulk single electron scattering (e.g. surface scattering and collective dephasing processes are neglected). Since these further dephasing mechanisms would reduce the quality factor, the calculated line gives the theoretical limit for the quality factor of gold nanoparticles.

To summarize the findings in this section: nanorods show a large scattering efficiency at the plasmon resonance combined with extremely small linewidth, i.e. long plasmon dephasing times. In fact, the longest dephasing times measured here (18 `fs`) are, to the best of my knowledge, the longest reported for gold nanoparticles to date. The reason for this long dephasing time is reduced nonradiative damping by suppression of interband transitions, which reduces the linewidth and increases the radiative quantum yield. Comparison with electrostatic theory shows that the plasmon damping in nanorods is solely due to single electron relaxation. This single electron relaxation can be described as electron-hole-pair excitation. In particular, radiation damping, surface scattering, and collective dephasing are negligible. This means that the observed quality factors of up to 23 reach the theoretical limit given by the single electron relaxation.

The high radiative quantum yield, large scattering efficiency, small linewidth and large local field enhancement achievable with nanorods is an ideal combination of properties for most optical applications relying on particle plasmons.

One example is nonlinear-optics, where effects such as second harmonic generation (SHG) or surface enhanced Raman scattering (SERS) are increased by taking advantage of the local field-enhancement around the particles. The large local field-enhancement factor in nanorods is obviously helpful — but the high radiative quantum yield is also very important, because the efficiency of a nonlinear effect is ultimately limited by sample heating due to light absorption and because very intense light fields are necessary to get a reasonable non-linear response. Since a high radiative quantum yield means a large fraction of light energy is re-emitted, heating of the nanorods is reduced.

Another example is the application of particle plasmons as nanosensors by employing the high sensitivity of the resonance energy on the refractive index of the surrounding medium (Chap. 9). A shift in resonance energy is more easily observed for narrower lines. At the same time, a high radiative quantum yield and scattering efficiency is necessary to obtain enough scattering signal from the nanoparticle under investigation.

8.5 Particle pairs

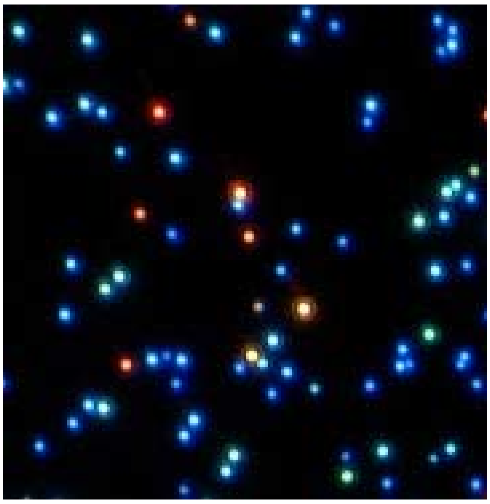

Fig. 8.15: Real color photograph of silver nanospheres (blue). Particle pairs are easily identified by their distinctly different color (orange) compared to single particles (blue). Note that particle pairs are not optically resolved as two dots because of the diffraction limit.

Before the experimental results of the previous sections are compared, I briefly discuss the electrodynamic coupling of close-lying particles. As I have mentioned before, the random distribution of nanospheres by simply spin-casting a solution of nanoparticles on the substrate leads occasionally to the formation of particle pairs. If the distance between the particles is on the order of the particle diameter, the plasmons couple electrodynamically like coupled dipoles. The coupling strength strongly depends on the separation distance. It leads to the formation of coupled plasmon modes as for any coupled oscillators. Thus there are in principle four modes ($\uparrow\uparrow$ and $\uparrow\downarrow$) perpendicular and parallel to the axis connecting the particles. Only the in-phase modes ($\uparrow\uparrow$) can be excited with light, because the overall dimension of the particle pair is still much smaller than the light wavelength. The light field and thus the electron displacement is therefore in the same direction for both particles. The two modes parallel ($\rightarrow\rightarrow$) and perpendicular ($\uparrow\uparrow$) to the connecting axis, which I will term[iv] long-axis and short-axis mode, respectively, can be excited by light. They have different resonance frequencies, with the long axis mode being at lower energies (Bohren and Huffman, 1982; Kreibig and Vollmer, 1995). This effect is observed in the real color photograph shown in Fig. 8.15 : particle pairs show distinctly different colors (green, orange) from single particles (blue). Note that coupled particle pairs are not resolved optically as two dots due to the diffraction limit. The color and the polarization dependence are the only means to identify them optically.

In Fig. 8.16 , this effect is shown more quantitatively. By exciting with polarized light, the two plasmon modes can be addressed separately. The splitting of the two resonance modes, which is easily observed in such experiments, is determined by the particle separation. Simple electrostatic theory assuming interacting point dipoles reproduce the splitting observed in Fig. 8.16 a for a particle separation of $4.8 \pm 0.1\,\mathtt{nm}$.

The plasmon resonance splitting can, in principle, be used as a very sensitive way to determine interparticle distances optically with Ångström resolution. Also, more complicated structures, produced for example by DNA assisted self-assembly (Mirkin *et al.*, 1996; Alivisatos *et al.*, 1996), could be investigated.

[iv] Analogous to the modes in nanorods

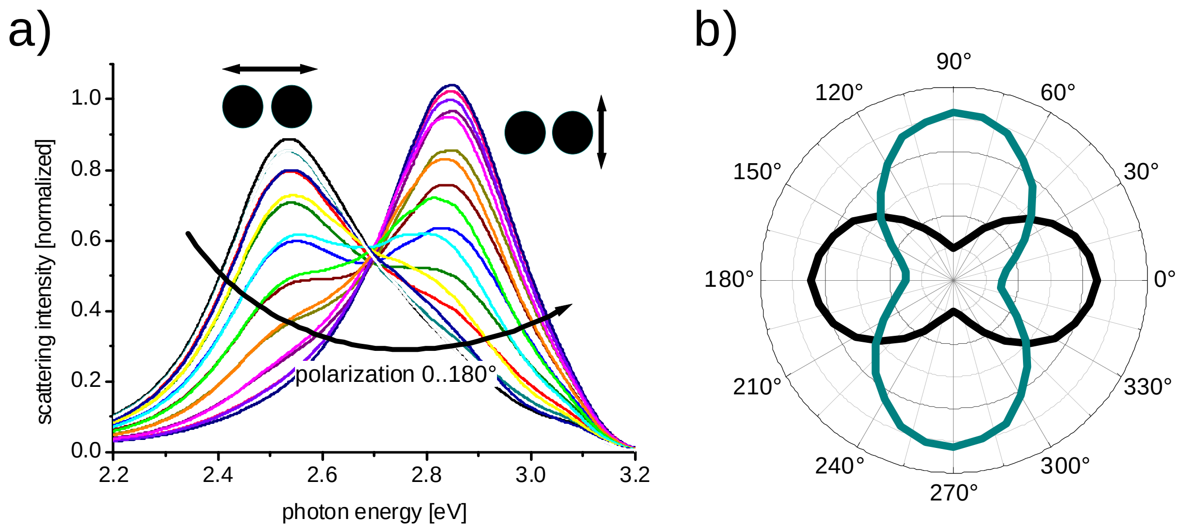

Fig. 8.16: a) Spectra of the same individual pair of silver nanospheres with 60 nm diameter taken with polarized light for polarization angles between 0°and 180°in 10°steps. The two peaks correspond to the long-axis (left) and short-axis (right) plasmon modes, respectively. b) Intensity at the long-axis (black) and short-axis (green) resonance frequencies shown in a polar diagram. Both modes show the expected dipolar angle dependency.

8.6 Discussion

The dephasing time for plasmons in metal nanoparticles has been the subject of intense research efforts and is probably the most important fundamental open question regarding particle plasmons (Sec. 4.6). Nevertheless, the reported values strongly disagree. I summarize therefore my results in Sec. 8.6.1 . Comparing these dephasing times allows to deduce further details of the dephasing process (Sec. 8.6.2). In fact, it allows to estimate the contribution of all relevant dephasing processes quantitatively (Sec. 8.6.3).

8.6.1 Summary of dephasing times

The particle plasmon dephasing times determined for spherical gold and silver particles are summarized in Tab. 8.3 . Generally, a reduction in dephasing time is observed with increasing particle diameter. These values give reliable answers to the long debated question on the amount of damping in spherical nanoparticles as function of their size (cf. Sec. 4.6).

The difference in plasmon linewidth between gold and silver nanospheres are not dramatic. This finding has two important technological implications:
1. There is *not* a large advantage to using silver instead of gold if small linewidth or long dephasing times are needed.
2. it is possible to find a particle material (gold, silver or an alloy of the two) for any desired resonance energy over the entire visible spectral region with reasonably small linewidths and large quality factor (see Fig. 8.17).

	d [nm]	E_{res} [eV]	λ_{res} [nm]	Γ [meV]	$\Delta\lambda$ [nm]	T_2 [fs]	$\tau \equiv T_1$ [fs]	Q [–]
Au	150	1.67	742	626	289	2.1	1.1	2.7
	100	2.06	601	484	143	2.7	1.4	4.3
	80	2.09	591	395	113	3.3	1.6	5.3
	60	2.15	575	318	86	4.1	2.1	6.8
	40	2.22	557	294	74	4.5	2.3	7.6
	20	2.23	555	289	72	4.5	2.3	7.7
Ag	80	2.53	489	601	118	2.3	1.2 (?)	4.2
	60	2.70	459	290	50	4.7	2.4 (?)	9.3
	40	2.76	449	257	42	5.2	2.6 (?)	10.7
	20	2.89	429	305	45	4.5	2.3 (?)	9.5

Tab. 8.3: Summary of the plasmon properties for gold and silver nanospheres determined in this work (d: particle diameter, E_{res}: resonance energy, λ_{res}: resonance wavelength, Γ: full linewidth at half maximum (FWHM), $\Delta\lambda$: linewidth in `nm`, T_2: dephasing time, T_1: lifetime, Q: quality factor). All particles are embedded in a medium with refractive index $n = 1.5$. Since the uncertainty in the theory for silver does not allow to exclude collective elastic dephasing mechanism, the calculation of T_1 is not possible. The values are therefore marked with a (?).

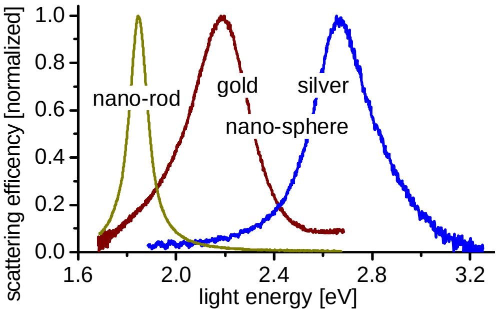

Fig. 8.17: Comparison of resonances in gold and silver nanoparticles.

The plasmon linewidth, dephasing times and quality factors for gold nanorods and -disks are not as easily presented in a table because of the unknown particle dimensions. Instead, the usual plots of linewidth/dephasing time and quality factor as functions of resonance energy are shown in Fig. 8.18 . However, it should be emphasized that the nanodisk values are not directly comparable to the others because they are determined in a different environment (ITO/air instead of glass/oil). This causes an unknown shift in resonance position and possibly also in linewidth. Nevertheless, it is observed that nanodisk dephasing times are shorter than those of nanorods due to their much larger volume. Both particle classes cover a large range of particle plasmon dephasing times T_2: 6.2–18 `fs` for nanorods and 2.1–7.3 `fs` for nanodisks.

The strong shape and size dependence of the particle plasmon dephasing time explains the variety of values reported in literature.

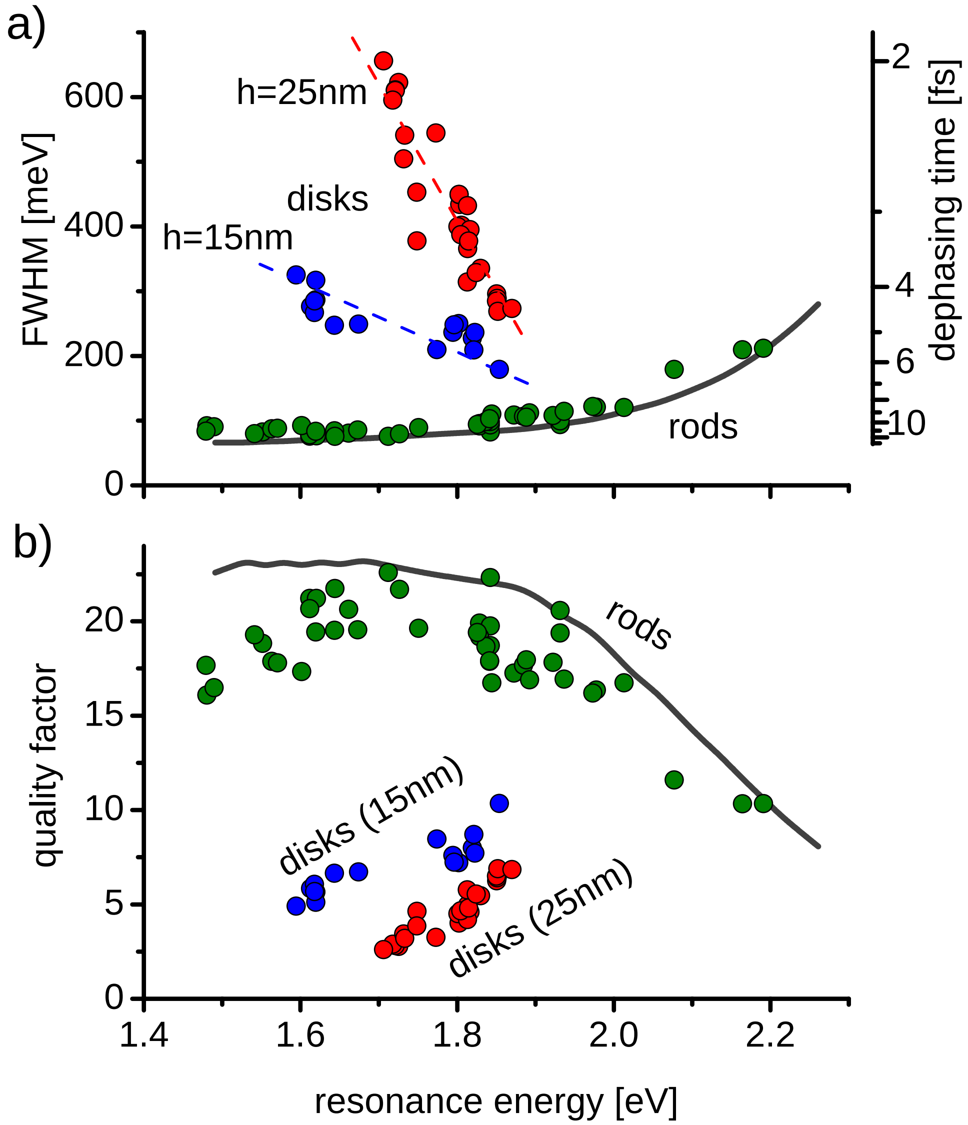

Fig. 8.18: Summary of all linewidth, dephasing time (a) and quality factor (b) data for gold nanorods and -disks. The disk values correspond to disks with heights of $h = 15\,\texttt{nm}$ and $h = 25\,\texttt{nm}$

8.6.2 Particle plasmon damping mechanisms in gold (qualitative)

A lot can be learned about the plasmon dephasing mechanisms by comparing gold nanospheres and nanorods (assuming that the dephasing mechanisms are similar). For this, the data presented in the corresponding sections are plotted together in Fig. 8.19 . The most striking fact is that nanospheres and -rods show the opposite behaviour with respect to linewidth. Whereas the linewidth of nanospheres increases for more red-shifted resonances, it decreases for nanorods. The almost perfect agreement with the results of theoretical calculations is also noteworthy. In the case of the theory for nanospheres, this is a complete electrodynamical calculation (Mie theory) *including* radiation effects with the particle diameter as parameter, while in the case of the theory for nanorods it is a simple electrostatic approximation (Rayleigh-theory) *neglecting* radiation effects with the aspect ratio as parameter. The bulk dielectric function for gold (Johnson and Christy, 1972) is used in both cases. No further parameters enter the calculation.

Only single electron relaxation enters the bulk dielectric function of gold, i.e. inter- and intraband transitions. From the agreement between theory and experiment, I conclude for the samples under investigation (some of these conclusions have already been mentioned in the previous sections):

(I) Only interband, intraband and radiation damping contribute significantly to particle plasmon dephasing.

(II) Radiation damping is small compared to nonradiative damping for nanorods.

Conclusion I rules out in particular significant surface effects and/or a collective plasmon dephasing. Of course, this is only true for particle sizes studied here. Surface effects will have a dominant effect in very small particles with dimensions smaller than the mean-free-path (MFP) of the conduction electrons, i.e. gold particles smaller than about 20 nm. Conclusion II is reasonable here also because of the small volume of the nanorods investigated, which are always smaller than nanospheres with 40 nm diameter, and typically more similar to nanospheres with 30 nm diameter.

The observed decrease in linewidth of nanorods with increasing red-shift of the plasmon resonance is explained by the following conclusion:

(III) Interband damping is suppressed at lower resonance energies.

Conclusion III also explains (at least partly) the surprisingly large scattering efficiency of nanorods (despite their small radiation damping) by an increased radiative quantum efficiency η, which follows automatically from the suppression of interband damping. In other words:

(IV) From III follows an increasing radiative quantum efficiency for nanorods with increasing aspect ratio.

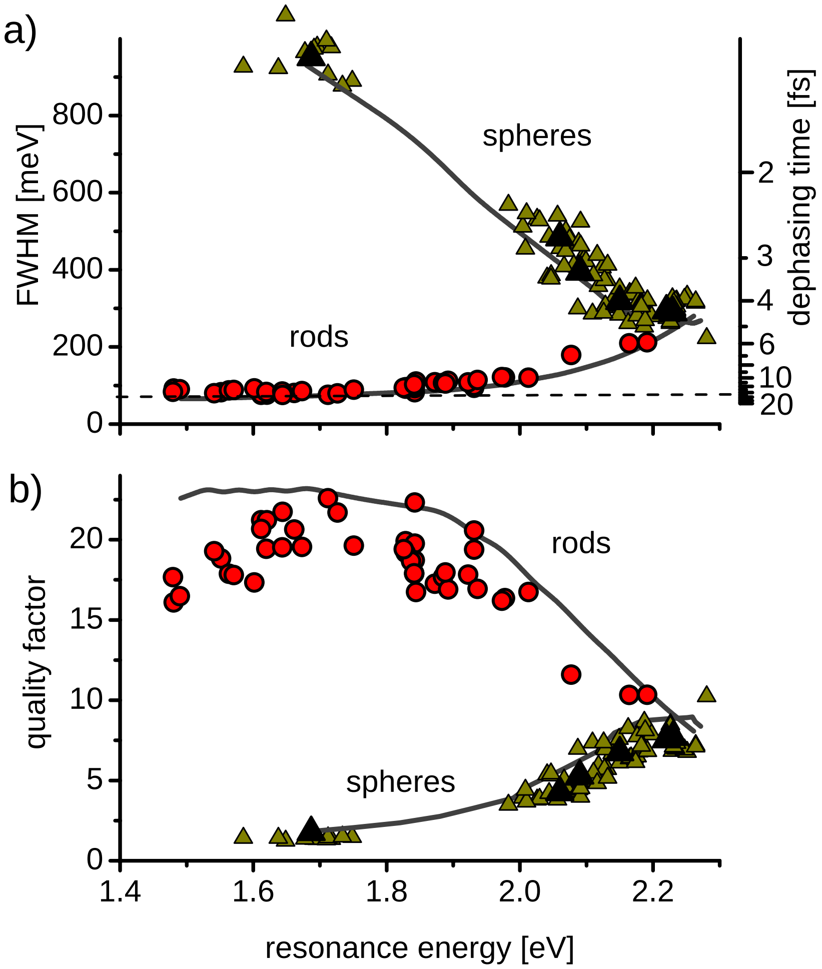

Fig. 8.19: a) Homogeneous linewidth Γ of plasmon resonances in nanorods (dots) and nanospheres (triangles) as function of their resonance energy E_{res}. The nanosphere diameter and the nanorod aspect ratio increase from right to left. The linewidth Γ directly gives the dephasing time $T_2 = 2\hbar/\Gamma$ (scale on the right). Line: theoretical calculation. Dashed horizontal line: 'true' plasmon dephasing time in gold.
b) same data as above plotted as quality factor $Q = E_{\mathrm{res}}/\Gamma$.

Finally, the strong increase of the plasmon linewidth for gold nanospheres with increasing diameter must be explained. Since we know from (III) that nonradiative damping should *decrease* on red-shifting of the resonance energy, we have to assume:

(V) Radiation damping increases dramatically with particle size.

Apparently, effect (V) far outweighs effect (III) for gold nanospheres, whereas it does not come into effect for the nanorods due to their relatively small volume.

8.6.3 Particle plasmon damping mechanism in gold (quantitative)

Conclusions I-IV stated above provide a tool to separate the contributions of the three relevant dephasing mechanism in gold nanoparticles quantitatively. From the Drude-Sommerfeld theory for metals, we know that the intraband contribution to damping (Γ_{intra}) is constant over the frequency range considered here. From I–III and Fig. 8.19 we have therefore[(v)]

$$\Gamma_{\text{intra}} = 77\,\texttt{meV} \tag{8.2}$$

We just have to subtract this intraband contribution from the measured dephasing times in nanorods to obtain the interband contribution (Γ_{inter}). The resulting data points are well described by the purely empirical relation:

$$\Gamma_{\text{inter}}/\,\texttt{meV} = e^{(E_{\text{res}}/\,\texttt{eV}-1.334)/0.171} \tag{8.3}$$

Again, this dephasing rate should be independent of particle size or shape (except for their influence on the resonance energy, of course) as it is a property of the individual electrons. Combining Eqn. 8.2 and Eqn. 8.3 , yields:

$$\Gamma_{\text{nonrad}}/\,\texttt{meV} = 77 + e^{(E_{\text{res}}/\,\texttt{eV}-1.334)/0.171} \tag{8.4}$$

We can use this equation to calculate the non-radiative dephasing rate for each of the measured data points for the nanospheres in Fig. 8.19 . The radiative dephasing rate is then the remaining portion of the measured total rate. The result is shown in Fig. 8.20 . The resonance energy has been converted to nanosphere diameter using Eqn. 4.16 obtained from Mie theory (Sec. 4.5.4) for convenience:

$$d/\,\texttt{nm} = 215\sqrt{2.262 - E_{\text{res}}/\,\texttt{eV}} \quad (d < 150\,\texttt{nm}) \tag{8.5}$$

It is found from Fig. 8.20 that for particle diameters d up to 100 nm the radiative dephasing rate is well described by the empirical d^3 law:

$$\Gamma_{\text{rad}}/\,\texttt{meV} = (d/14\,\texttt{nm})^3 \quad (20\,\texttt{nm} < d < 100\,\texttt{nm}) \tag{8.6}$$

This dependence of the radiative dephasing rate on the *volume* of the particle was a result already hinted by the investigation of nanodisks of different height in Sec. 8.1 [(vi)]. The slightly smaller dephasing rate of 150 nm spheres compared to the one predicted by this equation is due to the influence of the quadrupole plasmon mode. From the sum-rule (Eqn. 4.8) it is clear that this leads to a reduction of the strength of the dipolar plasmon mode and thus its the radiative damping rate.

The empirical equations 8.2-8.6, derived almost entirely from experimental data, allow to calculate the contributions of any of the relevant dephasing mechanisms for a given gold particle. I give an example for the powerful tool these equations provide by calculating the

---

(v) In this section, dephasing rates are given in units of energy to facilitate comparison with experimental data. The more familiar value in terms of inverse time is simply obtained by $T^{-1} = \Gamma/2\hbar$

(vi) This result follows also from complicated considerations involving the concept of radiation reaction force, cf. for example the book by Jackson (1975), combining equations 17.3 and 17.61 and using $e \propto V$ and $m \propto V$.

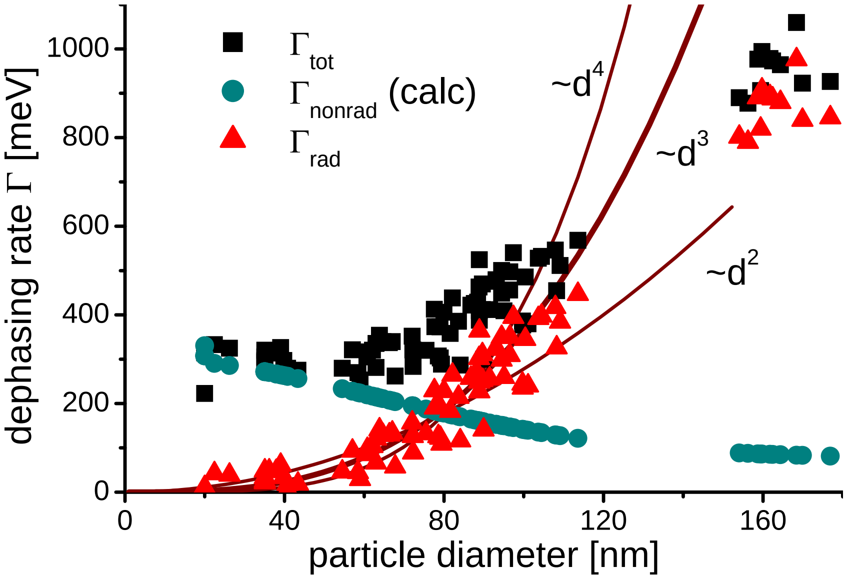

Fig. 8.20: Dephasing rates in gold nanospheres as function of diameter. Γ_{tot}: measured, Γ_{nonrad}: calculated by Eqn. 8.4 , Γ_{rad}: calculated by subtracting the two. Particle diameter is inferred from resonance position by Eqn. 8.5 .

radiative quantum yield η for spherical gold nanoparticles as function of particle diameter. It is given simply by:

$$\eta = \Gamma_{\mathrm{rad}}/\Gamma_{\mathrm{tot}} = \Gamma_{\mathrm{rad}}/(\Gamma_{\mathrm{rad}} + \Gamma_{\mathrm{nonrad}}) \tag{8.7}$$

The result is shown in Fig. 8.21 . The dot-dashed line is calculated using the empirical relations Eqn. 8.4 and 8.6. The large circles are derived from measured data for Γ_{tot} and Eqn. 8.4 , i.e. without Eqn. 8.6 . These are compared to entirely theoretical calculations using Mie theory (dashed line) with no free parameters and bulk values for gold. For this I used the relation:

$$\eta \approx \left. \frac{C_{\mathrm{sca}}}{C_{\mathrm{ext}}} \right|_{E_{\mathrm{res}}} \tag{8.8}$$

Both theory and experimental data shows a sharp increase of radiative quantum yield with increasing particle diameter. Starting from a few percent for 20 nm particles it increases to about 80-90% for particle sizes between 100 nm and 150 nm. Very good agreement of theory and experiment is observed. This is not at all trivial, as the two curves are derived by quite different concepts, namely Eqn. 8.7 and Eqn. 8.8 . In the latter, the different magnitudes of scattering and extinction cross-sections at the resonance frequency is used to determine η, in the former case dephasing rates are calculated from *linewidths.*

8.6.4 The ‘true’ plasmon dephasing time

After this important discussion of the dephasing mechanisms, I come back to the real meaning of the concept of ‘particle plasmon dephasing time’. We have seen in Sec. 8.6.1 that there is no universal particle plasmon dephasing time, if the plasmon is regarded as the origin of the observed resonance.

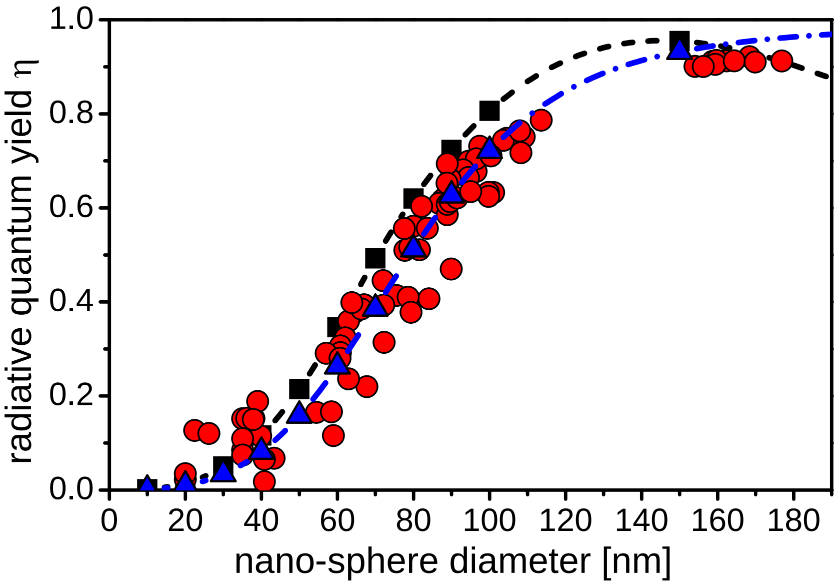

Fig. 8.21: Radiative quantum yield as a function of diameter for gold nanospheres. Dashed line: Mie theoretical results taking $\eta = C_{\text{sca}}/C_{\text{ext}}|\,E_{\text{res}}$. Triangles/dot-dashed line: calculation using the empirical equations 8.2-8.6. dots: experimental results (Γ_{tot}) combined with Eqn. 8.4 .

We may, however, define the particle plasmon differently. Up to now, the observed resonance has been *identified* with the plasmon. In a more fundamental view, the observed resonance is in fact a coupled ['true particle plasmon']-[interband-exciton]-[photon] quasi-particle(vii). The 'true particle plasmon' is a pure oscillation of quasi-free-electrons in the conduction band without interaction with interband excitations or propagating electromagnetic fields (photons). This pure oscillation can be observed experimentally only in case of the absence of any nearby interband transitions *and* the absence of radiation damping.

This 'true particle plasmon' resonance is realized in small nanorods with resonance frequencies below the interband transition threshold. At these resonance energies and particle dimensions, interband damping is suppressed and radiation damping negligible (Sec. 8.4). The limiting value of the dephasing time in nanorods shown by the horizontal lines in Fig. 8.13 a and Fig. 8.19 a is therefore the 'true' particle plasmon dephasing time $T_2^{\text{true}} = 18\,\texttt{fs}$.

In the Drude-Sommerfeld model, the true plasmon dephasing time is related to the free-electron relaxation time by:

$$T_2^{\text{true}}/2 = \tau_{\text{Drude}} \tag{8.9}$$

Calculating the free-electron relaxation time from DC values, a much larger value is obtained (Kopitzki, 1993): $\tau_{\text{Drude}} = \sigma m^*/ne^2 = 29\,\texttt{fs}$. It is, however, well known (Foiles, 1985) that the free-electron relaxation times decrease for increasing oscillation frequency. Values of 4-22 `fs` are reported by Foiles (1985) for gold in the infrared spectral region, which is in fair agreement with the value measured here. Johnson and Christy (1972) give 9.3 `fs` for the free-electron relaxation time, which is in excellent agreement with the true particle plasmon dephasing time divided by two.

(vii) Similar to the distinction between surface plasmons and surface plasmon polaritons.

8.7 Summary

The method of single particle scattering spectroscopy by dark-field microscopy has been applied for the first time to determine the amount and the mechanism of particle plasmons damping. Experiments on ordered arrays of nanodisks have established the reliability of the method. Subsequent investigations have determined the dephasing times of gold and silver nanospheres and gold nanorods. This is the first systematic and conclusive experimental study of particle plasmon dephasing. It answers the long debated question of the amount of plasmon damping in gold nanoparticles. Good agreement with calculations using the bulk dielectric function for gold shows that collective dephasing and surface effects contribute negligibly to the overall damping — only radiation damping and single electron scattering contribute significantly. The local field enhancement factors determined for my samples of gold and silver nanospheres show no considerable advantage of silver over gold despite the theoretical predictions. The reason for the unexpectedly large damping in silver nanospheres remains unclear. Probably surface scattering or contamination by surface reactions leads to additional damping. Nanorods are found to be almost ideal for optical applications. They combine small linewidths and large local field enhancement factors with relatively large radiative quantum yields and strong light-scattering. Comparison with theory shows that interband damping is suppressed in nanorods with sufficiently large aspect ratios and radiation damping is negligible. This allows qualitative and quantitative deduction of the relative contributions of radiation, inter- and intraband damping in gold nanoparticles. Furthermore, it allows to determine the 'true' plasmon dephasing time in the sense of a pure plasmon oscillation without coupling to other excitations (interband) or photons.

In addition to plasmons in individual particles, the formation of coupled plasmon modes in close-lying particles has been observed. The splitting between the plasmon modes parallel and perpendicular to the connecting axis allows to determine the particle separation. By controlling the polarization of the exciting light, both modes can be addressed separately.

Finally, it should be mentioned that the strong colors of metal nanoparticles due to their plasmon resonances can be tuned over the entire visible spectral range by choosing the appropriate particle material, shape and size. This is demonstrated by the true-color photograph on the cover.

Of course the findings presented in this chapter can be extended to other classes of metal nanostructures. Also, the influence of many parameters such as particle charges, surface treatments, temperature and static electric or magnetic fields have not been investigated. Besides these interesting questions regarding intrinsic particle properties, the application of particle plasmons can also be exploited. In particular, the method of single particle scattering spectroscopy suggests employing the strong light scattering efficiency of noble metal nanoparticles at their plasmon resonance. In the following two chapters, initial experiments are shown to demonstrate the potential for optical applications. First, the plasmon is used *passively* as a *sensor* for its dielectric environment (Chap. 9). In Chap. 10 , plasmon resonances are then *actively* controlled in order to show their potential as electrically controlled light scatterers.

9. NANOSENSOR APPLICATIONS

Among the most important biochemical challenges today are the fast and sensitive analysis of specific nucleic acid sequences (DNA-chip, e.g. Heller *et al.*, 1997) In biology, sensors inside of single living cells are desirable (Clark *et al.*, 1999). Optically detecting chemical or biochemical substances or reactions optically has many advantages over other techniques such as radio-isotope labelling. The most important advantage is the instantaneous response and its potential simplicity. I will discuss now how particle plasmon based sensors can be employed to such biological or biochemical challenges.

The particle plasmon resonance frequency is sensitive to the refractive index of the surrounding medium (e.g. Underwood and Mulvaney, 1994). For most of the experiments shown so far, problems arising from this effect have been avoided by ensuring a homogeneous particle environment with a refractive index of $n = 1.5$. The sensitivity on the surrounding medium can also be employed to *measure* its refractive index — suggested for example by Klar *et al.* (1998).

In my opinion, one of the biggest advantage of particle plasmon based nanosensors over other optical sensors is the fact that they give information about the *local* dielectric environment. This extreme locality is demonstrated in Fig. 9.1. To the best of my knowledge, none of the applications of particle plasmons as sensors shown up to now has made use of this locality, due to the lack of single particle spectroscopic methods. I will show that the single particle scattering spectroscopy developed in this work can be employed to achieve this local optical sensing on a nanometer size scale. First, I

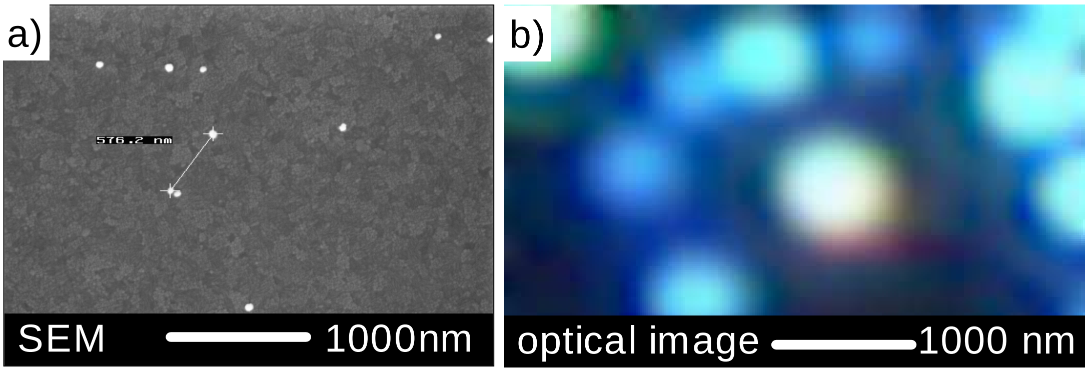

Fig. 9.1: a) Scanning electron microscopy (SEM) image of metal nanoparticles and b) diffraction limited optical image of a similar sample obtained with a dark-field microscope. Both images are shown with the same magnification. Note the extremely small size of the particles compared to their optical appearance. The sensing volume depends on this real size not on the apparent optical dimension. Therefore optical information of processes occurring on length-scales much smaller than the diffraction limit can be obtained.

demonstrate the applicability of the method to measuring particles partially exposed to liquids. Then, I show the ability to detect local concentrations, binding events and chemical reactions.

9.1 Measurements in liquids

The possibility of measuring the spectra of single particles partially immersed in liquids has been recognized early on in this work. The particles have to be supported by a glass substrate, but most of their surface is exposed to the medium covering the substrate. This can be air or various kinds of liquids. A small drop of such a liquid added to the space between sample and microscope objective is enough to cover the sample (see Fig. 9.2 center). The first demonstration of this principle on a single particle level was the observation of the plasmon resonance shift induced by adding water or oil to gold nanodisks previously exposed to air (Fig. 9.2 , left and right).

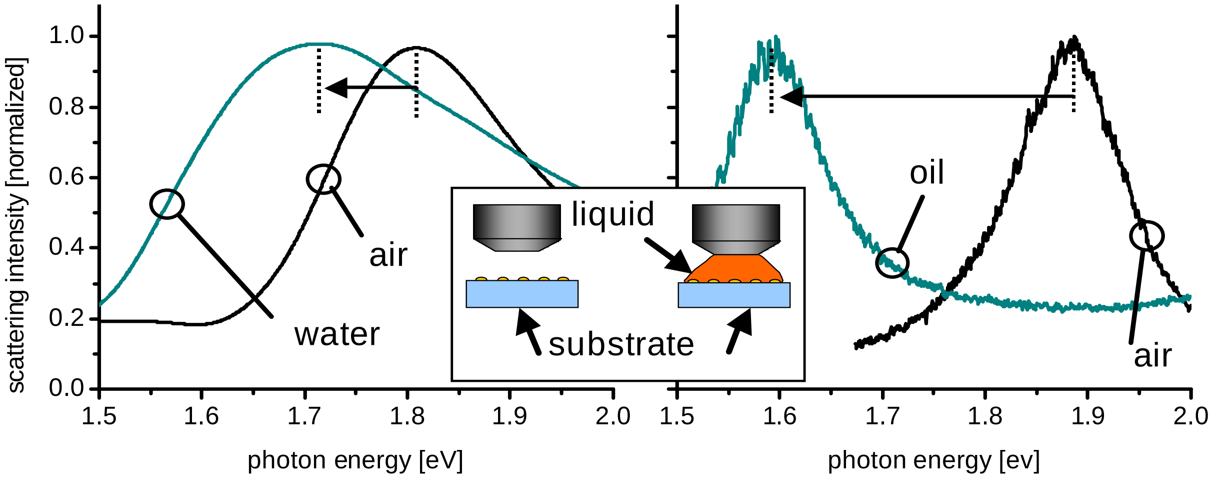

Fig. 9.2: Red-shift of the particle plasmon resonances of individual nanodisks due to the different refractive index of water (left) and oil (right) as compared to air. Center: experimental setup.

The observed red shift agrees approximately with the shift calculated using the simple Rayleigh scattering law for the polarizability of small ellipsoidal particles (cf. Sec. 4.5.2). The aspect ratio of the nanodisks is estimated from the position of the particle plasmon resonance in air. The dielectric function of the medium ϵ_m is computed by averaging between the ITO substrate ($\epsilon \approx 4$) and the surrounding medium, i.e. air ($\epsilon = 1$), water ($\epsilon = 1.78$) or oil ($\epsilon = 2.25$). This calculation predicts a larger red-shift for particles with higher aspect ratio, which is in agreement with my observation.

9.2 Local concentration sensor

In the previous section, two kinds of liquids with different refractive indices have been added to the sample. Another way to change the refractive index of the medium covering the substrate is to dissolve substances with a high refractive index in a liquid solvent with a lower refractive index. I use here sugar (saccharose) dissolved in water for this purpose. Saccharose is an inexpensive organic substance with high refractive index, which is not harmful and easily soluble in water.

Fig. 9.3 a shows single particle scattering spectra from the same silver nanosphere embedded in water with various (weight) concentrations of saccharose. Clearly a red-shift on increasing saccharose concentration is observed. The magnitude of this red-shift is linearly dependent on the concentration and agrees reasonably with calculations using Mie-theory (Fig. 9.3 b). The linear dependence is expected for a concentration effect because (i) the refractive index of a mixture is the weighted average of its constituents and (ii) the plasmon resonance energy depends, to a first approximation, linearly on the refractive index. Rinsing the sample with clean water fully reverses the shift. This reversibility and the observed linear dependence proves that the shift is caused by the concentration of sugar molecules dissolved in the liquid, *not* by sugar molecules adsorbed to the particle surface.

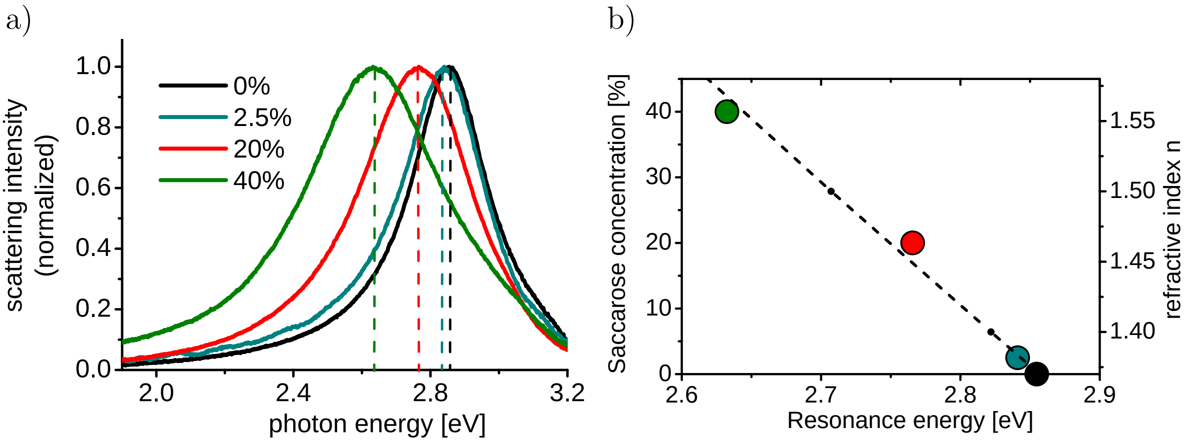

Fig. 9.3: a) Measured scattering spectra of the same silver nanospheres (60 nm) partly immersed in aqueous saccharose solutions of various (weight) concentrations b) Dots: resonance energy versus saccharose concentration (scale on the left). Line: calculated resonance position for embedding media with various refractive indices (scale on the right). Note that the refractive index indicated on the right does *not* correspond to the saccharose solution on the left (e.g. 40% $\leftrightarrow n = 1.40$). The reason for the discrepancy is unknown but could be due to the uncertainty in the dielectric function of silver, which strongly influences resonance position.

9.3 Increasing sensitivity

For the experiments in the previous section, relatively high concentrations of sugar are used in order to have easily observable effects. This raises immediately the question whether or not it is possible to measure much smaller concentrations. In general, the sensitivity of a particle plasmon based sensor is determined by three parameters: (i) the magnitude of the induced shift. The smallest detectable shift is determined by (ii) the measurement accuracy and (iii) the linewidth of the plasmon resonance, since a given resonance-shift is more easily observed for a smaller line.

In this section I want to address the limitations to the parameters (i) – (iii) and show ways to improve these values. Since the limitation by the measurement accuracy (ii) is the most difficult to tackle, I will discuss it first.

9.3.1 Measurement accuracy

The dark-field and total internal reflection microscopy setups used in this work are not designed for high accuracy resonance energy determination, so measurement accuracy can be drastically increased in a dedicated setup. It is difficult, however, to give the practical limit. Gluodenis *et al.* (1999) have shown that phenol concentrations down to $0.4\,\mathtt{mM}$ can be determined with a large ensemble of particles in suspension. Since the resonances of single particles are inherently smaller than ensemble resonances, this value should be easily reached with the method described here. Nevertheless, I cannot give a meaningful limit on the principal or practical limit of the measurement accuracy. Currently, resonance shifts down to approximately $\Delta\lambda = 2\,\mathtt{nm}$ have been reliably measured on single particles.

9.3.2 Linewidth and magnitude of the resonance-shift

In principle, there are two ways to increase the intrinsic measurement sensitivity of particle plasmon based nanosensors regardless of the measurement accuracy: either the magnitude of the shift induced by a given change in the environment has to be increased — or the linewidth of the resonance has to be reduced in order to make a given shift in resonance energy more easily observed.

I show here that both effects are achieved simultaneously by using nanorods instead of nanospheres(i). In Fig. 9.4 a, the resonance shift induced by changing the environment from air ($n = 1$) to water ($n = 1.33$) is compared for a gold nanorod with the dimensions of roughly 20 nm × 20 nm × 60 nm and a gold nanosphere with a diameter of 40 nm. The absolute magnitude of the red-shift for the nanorod (87 meV) is almost twice as large as the shift for the nanosphere (54 meV). Furthermore, the shift relative to the linewidth is even more pronounced in nanorods because of their extremely small resonances. Here, the red-shift in the nanorod is about 80% of its resonance linewidth as compared to about 20% for the nanosphere.

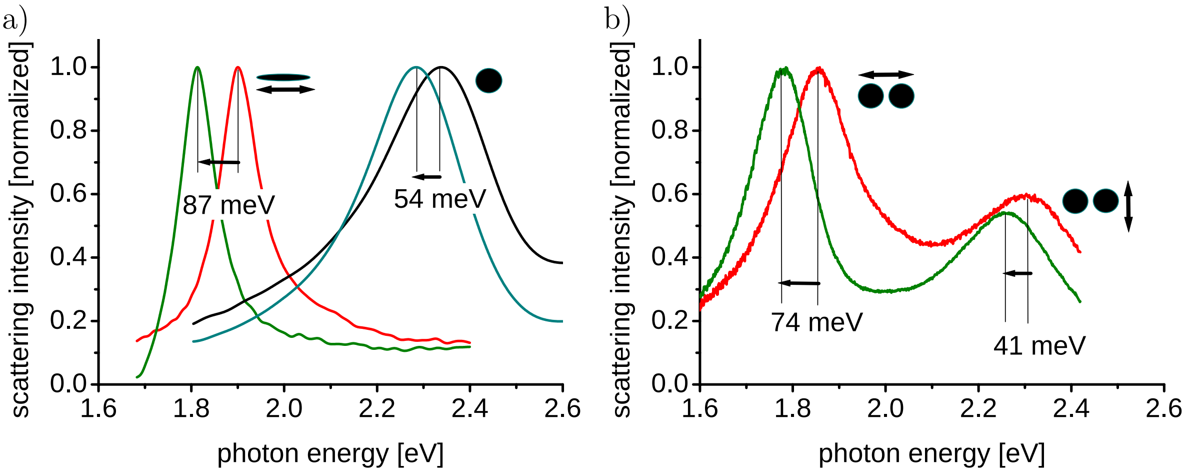

Fig. 9.4: a) Measured scattering spectra of the same gold nanoparticles partially exposed to air and immersed in water, left nanorod, right 40 nm nanosphere; b) pair of 40 nm gold nanospheres in air and water. In all cases the resonance in water is shifted to the red compared to the resonance in air. The magnitude of the shift is larger for nanorods and the long axis mode of particle pairs than the shift for individual particles.

Another approach to increase the magnitude of the shift in plasmon resonance energy is to use close-lying, electrodynamically coupled particles, the so-called particle pairs. Particle pairs have two resonances — similar to nanorods — along and perpendicular to the axis connecting the particles. I call the low energy resonance mode, which is along the connecting axis, the 'long axis' mode in analogy to the low energy resonance in nanorods. The sensitivity on the embedding medium of this long axis mode of particle pairs should be increased, because the electrodynamic coupling of the two particles depends strongly on the medium *inbetween* the particles. I demonstrate this effect in Fig. 9.4 b, where the scattering spectra of the same particle pair exposed to air and water are compared. The shift of the long axis mode is larger (74 meV) than that for an individual particle (54 meV);

(i) Note that nanorods could not be used in an ensemble measurement because of the large inhomogeneous broadening of their ensemble extinction spectrum.

the shift of the high energy resonance mode is smaller (41 meV). The shift relative to the linewidth increases from 20% in individual particles to about 30% for the long axis mode, but this is far less than observed for nanorods.

I should mention another advantage of nanorods compared to spherical particles: their high scattering efficiency, which is due to their large radiative quantum yield and their high polarizability compared to nanospheres of similar volume. This high scattering efficiency makes the observation much easier and faster. Since it is experimentally difficult to determine the absolute scattering intensity, it is difficult to quantify this effect, but it is likely to be a factor of 10 or more (cf. Sec. 8.4). Nanorods are therefore the ideal solution for single particle particle plasmon based nanosensors: they combine high scattering efficiency, small linewidth and large sensitivity on the environment.

9.3.3 Conclusion

In conclusion, the measurements presented here show that employing particle plasmons as sensor for concentrations as described by Gluodenis *et al.* (1999) is easily scaled down to the single particle level using the scattering spectroscopy technique developed here. The technical limit of detecting low concentrations has not been approached so far, but I show that the sensitivity can be increased by using nanorods or particle pairs. Nanorods are the ideal solution for this kind of application due to their high scattering efficiency, their small linewidth and large sensitivity on the environment. The shift of the particle plasmon resonance of an individual particle gives the *local* concentration in a volume as small as 0.1 attoliter (cf. Sec. 4.5.4). The total amount of molecules in this volume causing the observed shift is extremely low (on the order of a few thousands).

9.4 Binding indicator

Another way to change the refractive index of the medium around an individual particle is to specifically bind substances to its surface (Kubitschko *et al.*, 1997). This allows the detection of this substance and its binding kinetics to the particle in a similar manner to the surface plasmon resonance (SPR) sensors utilizing plasmons on extended metal films. The advantage over the SPR method is the possibility to scale-down the device much further, which allows, in principle, massively parallel monitoring.

The feasibility of this concept on a single particle level is demonstrated by Fig. 9.5 . This plot shows the measured shift of plasmon resonance energy upon binding of a molecule (dodecan-thiol) to the surface of the metal particle. A very small amount of this molecule is added to the solvent. The magnitude of the observed shift cannot be explained by the tiny change in refractive index due to the solvation of the molecule. Also, it is not reversed upon washing with solvent. Both observations prove the (tight) binding of the dodecan-thiol molecule to the surface of the particle. The shift increases with time until it reaches saturation demonstrating the applicability to determining binding kinetics.

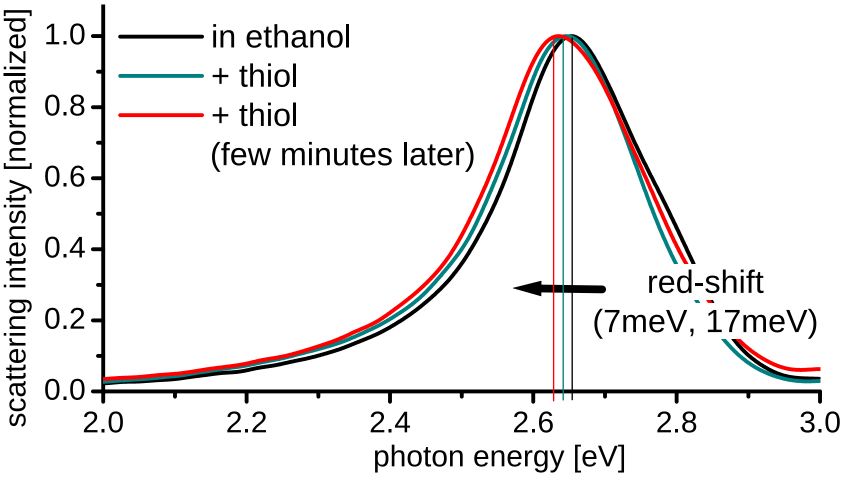

Fig. 9.5: Silver particle (60 `nm`) partially immersed in ethanol (black). The resonance position shifts towards lower energies immediately after adding a very small amount of dodecan-thiol (green line). This shift increases with time for several minutes until it saturates (red line).

9.5 Particle charge sensor – Redox potential sensor

It has been shown (Mulvaney, 1996) that the particle plasmon resonances can be shifted towards *higher* energies by increasing the number of electrons in the particle, i.e. charging the particle negatively. This blue-shift can be understood from the basic relation for the plasmon frequency ω_p given in the quasi-free-electron model (Sec. 2.2.1):

$$\omega_p = \sqrt{n\, e^2/\varepsilon_0 m^*} \tag{9.1}$$

From this equation follows an increase in frequency for increasing electron density n.

The charge of metal colloids in suspension is determined by chemical reactions described by the corresponding redox potentials. Adding a strongly reducing agent, such as $NaBH_4$, to particles immersed in water should lead to a transfer of negative charges to the metal particle (Mulvaney, 1996).

I show here that this effect can be observed at the single-particle level (Fig. 9.6). A very small amount of $NaBH_4$ added to particles immersed in water leads to a considerable (32 `meV`) blue-shift of the resonance position.

The observations shown here imply that particle charging has to be kept in mind in any potential sensor application. Possibly, this charge-effect could also be *used* to monitor local redox potentials or particle charges in general.

9.6 Discussion

I have demonstrated proof-of-principle that changes in the particle-environment properties due to local concentrations, binding events or charge transfer processes can be detected *locally* by monitoring the plasmon resonance. Besides this experimental success, the question remains whether such detection is useful for real devices.

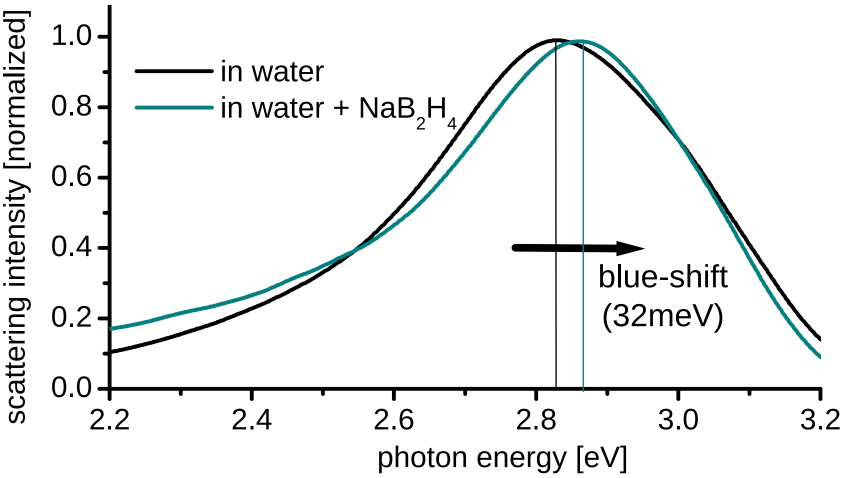

Fig. 9.6: Silver particle (60 nm) partially immersed in water (black). The resonance position shifts towards higher energies immediately after adding a very small amount of NaB_2H_4 (green line).

It is unlikely (but not impossible) that the sensitivity of such a sensor can compete with the very advanced optical sensors employing *surface* plasmons on extended metal films. These have been successfully used to detect low concentrations of molecules and to determine binding kinetics and affinity constants (see Canziani *et al.* (1999); Mullett *et al.* (2000) and the '*Survey of the 1999 surface plasmon resonance biosensor literature*' by Rich and Myszka (2000)).

Plasmon resonances of large *ensembles* of metal particles have been used as sensors in some cases (Kubitschko *et al.*, 1997; Englebienne, 1998; Takai, 1998; Bauer *et al.*, 1999; Gluodenis *et al.*, 1999). As mentioned before, none of these applications has made use of the *local* information particle plasmons give due to the lack of single particle spectroscopic methods. Therefore, the main advantage of particle plasmons over surface plasmons has not been employed. I believe that the demonstration of single particle nanosensors presented here will open up new implementations of the above mentioned applications and possibly lead to completely new applications.

9.7 Summary

The experiments described in this chapter have shown the applicability of plasmons in metal nanoparticles as sensors for various physical and chemical processes. For the first time, these processes have been monitored on single particles. Only such single particle sensors make effective use of the extremely small volume on the order of an attoliter as probed by the plasmon resonance of a single particle. I demonstrate therefore the first optical *nano*sensors based on particle plasmon resonances. It is shown that local concentrations, binding events and particle charges can be detected. First experiments towards increasing the sensitivity have been carried out.

10. ELECTRICALLY CONTROLLED LIGHT SCATTERING

The plasmon resonance shift induced by a change in the particle surrounding can be used as a passive sensor for such changes. This has been demonstrated in the previous chapter. It is shown in this chapter that it is possible to *actively* change the plasmon resonance frequency *electrically.*

Electrically controlled switching of light is a key ingredient in modern optical communication and display systems. Several techniques are in use today. One possibility is to directly modulate the light output of a light emitting device, e.g., by varying the driving current of a light emitting (laser-) diode. For many applications, however, the light is modulated externally. An example is the acousto-optical modulator (AOM), where light is diffracted by a refractive index modulation. This refractive index modulation is induced by an acoustic wave introduced and controlled electrically via the piezo electrical effect (Chang, 1995). Another example are electro-optical modulators employing the linear (Pockels) or quadratic (Kerr) electro-optic effect, which changes electrically the anisotropy in the refractive index (Maldonado, 1995). Such optoelectronic modulators and switches usually change the properties (intensity, phase, frequency, polarization) of transmitted, reflected or diffracted light beams. To the best of my knowledge, optoelectronic modulators or switches based on electrically controlled light *scattering* are not known up to now. However, such optoelectronic scattering devices would be highly desirable. Electrically and spatially controlled light coupling out of and inbetween waveguides, photonic crystals and other micro-optical components are potential applications.

I show here that such electrically controlled light scattering can be achieved by electrically shifting the particle plasmon resonance. The basic idea is that the electric field $\vec{F}$ alters the refractive index of the embedding dielectric matrix. For this purpose, silver nanoparticles are incorporated in a liquid crystal (LC). The applied electric field $\vec{F}$ aligns the LC molecules leading to an anisotropic refractive index and thus to a polarization dependent spectral shift of the particle plasmon.

10.1 Principle of the experiment

Samples are fabricated as described in Sec. 6.2 using spherical silver particles with a mean diameter of 60 nm. Gold electrodes of 100 nm thickness separated by a 200 μm gap are evaporated onto the substrate before adding the nanoparticles. The resulting sample structure is schematically shown in Fig. 10.1 a and b.

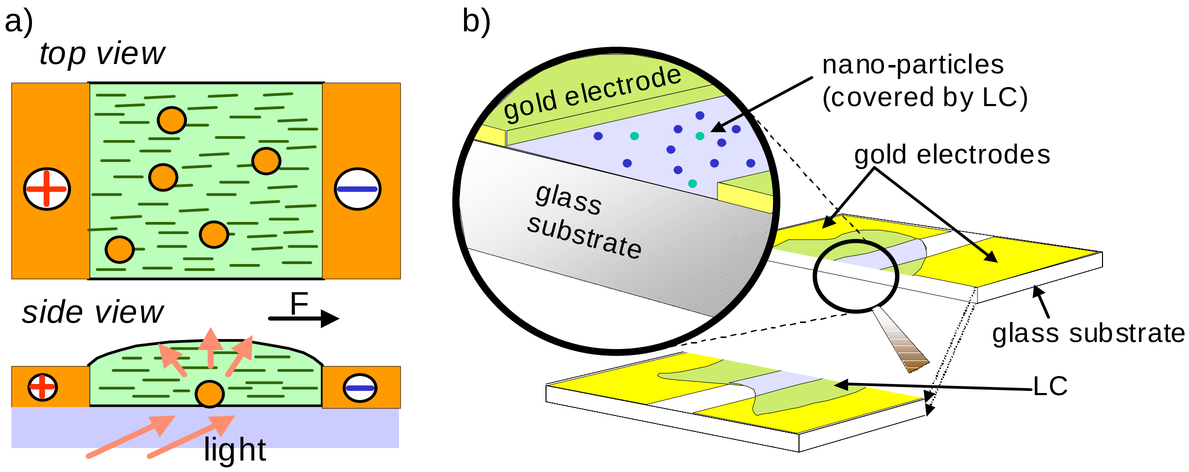

Fig. 10.1: a) Top view and side view of the sample structure. Silver nanoparticles are deposited between two gold electrodes with average interparticle distances on the order of a few microns and covered with a liquid crystal (green). An electric field $\vec{F}$, applied between the electrodes ($\oplus/\ominus$), aligns the liquid crystal molecules (dashes) in the sample plane. b) More realistic three dimensional drawing of the sample structure.

Electric fields of typically $|\vec{F}| = 20\,000\,\mathtt{V/cm}$ are applied between the electrodes to align the LC molecules in the plane of the substrate (Fig. 10.1 a). I use a commercially available nematic liquid crystal with high anisotropy in refractive index (E7, Merck, $n_\perp = 1.5211, n_\parallel = 1.7464$).

The orientation of the liquid crystal molecules can be checked by polarization microscopy using two orthogonal polarization filters for the excitation and the collected light. The optical anisotropy of liquid crystals turns the polarization direction of light which is not polarized parallel to one of its major axes. Such images show that the liquid crystal film consists of domains in which the LC molecules are spontaneously aligned (Fig. 10.2), possibly due to interaction with the sample surface. This alignment is found to remain stable on application of an electric field $\vec{F}$ between the electrodes. The polarization contrast between different domains increases strongly, however, on switching on the external field.

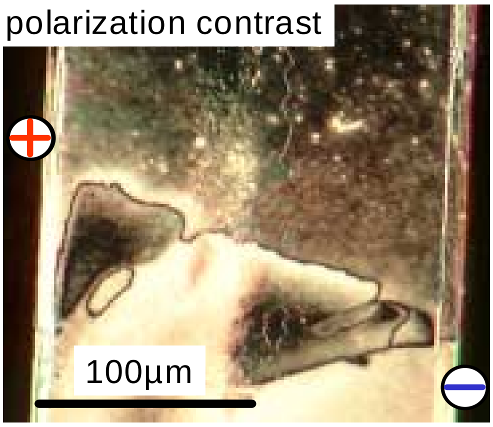

Fig. 10.2: Polarization contrast image of the part of the sample area between the electrodes showing the domain structure of the liquid crystal orientation.

The observed domain structure shows that the alignment of the liquid crystal molecules is not as homogeneous as depicted in Fig. 10.1 a. The change in polarization contrast by switching on the electric field shows, however, the electric field has some influence on the orientation of the liquid crystal molecules. Since I focus here on demonstrating the feasibility of the concept of electrically controlling plasmon resonances using liquid crystals, this local change in orientation is enough to achieve the effect. Nevertheless, an improvement of the liquid crystal alignment would be highly desirable and steps towards this goal are currently under way.

10.2 Electrically induced plasmon resonance shift

Single particle spectra are recorded with the dark-field setup described in Sec. 5.2.3 with and without external electric field $\vec{F}$. A reversible shift of the plasmon resonance of individual particles by switching the field on and off is clearly observed. In Fig. 10.3 a and b, two typical examples for particles in different domains are shown. Depending on the domain, both red- and blue-shifts are observed upon application of the field $\vec{F}$. The shift is approximately 70 meV in both cases, which leads to a contrast of 2-3 of the scattering intensity between on and off states at the tails of the resonances (indicated by the arrows in Fig. 10.3). This demonstrates that both silver nanoparticles act as efficient optoelectronic switches for light scattering.

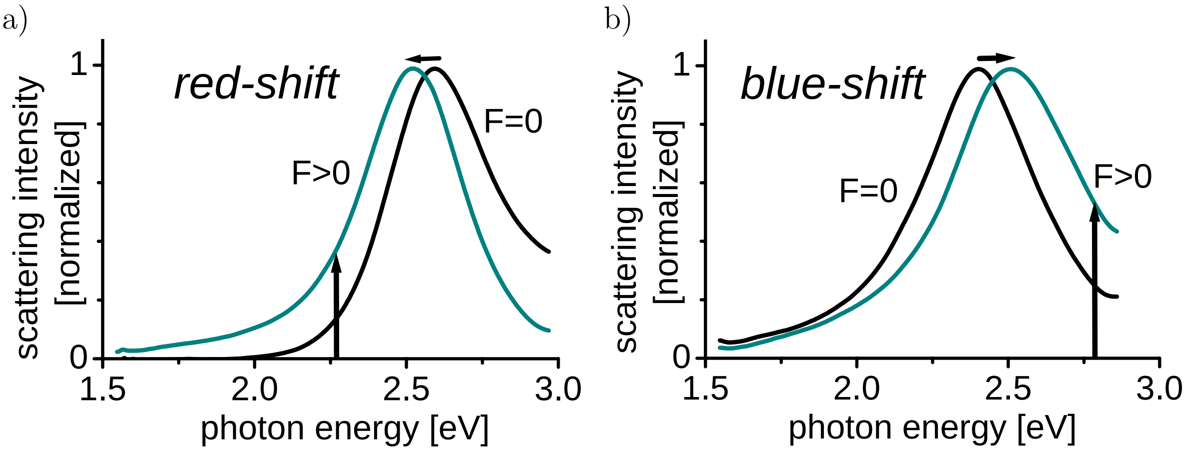

Fig. 10.3: a) Light scattering spectra of an individual silver nanoparticle, with and without applied electric field $\vec{F}$. The plasmon resonance shifts to the red upon application of the electric field. b) Another particle showing a blue-shift of the plasmon resonance. In both cases the resonances shifts by about 70 meV. Arrows indicate the optical contrast between off- and on-states at selected wavelengths.

10.3 Polarization effect

In order to explain the observed difference in the direction of the shift (red- and blue-shift), the direction of polarization of the incident light is systematically changed. For the spectra shown above, the polarization direction is parallel to the external electric field. The resonance energy depends in a sinusoidal way on the polarization direction similar to the case of nanorods shown in Sec. 8.4 . This is shown in Fig. 10.4 for a silver nanosphere covered by liquid crystal molecules. Thus the particles behave *optically* like ellipsoids(i).

(i) The polarization dependence of the plasmon resonance was carefully checked for each of the particles studied *before* adding the liquid crystal. This ensures that only (geometrically) spherical particles are considered here.

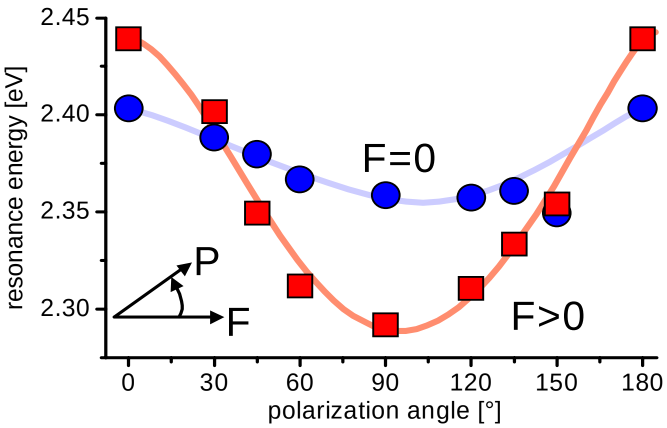

Fig. 10.4: Example of the dependence of the particle-plasmon resonance energy upon polarization angle of the incident light $\vec{P}$ (measured relative to the direction of the applied field $\vec{F}$). At 0°, a blue-shift of the particle plasmon is observed upon switching on the electric field $\vec{F}$, while at 90°a red-shift is observed.

Comparing now the resonance positions as a function of polarization angle for the cases with and without applied electric field $\vec{F}$ (Fig. 10.4), a clear difference in the modulation magnitude of the resonance energy with polarization angle is observed. In other words, the amount of splitting between maximum and minimum resonance positions changes. This splitting is taken as a measure for the *'optical ellipticity'* of the particles — analogously to the splitting in ellipsoidal particles (nanorods), which increases with increasing aspect ratio. The optical ellipticity increases on application of the electric field, which leads to both red- and blue-shifts compared to the zero-field case for different polarization angles.

10.4 Model and discussion

A model for the physical effect causing the resonance shift has to explain the following experimental details:

(i) both red- and blue-shifts are observed for polarization parallel to the external electric field (Fig. 10.3),

(ii) a red-shift turns into a blue-shift on changing the polarization direction by 90°and vice versa (Fig. 10.4), and

(iii) the optical ellipticity increases on application of the external field (Fig. 10.4).

It is not surprising that spherical particles in an anisotropic environment behave optically similar to ellipsoidal particles in a homogeneous environment — in fact, it is expected from simple electrostatic theory (Jones, 1945). This optical ellipticity due to the electrically induced alignment of the liquid crystal molecules explains all observations if we assume a random orientation of the alignment directions of the liquid crystal domains, which is not changed by the external electric field. The external field merely increases the ordering in the plane of the sample either by tilting the molecules into the sample plane or by reducing their disorder. This model is schematically shown in Fig. 10.5 . The observation of either a red- or blue-shift depends on the orientation of the domain relative to the polarization direction of the exciting light.

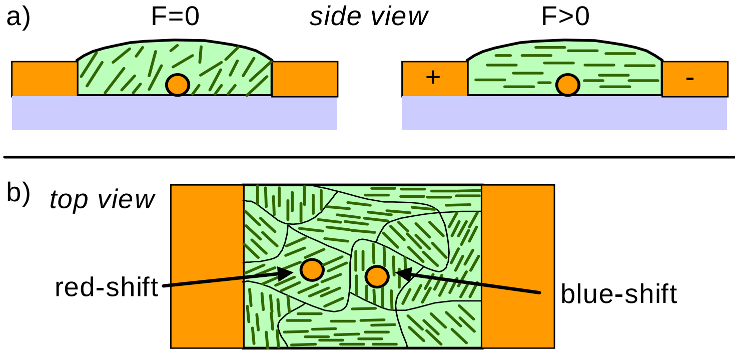

Fig. 10.5: a) A model scenario in which the experimentally observed increased polarization anisotropy on application of an external field $\vec{F}$ is explained by a stronger alignment of the liquid crystal molecules and a tilt into the sample plane. b) The spectral direction of the plasmon resonance shift (blue- or red-shift) is due to domains of different horizontal orientation of the liquid crystal molecules. This orientation does not change upon application of the external field.

In order to achieve the same direction for the field-induced spectral shift of the particle plasmon for all particles, the ordering of the LC molecules around the metal nanoparticles has to be better controlled. In particular, domains with different orientations have to be avoided. This technical problem can be solved by either optimizing the sample preparation procedure or by using different electric field geometries.

10.5 Conclusion

In conclusion, it is shown for the first time that the plasmon resonance of silver nanoparticles can be shifted over a wide spectral range by electrical alignment of liquid crystal molecules in their vicinity. The spherical nanoparticles become optically ellipsoidal when adjacent anisotropic liquid crystal molecules are aligned. The experiments presented here show that this novel effect can be used for electrically controlled light scattering with high contrast and with considerable spectral selectivity.

11. SUMMARY

In the previous chapters, new experimental results on the interaction of light with metal nanostructures have been presented, which will be briefly summarized here.

In Chap. 7 optical transmission through individual nanoholes in gold, silver, and aluminum films has been investigated. Using a scanning near-field optical microscope (SNOM) in illumination mode, surface plasmons were locally excited on the films; this approach avoids complications associated with surface-plasmon excitation via gratings. The patterns observed show unambiguously that light transmission through the nanoholes is supported by surface plasmons propagating along the surface of the films. The propagation direction is given by the light polarization. I have found characteristic interference effects due to scattering of surface plasmons off neighboring holes.

The directed launching of surface plasmons below a SNOM tip may be used to selectively transmit light through distinct holes according to the light polarization in the fiber — a process that may figuratively be described as “nanogolf”. This polarization controlled addressing of specific holes may be applicable for de-multiplexing purposes in future optical systems.

In order to spectrally investigate plasmon modes in metal nanoparticles, I have used the methods of near-field and far-field single particle scattering spectroscopy. The near-field scattering spectroscopy was found to be very laborious, hence preference was given to the faster and more flexible far-field technique. High signal to background contrast has been achieved in the far-field microscope either by total internal reflection (TIR) or dark-field (DF) illumination.

This far-field method has been applied for the first time to determine the amount and the mechanism of particle plasmon damping (Chap. 8). Experiments on ordered arrays of nanodisks have established the reliability of the method. Subsequent investigations have determined the dephasing times of gold and silver nanospheres and gold nanorods. The results of this first systematic and conclusive experimental study on individual metal nanoparticles answer the long debated question of the amount of plasmon damping in gold nanoparticles. Good agreement with calculations using the bulk dielectric function of gold shows that collective dephasing and surface effects contribute negligibly to the overall damping in the particles under investigation here. Only radiation damping and single electron scattering contribute significantly. Nanorods are found to combine small linewidth and a large local field enhancement factor with a relatively large radiative quantum yield and strong light-scattering. Comparison with theory shows that interband damping is suppressed in nanorods and radiation damping is negligible. This allows the qualitative and quantitative deduction of the relative contributions of radiation, inter- and intraband damping in gold nanoparticles. Furthermore, it allows the determination of the ‘true’ plasmon dephasing time in the sense of a pure plasmon oscillation without coupling to other excitations (interband) or photons.

The spectroscopic investigation of plasmons in single nanoparticles can also be used to determine the refractive index of the medium surrounding the particle. This is especially interesting as the far-field setup used in this work, allows the partially immersion of the particles in liquids. I demonstrate in Chap. 9 for the first time how this can used to build optical nanosensors based on particle plasmons. It is shown how these can be used to determine local concentrations, local binding events, and redox reactions. The sensing volume of such a nanosensor is on the order of attoliters. First experiments towards increasing the sensitivity show the potential of this technique.

Actively changing the environment around metal particles by electrically aligning liquid crystal molecules allows to shift the resonance frequency over a wide spectral range. The experiments presented in Chap. 10 show that this novel effect can be used for electrically controlled light scattering with high contrast and with large spectral selectivity.

BIBLIOGRAPHY

Adam, P.-M., Benrezzak, S., Bijeon, J., and Royer, P. (2000). *Localized surface plasmons on nanometric gold particles observed with an apertureless scanning near-field optical microscope.* J. Appl. Phys. 88, 6919.

Alivisatos, A. P., Johnsson, K. P., Peng, X., Wilson, T. E., Loweth, C. J., Bruchez Jr, M. P., and Schultz, P. G. (1996). *Organisation of 'nanocrystal molecules' using DNA.* Nature. 382, 607.

Alivisatos, P. A., Barbara, P. F., Castleman, J. C., Dixon, D. A., Klein, M. L., McLendon, G. L., Miller, J. S., Ratner, M. A., J, R. P., Stupp, S. I., and Thomson, M. E. (1998). *From Molecules to Materials: Current Trends and Future Directions.* Adv. Mater. 10, 1297.

Allen, L. and Eberly, J. (1975). *Optical Resonance and Two-Level Atoms.* Wiley, New York.

Ashcroft, N. W. and Mermin, N. D. (1976). *Solid State Physics.* Saunders College, Philadelphia.

Bauer, G., Pittner, F., and Schalkhammer, T. (1999). *Metal Nano-Cluster Biosensors.* Microchim. Acta. 131, 107.

Bohren, C. and Huffman, D. (1982). *Absorption and Scattering of Light by Small Particles.* John Wiley & Sons, New York.

Canziani, G., Zhang, W., Cines, D., Rux, A., Willis, S., Cohen, G., Eisenberg, R., and Chaiken, I. (1999). *Exploring Biomolecular Recognition Using Optical Biosensors.* Methods. 19, 253.

Chan, V. Z.-H., Spatz, J. P., and Möller, M. (2001). Gold nanoarrays for lithography and tethering of single molecules. In H. Hahn, D. Feldheim, C. Kubiak, R. Tannenbaum, and R. Siegel, editors, *Synthesis, Functional Properties, and Applications of Nanostructures*, volume 676. Materials Research Society (MRS).

Chang, I. C. (1995). *Handbook of Optics*, volume II, chapter 12. McGraw-Hill, New York.

Chang, S.-S., Shih, C.-W., Chen, C.-D., Lai, W.-C., and Wang, C. (1999). Langmuir. 15, 701.

Charle, K.-P., König, L., Nepijko, S., Rabin, I., and Schulze, W. (1998). *The Surface Plasmon Resonance of Free and Embedded Ag-Clusters in the Size Range 1,5 nm $< D <$ 30 nm.* Cryst. Res. Technol. 33, 1085.

Clark, H. A., Hoyer, M., Philbert, M. A., and Kopelmann, R. (1999). *Optical Nanosensors for Chemical Analysis inside Single Living Cells. 1. Fabricatopn, Characterization, and Methods for Intracellular Delivery of PEBBLE Sensors.* Anal. Chem. 71, 4831.

Dawson, P., Bryanbrown, G., and Sambles, J. R. (1994). *Broad-Band Excitation and Emission of Surface-Plasmons.* J. Mod. Opt. 41, 1279.

Demtröder (1996). *Laser Spectroscopy.* Springer, Berlin, 2nd edition.

Drude, P. (1900). *Zur Elektronentheorie der Metalle.* Annalen der Physik. 1, 566.

Ebbesen, T. W., Lezec, H. J., Ghaemi, H. F., Thio, T., and Wolff, P. A. (1998). *Extraordinary optical transmission through sub-wavelength hole arrays.* Nature (London). 391, 667–9.

Englebienne, P. (1998). *Use of colloidal gold surface plasmon resonance peak shift to infer affinity constants from the interactions between protein antigens and antibodies specific for single or multiple epitopes.* Analyst. 123, 1599.

Fischer, U. C. (1986). *Submicrometer aperture in a thin metal film as a probe of its microenvironment through enhanced light scattering and fluorescence.* J. Opt. Soc. Am. B. 3, 1239.

Foiles, C. (1985). Optical properties of pure metals and binary alloys. In K. Hellwege and J. Olsen, editors, *Metals: Electronic Transport Phenomena*, volume 15b of *Landolt-Börnstein.* Springer, Berlin.

Genzel, L. and Kreibig, U. (1980). *Dielectric Function and Infrared Absorption of Small Metall Particles.* Z. Physik B. 37, 93.

Ghaemi, H. F., Thio, T., Grupp, D. E., Ebbesen, T. W., and Lezec, H. J. (1998). *Surface plasmons enhance optical transmission through subwavelength holes.* Phys. Rev. B. 58, 6779.

Gluodenis, M., Manley, C., and Foss, C. A. (1999). *In situ monitoring of the change in extinction of stabilized nanoscopic gold particles in contact with aqueous phenol solutions.* Analytical Chemistry. 71, 4554.

Grosse, S. (1998). *Raumzeitliche Dynamik optisch angeregter Elektron-Loch-Paare in Halbleiter-Nanostrukturen.* Ph.D. thesis, Ludwig-Maximilians-Universität München.

Grupp, D. E., Lezec, H. J., Thio, T., and Ebbesen, T. W. (1999). *Beyond the Bethe limit: Tunable enhanced light transmission through a single sub-wavelength aperture.* Adv. Mater. 11, 860.

Grupp, D. E., Lezec, H. J., Ebbesen, T. W., Pellerin, K. M., and Thio, T. (2000). *Crucial role of metal surface in enhanced transmission through subwavelength apertures.* Appl. Phys. Lett. 77, 1569.

Güntzer, D. (1999). *Optische Messungen an Oberflächenplasmonen.* Zulassungsarbeit zum Staatsexamen, Ludwig-Maximilians-Universität München.

Hayat, M. (1989). *Colloidal Gold: Principles, Methods, and Applications*, volume 1-3. Academic Press, London, 1st edition.

Hecht, B., Bielefeldt, H., Novotny, L., Inouye, Y., and Pohl, D. (1996). *Local Excitation, Scattering, and Interference of Surface-Plasmons.* Phys. Rev. Lett. 77, 1889.

Heilweil, E. J. and Hochstrasser, R. M. (1985). *Nonlinear spectroscopy and picosecond transient grating study of colloidal gold.* J. Chem. Phys. 82, 4762.

Heller, R. A., Schena, M., Chai, A., Shalon, D., Bedilion, T., Gilmore, J., Wolley, D. E., , and Davis, R. W. (1997). *Discovery and analysis of inflammatory disease-related genes using cDNA microarrays.* Roc. Natl. Acad. Sci USA. 94, 2150.

Hohng, S. C., Yoon, Y. C., Kim, D. S., Malyarchuck, V., Lienau, C., Park, J. W., Yoo, K. H., and Y, R. H. (2001). Transmission, controll and coherent propagation of surface plasmons in metal nanostructures. In *Postdeadline Papers*. Quantum Electronics and Laser Science Conference (QELS), Baltimore. (QPD4).

Jackson, J. (1975). *Classical Electrodynamics*. Wiley, New York, 2nd ed. edition.

Johnson, P. and Christy, R. (1972). *Optical Constants of the Noble Metals*. Phys. Rev. B. 6, 4370.

Jones, R. C. (1945). *A Gerneralization of the Dielectric Ellipsoid Problem*. Phys.Rev. 68, 93 and 213.

Karrai, K. and Grober, R. D. (1995). *Piezoelectric tip-sample distance control for near field optical microscopes*. Appl. Phys. Lett. 66, 1842.

Kawabata, A. and Kubo, R. (1966). *Electronic Properties of Fine Metallic Particles. II. Plasma Resonance Absorption*. J. Phys. Soc. Jpn. 21, 1765.

Keilmann, F. (1981). *Infrared High-Pass Filter with High Contrast*. Int. J. of Infrared and Millimeter Waves. 2, 259. and references therein.

Kim, T. J., Thio, T., Ebbesen, T. W., Grupp, D. E., and Lezec, H. J. (1999). *Control of optical transmission through metals perforated with subwavelength hole arrays*. Optics Letters. 24, 256.

Klar, T. (1997). *Nahfeldoptische Untersuchungen an Gold-Nanopartikeln*. Diplomarbeit, Ludwig-Maximilians-Universität München.

Klar, T., Perner, M., Grosse, S., von Plessen, G., Spirkl, W., and Feldmann, J. (1998). *Surface-Plasmon Resonances of Single Metallic Nanoparticles*. Phys. Rev. Lett. 80, 4249.

Kneipp, K., Wang, Y., Kneipp, H., Itzkan, I., Dasari, R. R., and Feld, M. S. (1996). *Population pumping of excited vibrational states by spontaneous surface-enhanced Raman scattering*. Phys. Rev. Lett. 76, 2444.

Kopitzki, K. (1993). *Einführung in die Festkörperphysik*. Teubner, Stuttgart, 3 edition.

Kreibig, U. and Vollmer, M. (1995). *Optical Properties of Metal Clusters*, volume 25 of *Springer Series in Materials Science*. Springer, Berlin.

Krenn, J., Wolf, R., Leitner, A., and Aussenegg, F. (1997). *Near-Field Optical Imaging the Surface Plasmon Fields of Lithographically Designed Nanostructures*. Opt. Commun. 137, 46.

Krenn, J. R., Salerno, M., N., F., Lamprecht, B., Schider, G., Leitner, A., Aussenegg, F. R., Weeber, J. C., Dereux, A., and Goudonnet, J. P. (2001). *Light field propagation by metal micro- and nanostructures*. Journal of Microscopy. 202, 122.

Kretschmann, E. (1972). *Untersuchungen zur Anregung und Streuung von Oberflächenplasmaschwingungen an Silberschichten*. Ph.D. thesis, Hamburg.

Kryukov, A. E., Kim, Y. K., and Ketterson, J. B. (1997). *Surface plasmon scanning near-field optical microscopy*. J. Appl. Phys. 82, 5411.

Kubitschko, S., Spinke, J., Bruckner, T., Pohl, S., and Oranth, N. (1997). *sensitivity enhancement of optical immunosensors with nanoparticles.* Analytical Biochemistry. 253, 112.

Lamprecht, B., Leitner, A., and Aussenegg, F. (1997). *Femtosecond Decay-Time Measurement of Electron-Plasma Oscillation in Nanolithographically Desingned Silver Particles.* Appl. Phys. B. 64, 269.

Lamprecht, B., Krenn, J., Leitner, A., and Aussenegg, F. R. (1999). *Resonant and Off-Resonant Light-Driven Plasmons in Metal Nanoparticles Studied by Femtosecond-Resolution Third-Harmonic Generation.* Phys. Rev. Lett. 83, 4421.

Liau, Y.-H., Unterreiner, A. N., Chang, Q., and Scherer, N. F. (2001). *Ultrafast Dephasing of Single Nanoparticles Studied by Two-Pulse Second-Order Interferometry.* J. Phys. Chem. B. 105, 2135.

Link, S. and El-Sayed, M. A. (1999a). *Size and Temperature Dependence of the Plasmon Absorption of Colloidal Gold Nanoparticles.* J. Phys. Chem. B. 103, 4212.

Link, S. and El-Sayed, M. A. (1999b). *Spectral Properties and Relaxiation Dynamics of Surface Plasmon Electronic Oscillations in Gold and Silver Nanodots and Nanorods.* J. Phys. Chem. B. 103, 8410.

Link, S. and El-Sayed, M. A. (2000). *Shape and size dependence of radiative, non-radiative and photothermal properties of gold nanocrystals.* Int. Rev. Phys. Chem. 19, 409.

Logan, N. A. (1965). *Survey of Some Early Studies of the Scattering of Plane Waves by a Sphere.* Proc. IEEE. 53, 773.

Maldonado, T. A. (1995). *Handbook of Optics*, volume II, chapter 13. McGraw-Hill, New York.

Marti, O., Colchero, J., Bielefeldt, H., Hipp, M., and Linder, A. (1993). *Scanning Probe Microscopy - Applications In Biology and Physics.* Microscopy Microanalysis Microstructures. 4, 429.

Martin-Moreno, L., Garcia-Vidal, F. J., J, L. H., Pellerin, K. M., Thio, T., Pendry, J. B., and Ebbesen, T. W. (2001). *Theory of extraordinary optical transmission through subwavelength hole arrays.* Phys. Rev. Lett. 86, 1114.

Michaels, A. M., Jiang, J., and Brus, L. (2000). *Ag Nanocrystal Junction as Site for Surface-Enhanced Raman Scattering of Single Rhodamine 6G Molecules.* J. Phys. Chem. B. 104, 11965.

Mie, G. (1908). *Beiträge zur Optik trüber Medien, speziell kolloidaler Metallösungen.* Ann. Phys. 25, 377.

Mirkin, C. A., Letsinger, R. L., Mucic, R. C., and Storhoff, J. J. (1996). *A DNA-based method for rationally assembling nanoparticles into macroscopic materials.* Nature. 382, 607.

Moskovits, M. (1985). *Surface-enhanced spectroscopy.* Rev. Mod. Phys. 57, 783.

Mullett, W. M., Lai, E. P. C., and Yeung, J. M. (2000). *Surface Plasmon Resonance-Based Immunoassays.* Methods. 22, 77.

Mulvaney, P. (1996). *Surface-Plasmon Spectroscopy Of Nanosized Metal Particles.* Langmuir. 12, 788–800.

Nie, S. and Emory, S. R. (1997). *Probing single molecules and single nanoparticles by surface-enhanced Raman scattering.* Science. 275, 1102.

Nolting, W. (1993). *Grundkurs: Theoretische Physik*, volume 3 (Elektrodynamik). Verlag Zimmermann-Neufang, Ulmen, 3rd edition.

Otto, A. (1968). *Excitation of Nonradiative Surface Plasma Waves in Silver by the Method of Frustrated Total Reflection.* Zeitschrift für Physik. 216, 398.

Paesler, M. and Moyer, P. J. (1996). *Near-Field Optics: Theory, Instrumentation, and Applications.* John Wiley & Sons, Inc., New York.

Palik, E. (1985). *Handbook of Optical Constants of Solids.* Academic Press, New York.

Perner, M. (1999). *Optische Untersuchung der Elektronen- und Gitterdynamik in Edelmetall-Nanopartikeln.* Shaker, Aachen. ISBN 3-8265-6814-1 (also Ph.D. thesis, Universität München).

Persson, B. N. J. (1993). *Polarizability of small spherical metal particles: influence of the matrix environment.* Surf. Sci. 281, 153.

Puech, K., Henari, F., Blau, W., Duff, D., and Schmid, G. (1995). *Investigation of the ultrafast dephasing time of gold nanoparticles using incoherent light.* Chem. Phys. Lett. 247, 13.

Quinten, M. and Kreibig, U. (1996). *Optical constants of gold and silver clusters in the spectral range between 1.5 eV and 4.5 eV.* Zeitschrift für Physik B. 101, 211.

Quinten, M., Kreibig, U., Schonauer, D., and Genzel, L. (1985). *Optical-Absorption Spectra of Pairs of Small Metal Particles.* Surf. Sci. 156, 741.

Raether, H. (1988). *Surface Plasmons on Smooth and Rough Surfaces and on Gratings.* Springer, Berlin.

Rich, R. L. and Myszka, D. G. (2000). *Survey of the 1999 surface plasmon resonance biosensor literature.* Journal of molecular recognition. 13, 388.

Salomon, L., Grillot, F., and de Fornel, F. (2001). Optical transmission of a metal film with periodic subwavelength holes: a near-field view. In *Postdeadline Papers.* Quantum Electronics and Laser Science Conference (QELS), Baltimore. (QPD5).

Schröter, U. and Heitmann, D. (1998). *Surface-plasmon-enhanced transmission through metallic gratings.* Phys. Rev. B. 58, 15419.

Seider (1996). *Nah- und Fernfeldspektroskopie Metallischer Mikrostrukturen.* Shaker, Aachen. ISBN 3-8265-2368-7 (also Ph.D. thesis, Universität Hamburg).

Serra, L. and Rubio, A. (1997). *Core polarization in the optical response of metal clusters: generalized time-dependent density-functional theory.* Phys. Rev. Lett. 78, 1428.

Shahbazyan, T. V., Perakis, I. E., and Bigot, J. Y. (1998). *Size-dependent surface plasmon dynamics in metal nanoparticlcs.* Phys. Rev. Lett. 81, 3120.

Shalaev, V. (2000). *Nonlinear Optics of Random Media: Fractal Composites and Metal-Dielectric Films.* Springer, Berlin.

Shipway, A. N., Katz, E., and Willner, I. (2000). *Nanoparticle Arrays on Surfaces for Electronic, Optical, and Sensor Applications.* ChemPhysChem. 1, 18.

Silva, T. J. (1994). *A scanning near-field optical microscope with magneto- optical Kerr effect contrast for the imaging of magnetic domains with 200 Angstrom resolution.* Ph.D. thesis, Univ. of California, San Diego.

Smolyaninov, I., Mazzoni, D. L., and Davis, C. C. (1996). *Imaging of surface plasmon scattering by lithographically created individual surface defects.* Phys. Rev. Lett. 77, 3877.

Smolyaninov, I., Mazzoni, D. L., Mait, J., and Davis, C. C. (1997). *Experimental study of surface-plasmon scattering by individual surface defects.* Phys. Rev. B. 56, 1601.

Sommerfeld, A. (1909). *Über die Ausbreitung der Wellen in der drahtlosen Telegraphie.* Annalen der Physik (4th series). 28, 44.

Specht, M., Pedarnig, J., Heckl, W., and Hänsch, T. (1992). *Scanning Plasmon Near-Field Microscope.* Phys. Rev. Lett. 68, 476.

Stietz, F., Bosbach, J., Wenzel, T., Vartanyan, T., Goldmann, A., and Träger, F. (2000). *Decay Times of Surface Plasmon Excitation in Metal Nanoparticles by Persistent Spectral Hole Burning.* Phys. Rev. Lett. 84, 5644.

Tae Jin, K., Thio, T., Ebbesen, T. W., Grupp, D. E., and Lezec, H. J. (1999). *Control of optical transmission through metals perforated with subwavelength hole arrays.* Opt. Lett. 24, 256.

Takai, H. (1998). *Controlled Formation of Gold Microparticles on a Surface: Application as Localized Surface Plasmon Sensor.* Tech. Dig. 16th Sensor Symposium. C, 123.

Taton, T. A. (2000). *Scanometric DNA Array Detection with Nanoparticle Probes.* Science. 289, 1757.

Treacy, M. (1999). *Dynamical diffraction in metallic optical gratings.* Appl. Phys. Lett. 75, 606.

Underwood, S. and Mulvaney, P. (1994). *Effect of the Solution Refractive-Index on the Color of Gold Colloids.* Langmuir. 10, 3427.

van de Hulst, H. C. (1957). *Light scattering by small particles.* Dover, New York.

Vartanyan, T., Simon, M., and Trager, F. (1999). *Femtosecond optical second harmonic generation by metal clusters: the influence of inhomogeneous line broadening on the dephasing time of surface plasmon excitation.* Appl. Phys. B. 68, 425.

Weaver, J., Krafka, G., Lynch, D., and Koch, E. (1981). *Optical Properties of Metals, Physik Daten Nr. 18-2.* FIZ Karlsruhe. 1-2.

Winsemius, P. (1972). *Temperature dependence of the optical properties of Au and Ag.* Ph.D. thesis, University of Leiden.

Xia, Y., Gates, B., Yin, Y., and Lu, Y. (2000). *Monodispersed Colloidal Spheres: Old Materials with New Applications.* Adv. Mater. 12, 693.

Zenneck, J. (1907). *Über die Fortpflanzung ebener elektromagnetischer Wellen längs einer ebenen Leiterfläche und ihre Beziehung zur drahtlosen Telegraphie.* Annalen der Physik (4th series). 23, 846.

Curriculum Vitae

University education:

01/1998-	Ludwig-Maximilians-Universität (LMU) Munich, Germany Ph.D. candidate in physics in the Photonics and Optoelectronics group
9/1996- 10/1997	University of Cambridge, England M.Phil. in the Polymers and Colloids group (Prof. Donald), thesis entitled *‘Environmental Scanning Electron Microscopy (ESEM) on living cells’*
9/1994- 9/1996	University of Hamburg, Germany ’Vordiplom’ (intermediate diploma), Final score: ’excellent’
1993-1994	Audited physics (3 semesters) while attending high school

National service:

1993-1994	German mandatory national service (15 months) working for the environmental agency of Hamburg (in the water protection division).

Secondary school in Hamburg, Germany:

1993	Graduation with the final score 1.0 Major courses: Mathematics, Physics, and Chemistry
8/1990	Internship at the Fred Hutchinson Cancer Research Center, Seattle (USA)
1990	High-school in Seattle, USA (one semester), GPA: 3.7/4.0
1986-1992	Member of the mathematical talent promotion project of Hamburg
1990-1993	Trained as chemical laboratory assistant

Elected as class representative in Grades 5 to 10 and 12 to 13 in secondary school

Scholarships:

1993-1998	National Merit Foundation (’Studienstiftung des deutschen Volkes’)
1995-1996	Fritz-Prosiegel-Scholarship of the University of Hamburg
1996-1997	DAAD (German Academic Exchange Program) scholarship
1996-1997	King Edwards VIIth scholarship and European Trust grant

Awards and youth competitions:

’jugend forscht’ (young reasearcher) projects (with Eike Lau and Mathias Püstow)

1992	1st prize (physics) in Hamburg and 4th prize (physics) at the national level
1991	2nd prize (mathematics) in Hamburg
1990-1993	several 1st, 2nd and 3rd prizes in the first rounds of the national youth competitions in mathematics, computer science, and physics.
1990	Seattle, USA: Science Olympiad, State Finals (2nd prize)

ACKNOWLEDGEMENTS

Experimental research is almost impossible without the close interaction of many people. I am deeply indebted to all those involved in the research I present in this thesis — for their help, guidance, friendship, patience and their constructive criticism. I hope for understanding that it is impossible to mention everyone individually.

As head of the group, Prof. Dr. Jochen Feldmann has initiated this research and provided the necessary infrastructure, funding and scientific contacts. He has closely followed this work and influenced it with many ideas and recommendations. Discussions have often led to find new perspectives or deeper insight into observations. I benefited greatly from the opportunity he gave me to present my work at workshops and conferences and his strive for improvement of such presentations.

Dr. Gero von Plessen has supervised this project by critically following all stages of the experiments and making many suggestions. Discussions with him have been a crucial step for a deeper understanding of all aspects of this thesis. More over, he handled much of the administrative work associated with modern research. I also wish to express great thanks for critical proof-reading the manuscript of this thesis and the associated publications.

Dr. Nancy Hecker's extensive knowledge of experimental techniques has been of great help to me in many cases. Her continuous motivation and scientific interest throughout this thesis has been an important motivation to continue working during troublesome and frustrating times.

Most importantly, I wish to thank all graduate students who have worked closely with me and contributed to the findings presented here. It would have been a lot less fun without them.

Alexander Duch has spent many long nights with me squeezing light through nanoholes. Stefan Geier helped setting up the TIR setup with great enthusiasm. In one of the most important evenings of our struggle with the setup, Stephan Geier did *not* reject my admittedly crazy idea to put the whole, brand-new, 150 000 DM spectrometer on top of the quite shaky microscope. To our own surprise, it finally worked this way. Arpad Jakab has been a stimulating companion. I have learned a lot about alternative music styles during our joint experiments. Dorle Guentzer and Arne Morteani have been critical discussion partners on the properties of surface and particle plasmons, electrodynamics and life in general.

Tatjana Wilk, Thomas Franzl and Stephan Malkmus have started as summer students with great commitment on their 'sweet plasmon' project. The fun we had at many private events and their continuing interest in nanoparticle research have been a very stimulating motivation and made my stay in Munich much more enjoyable. Special thanks goes to

Thomas Franzl, who continued working voluntarily on nanorods and particle pairs, for his help with the last and very last measurements for this thesis.

All my colleagues in this group have spent a lot of time with me during the last three years. All of them deserve great thanks for continuous support and the friendly atmosphere in the Sommerfeld lab. Michael Breit, with whom I shared the office for most of the time, has always had an open ear for the current experimental problems. Dr. Uli Lemmer often had to help out with money for the equipment I ordered. Christoph Lingk, Jürgen Müller and Stefan Riechel have been motivating and helpful colleagues for some years now. Eric Dulkeith has solved the 'pidgin-problem'. Gunnar Raschke has silently solved many technical problems. Clemens Hoffmann and Prof. Jürgen Köhler have provided helpful input to the organization of the laboratory in general and provided many helpful little tricks for experiments or computer programs. The 'new' members of the Photonics and Optoelectronics Group, Hubertus von Poschinger, Thomas Niedereichholz, Jana Crewett, Dr. Milena DeGiorgi, Martin Reufer and Johann Schermer have been friendly companions during the stressful time of writing this thesis. Thanks also go to the former members of the group, in particular to Stefan Grosse and Thomas Klar, who built the near-field setup which formed the basis for the setup I used in the experiments on nanoholes. Many problems were solved quickly and competently by the technical staff of the group, Anna Helfrich, Werner Stadler, and Stefan Niedermayer.

Cooperations with other groups have been an essential part for my work. I am very thankful for the efficient, friendly and open cooperation of Prof. Dr. Joachim Spatz and Dr. Vanessa Chan at the University of Ulm, who spent a lot of time with me in the clean-room producing nanoparticle samples. Special thanks goes to Dr. Vanessa Chan for her critical proof-reading of many English manuscripts I wrote, including part of this thesis. I learnt a lot about electron beam lithography and particle plasmons during the three months I spent at the University of Graz in the group of Prof. Dr. Franz Aussenegg with Dr. Joachim Krenn, Gerburg Schider, Bernhard Lamprecht and Harry Brunner. Paul Mulvaney has been a stimulating discussion partner and provided beautiful nanorod samples. Prof. Vladimir Shalaev, who spent part of his sabbatical in Munich, has been a stimulating discussion partner on scientific and non-scientific topics. The members of the neighboring group of Prof. Dr. Hermann Gaub, in particular Martin Benoit and Thorsten Hugel, have been very cooperative and often helped out with advice and equipment.

Last but not least, I have to thank my family for their great support during the time of my university education and for their understanding for the little time I was able to spend with them during the past years.